WWU
MÜNSTER

New Finite Element Methods for Solving the MEG and the Combined MEG/EEG Forward Problem

Dissertation

Maria Carla Piastra
-2019-

wissen.leben
WWU Münster

ChilDBrain

IBB
Institute for
Biomagnetism and
Biosignalanalysis

Angewandte
Mathematik
Münster

New Finite Element Methods for Solving the MEG and the Combined MEG/EEG Forward Problem

Inaugural-Dissertation zur Erlangung des Doktorgrades
der Naturwissenschaften
- Dr.rer.nat. -
im Fachbereich Mathematik und Informatik
der Mathematisch-Naturwissenschaftlichen Fakultät
der Westfälischen Wilhelms-Universität Münster
als interdisziplinäre Promotion
in Zusammenarbeit mit der Medizinischen Fakultät

vorgelegt von
Maria Carla Piastra
aus Genova
-2019-

Dekan: Prof. Dr. Xiaoyi Jiang
Erstgutachter: Prof. Dr. Christian Engwer
Zweitgutachter: Prof. Dr. Carsten H. Wolters
Drittgutachter: Prof. Dr. Benedikt Wirth
Viertgutachterin: Dr. habil. Maureen Clerc
Tag der mündlichen Prüfung: 11.03.2019
Tag der Promotion: 11.03.2019

Abstract

This thesis covers two main topics: on the one hand, the goal is to study new finite element method (FEM) techniques to solve the magnetoencephalography (MEG) and the combined MEG/electroencephalography(EEG) forward problem. On the other hand, the objective is to apply FEM to analyze MEG and EEG sensitivity to cortical and subcortical sources. In the first part of the thesis, a continuous (CG-) and a discontinuous (DG-) Galerkin FEM for solving the MEG and the combined MEG/EEG forward problems are presented and validated in both spherical and realistically shaped head models. We show for both FEM approaches that the partial integration approach outperforms the subtraction approach with regard to modeling the primary sources. Furthermore, in sphere models, DG-FEM provided results that are in a comparable range of high accuracy as CG-FEM, whereas in realistically shaped head models, we reported slightly more accurate results when DG-FEM is utilized. In contrast to the EEG case, the skull leakage effects do not play a crucial role for MEG. However, for EEG or combined MEG/EEG source analysis scenarios, DG-FEM offers an interesting new alternative to CG-FEM, considering the importance of a high accuracy of the forward problem solution in MEG/EEG source reconstruction. In the second part of the thesis, an EEG and MEG sensitivity study is presented, by computing signal-to-noise ratio (SNR) mappings based on FEM. In this study we recommend to rely on sensitivity maps that were constructed with at least a four compartment (skin, skull, cerebrospinal fluid, brain) head model. We focus on the importance of the contribution of the additional CSF compartment when compared to a standard three compartment modeling approach, especially in the EEG case. We conclude that MEG SNR values are higher than EEG SNR values when considering cortical sources. Moreover, while EEG SNR values are insensitive to source orientation, MEG SNR values remarkably vary with the orientation. Finally, the simulation results show that deep tangential sources can be detected by both the EEG and MEG modalities. The implementation of the new FEM for solving the MEG and combined MEG/EEG are collected in the *duneuro* toolbox and described in the last part of the thesis. Finally, during the PhD training, which is part of the ChildBrain project, a Horizon2020 Marie Skłodowska-Curie Action Innovative Training Network – European Training Network, special emphasis has been given to dissemination. Educational courses at international conferences and schools have been indeed linked to the implemented FEMs for solving partial differential equations in neuroscience.

Acknowledgment

I would like to express my sincere gratitude to

Carsten H. Wolters, my *Doktorvater*, who motivated me to move to Germany, he welcomed me in his working group, he introduced me and guided me through brain research and he supervised this thesis

Christian Engwer, who supported, motivated and guided me at the Numerics Institute and he supervised this thesis

Andreas Nüßing and Johannes Vorwerk who always offered me their support, from the very beginning

Andreas Nüßing, Sophie Schrader and Johannes Vorwerk for proof-reading this thesis and much more

all my new and old colleagues from the SIM-NEURO group, the Applications of PDEs group, the IBB, with special emphasis to the IBB previous and present IBB directors Christo Pantev and Joachim Gross, and the Numerics Institute in Münster

Paavo Leppänen, the coordinator of the ChildBrain project, together with all the p.i.s who made this project possible

all my colleagues and friends from the ChildBrain project, for the great experience we lived together, from conferences to jumps into frozen lakes (Praghajieeth Raajhen S., Caroline Beelen, Raul Granados, Gloria Romagnoli, Cecilia Mazzetti, Diandra Brkic', Weiyong Xu, Sam Van Bijnen, Anna Samsel, Abinash Pant, Vân Phan, Simon Homölle, Marios Antonakakis, Amit Jaiswal)

Harald Bornfleth, Robert Oostenveld, Lauri Parkkonen and Sampsa Pursiainen for the fruitful scientific and non-scientific discussions

Maureen Clerc and Théo Papadopoulo for hosting me at INRIA and for their valuable scientific input

Benedikt Wirth and Maureen Clerc for accepting to be examiners of this work

my family, for their warm long-distance cheer

my parents and my brother, for their constant and incredible energy, understanding and care, without whom I would have not enjoyed and grasped so many opportunities, e non avrei acceso il cervello quanto dovuto!

Lamine, for his heart and his smile (:

Contents

Notations and Abbreviations

$\mathbf{E}$	electric field
$\mathbf{B}$	full magnetic field (B-field)
$\mathbf{B}^p$	primary B-field
$\mathbf{B}^s$	secondary B-field
$\mathbf{j}$	total current density
$\mathbf{j}^p$	primary current density
$\mathbf{j}^s$	secondary current density
σ	conductivity profile of the conductive medium
u	electric potential
Ω	open set (model domain)
$\mathbf{M}$	moment of the mathematical dipole
δ	Dirac delta distribution
Φ	magnetic flux
$\mathbf{A}$	magnetic vector potential
$L^2(\Omega)$	set of square-integrable functions over Ω
$H^k(\Omega)$	Sobolev space of $L^2(\Omega)$ functions with $L^2(\Omega)$ derivatives up to order $k \in \mathbb{N}$
$H^k_*(\Omega)$	Sobolev space of functions with zero mean
$\mathbb{P}^k_d$	space spanned by monomials with exponents of $\lvert \cdot \rvert_1$-norm at most k
$\mathbb{Q}^k_d$	space spanned by monomials with exponents of $\lvert \cdot \rvert_\infty$-norm at most k
$\mathcal{T}_h$	triangulation of the set Ω
Γ_{int}	internal skeleton
$[\![\cdot]\!]$	jump operator
$\{\cdot\}$	weighted average operator
η	penalty parameter
RT_0	space of the lowest-order Raviart Thomas function

boundary SA	boundary subtraction approach
CG	continuous Galerkin
CDG	continuous and discontinuous Galerkin
CRF%	cumulative relative frequency in percentage
CSF	cerebrospinal fluid
DG	discontinuous Galerkin
DTI	diffusion tensor imaging
EEG	electroencephalography
FEM	finite element method
IQR	interquartile range
MAG%	magnitude error in percentage
MEG	magnetoencephalography
MRI	magnetic resonance imaging
PDE	partial differential equation
PI	partial integration approach
RDM%	relative difference measure in percentage
SA	subtraction approach
SNR	signal-to-noise ratio
TR	total range
VEN	Venant's approach

List of Figures

List of Tables

Introduction

The importance of human brain research cannot be overstated. More than 1,000 disorders of the brain and nervous system result in more hospitalizations and lost productivity than any other disease group, including heart disease and cancer [1]. There are many fields involved in human brain research, such as medicine, psychology, pharmacology, biology, engineering, mathematics, physics, chemistry etc. and the synergy of different expertise and fields bring brain research forward. An important element helping brain research is represented by neuroimaging techniques. Nowadays there are several advanced brain imaging techniques used in research facilities and hospitals throughout the world. They can be classified into two main groups: structural imaging techniques, such as magnetic resonance imaging (MRI), computed tomography (CT), ultrasound, whose aim is to identify the structure and anatomy of the tissues under examination, and functional imaging techniques, such as functional MRI (fMRI), electroencephalography (EEG), magnetoencephalography (MEG), positron emission tomography (PET), single-photon emission computed tomography (SPECT), which are able to investigate the activity or metabolism of the scanned tissue. Within this context, EEG and MEG are devoted to detect the electric potential distribution and the magnetic field generated by the brain, respectively, with a unique time resolution (range of ms) [18].
An important topic in many applications of EEG and MEG is the source reconstruction, i.e., the identification of the sources in the brain responsible for the signals recorded at the head surface (EEG) or at a small distance from the head surface (MEG). In order to compute MEG/EEG source reconstructions, i.e., to solve a related ill-posed inverse problem of MEG/EEG, the forward problem has to be solved. Since the accuracy of MEG/EEG inverse problem solutions depends

---

[1] `https://neuronline.sfn.org/Home/SfN/About/About-Neuroscience`

strongly on the forward solution, it is fundamental to increase the accuracy of the latter [18]. In the EEG case, the forward problem consists in the evaluation of the electric potential generated by a source located in the brain by solving an elliptic partial differential equation of second order [96]. In the MEG case, the magnetic field needs to be computed exploiting Biot-Savart's law, which depends on the EEG solution [18].

In simplified scenarios, such as multi-layer sphere models with piecewise homogeneous conductivity, analytical solutions are available [18]. In more realistic scenarios, e.g., realistically shaped head models, numerical methods have to be adopted. There is a large variety of numerical methods that can be employed. Among them are boundary element methods [59, 1, 40, 80], finite volume methods [24], finite difference methods [92, 84, 58] and finite element methods (FEMs) [17, 54, 79, 30, 72, 65].

Even if generated by the same sources, EEG and MEG carry complementary information. For example, there are studies showing that some epileptic spikes could be recorded only in MEG and not in EEG and vice versa [2, 4, 93]. In these scenarios, it has been shown [9, 8, 34] that combined MEG/EEG employs the complementary information of both modalities providing source reconstructions that outperform the ones provided by each single modality. The complementarity of EEG and MEG can be further studied through sensitivity maps, which show the EEG and MEG sensitivity to different sources in the brain. Sensitivity maps widen insights about the modulation of source orientations and locations to EEG and MEG signals; therefore, they lead to a correct interpretation of source reconstruction results, especially when EEG and MEG modalities are combined. Moreover, they can help quantifying the detectability of epileptic spikes in clinical routine, they can guide the design of new sensors, they can help planning experiments and they can influence the choice of preprocessing procedures to apply to recorded EEG and MEG signals. It is crucial that such sensitivity maps are as accurate as possible and, in order to improve this accuracy, one can work on the representation of the geometry of the model, of the electrical features of the model and on the mathematical method which can include different features, e.g., FEMs, which have shown high numerical accuracies with the possibility to model complex geometries and bioelectromagnetic properties (e.g., anisotropic conductivity) of the head.

The EEG forward problem has been extensively studied and approached via

different FEMs, for example, with a standard lagrangian continuous Galerkin FEM (CG-FEM) [1], a discontinuous Galerkin FEM (DG-FEM) [31], a mixed-FEM [88], an unfitted discontinuous Galerkin FEM [65], a cutFEM [63]. In contrast, not many recent studies have been conducted to solve the MEG forward problem with FEMs [1] and, to the best of our knowledge, none of them are about DG-FEM. Accurate MEG forward problem solutions represent an important ingredient to combined EEG and MEG source reconstruction. Furthermore, in such a multi-modal MEG/EEG reconstruction it is desirable to use the same forward model for both EEG and MEG data.
In the first part of this thesis this lack is addressed and a tool which enables a shared unique framework for solving both EEG and MEG forward problems, via CG and DG-FEMs, is presented and validated, both in spherical and realistic individualized head models. In the second part of the thesis, accurate sensitivity maps are consequently generated via the resolution of the EEG and MEG forward problem with FEM, and analyzed.

This thesis is structured as follows. In Chapter 1, both the physiological and mathematical backgrounds are presented and the EEG and MEG forward problems are derived; Chapter 2 is dedicated to the CG-FEM applied to solve the MEG forward problem: the basic theory, several approaches to deal with a singular right-hand side and the validations results are presented. In Chapter 3, the DG-FEM theory to solve the MEG forward problem is shown, together with validation results. In Chapter 4, CG- and DG-FEM simulation results are compared both in spherical and realistic head models. Finally, the content of Chapter 5 is a sensitivity study, where accurate EEG and MEG sensitivity maps are generated with FEMS, and analyzed.

1. General Background

In this chapter we present both a physiological and a mathematical background for the MEG and EEG forward problems.

1.1. Physiological Background

Already in the XIX century the cells were assumed to be the fundamental unit of all living organs. The extremely complex organization of the nervous tissue, together with an inadequate technology, let the biologists of that period think that the nervous tissue rather had a net structure. The Italian biologist Camillo Golgi referred to that as *reticulum*. On the other side, by means of Golgi's staining method to visualize biological tissue [39], the Spanish neuroanatomist Santiago Ramón y Cajal and the British physiologist Charles Sherrington replaced Golgi's reticular theory with the so called *neuron doctrine*. They claimed that nerve cells are discrete entities which communicate with one another by means of specialized contacts, i.e., synapses. The neuron doctrine was confirmed only in the 1950s with the advent of electron microscopy. Nevertheless, both Golgi and Cajal were awarded with the Nobel prize in 1906 in Physiology and Medicine for their findings on the organization of the nervous system and in 1932 also Sherrington was recognized for his contribution. The intense debate between especially Golgi and Cajal can be seen as the starting point of modern neuroscience.

The histological studies of Cajal, Golgi, and a host of successors led to the consensus that the cells of the nervous system can be divided into two broad categories: nerve cells, or neurons, and glial cells. The human brain is estimated to contain about 86 billion neurons and at least that many glial cells [73]. While

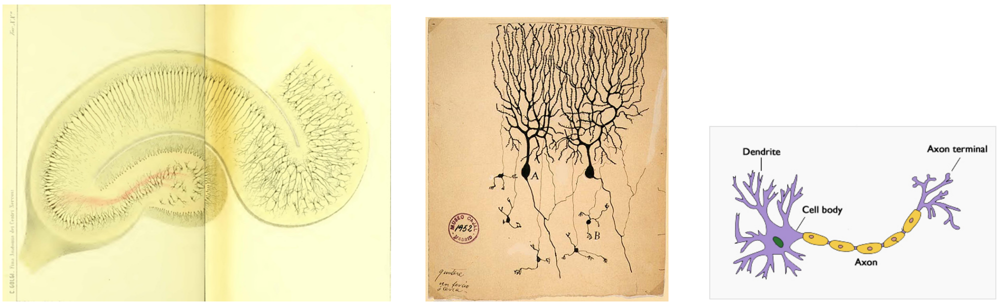

Figure 1.1.: Golgi's drawing of the hippocampus, based on tissues he had stained. From Golgi's 1886 publication "Sulla fina anatomia degli organi centrali del sistema nervoso." (on the left); 1899 drawing of Purkinje cells (A) and granule cells (B) from pigeon cerebellum by Santiago Ramón y Cajal. [image © Instituto Cajal, Madrid, Spain] (in the center); Schematic representation of the anatomy of the neuron (on the right).

nerve cells are devoted to electrical signaling over long distances, glial cells are supporting nerve cells and do not generate a signal themselves. Each neuron consists of a cell body, dendrites, and an axon (see Figure 1.1, on the right). The cell body contains the nucleus and cytoplasm. The axon extends from the cell body and often gives rise to many smaller branches before ending at nerve terminals. Dendrites extend from the neuron cell body and receive messages from other neurons. Synapses are the contact points where one neuron communicates with another. The dendrites are covered with synapses formed by the ends of axons from other neurons.

Neurons never function in isolation; they are organized into ensembles called neural circuits that process specific kinds of information and make up neural systems that serve broader purposes. The most general functional distinction divides such collections into sensory systems, motor systems and associational systems [73].

A more detailed picture of the events underlying any neural circuit can be obtained by electrophysiological recording, which measures the electrical activity of nerve cells [73]. With EEG the electric potential differences are measured by means of electrodes positioned on the scalp of the patient or healthy subject. This method was initially adopted in clinical practice to localize epileptic foci and epileptogenic cortical tissue for presurgical diagnosis. First attempts were made at the Montreal Neurological Institute by Herbert Jasper and Wilder Panfield.

Due to the non-invasive nature of this technique, EEG was thereafter used for basic research on healthy subjects. Similarly to EEG, the MEG measures brain activity by recording magnetic fields produced by electrical currents generated in the brain. Neuromagnetic signals are typically between 50 and 500 fT, therefore the MEG method is based on the superconducting quantum interference device or SQUID, a sensitive detector of magnetic flux, introduced in the late 1960s by James Zimmerman [99, 41]. The first SQUID measurement of magnetic fields of the brain was carried out at the Massachusetts Institute of Technology by David Cohen [23]. He measured the spontaneous α activity of a healthy subject and the abnormal brain activity of an epileptic patient [41]. MEG is closely related to EEG. In both methods, the measured signals are generated by the same synchronized neuronal activity in the brain. The time resolution of MEG and EEG is in the millisecond range, orders of magnitude better than in almost any other technique adopted in neuroscience [41]. Both EEG and MEG are completely non-invasive techniques.

In general, nerve cells generate a variety of electrical signals that transmit and store information [73]. Two main electrical signals are generated by neurons: action potentials and post-synaptic potentials. The action potential can be approximated with a current quadrupole, while a synaptic current flow with a dipole. The decay of an action potential is therefore faster ($1/r^3$, with r being the distance) than the one of a synaptic potential ($1/r^2$). Furthermore, temporal summation of currents flowing in neighboring fibers is more effective for synaptic currents, which last tens of milliseconds, than for action potentials, which have a duration of one millisecond only [41]. Thus EEG and MEG signals are produced in large part by synaptic current flow, which is approximately dipolar [41, 66, 60].

Finally, neuroscientists and neurologists have conventionally divided the vertebrate nervous system anatomically into central and peripheral components [73]. The central nervous system (CNS) comprises the brain (cerebral hemispheres, diencephalon, cerebellum, and brainstem) and the spinal cord. The peripheral nervous system (PNS) includes the sensory neurons that link sensory receptors on the body surface or deeper within it with relevant processing circuits in the CNS [73]. Two gross histological terms distinguish regions rich in neuronal cell bodies versus regions rich in axons. Gray matter refers to any accumulation of cell bodies in the brain and spinal cord. White matter (named for its relatively light appearance, the result of the lipid content of myelin) refers to axon tracts and commissures [73]. Within gray matter, nerve cells are arranged in two different ways. A local accumulation with neurons that have roughly similar connections and functions is called a *nucleus*; such collections are found throughout the cerebrum, diencephalon, brainstem, and spinal cord. In contrast, *cortex* describes sheetlike arrays of nerve cells. Within the white matter of the CNS, axons are gathered into tracts that are more or less analogous to nerves in the periphery [73].

1.2. Mathematical Background

In this section the mathematical models adopted to emulate the generation of electric potentials and magnetic fields, i.e., the EEG and MEG forward problems, are deduced.

1.2.1. Derivation of the EEG and MEG Forward Problem

Following [41] and [18], the electric potential distribution and the resulting magnetic induction generated in the brain can be modeled through the quasi-static approximation of Maxwell's equations, when assuming that the permeability of the tissue in the head is that of the free space, i.e., $\mu = \mu_0$,

$$\begin{aligned} \nabla \times \mathbf{E} &= 0, \qquad (1.1a) \\ \nabla \cdot \mathbf{E} &= \frac{\rho}{\epsilon_0}, \end{aligned}$$

related to the electrical part, and

$$\nabla \times \mathbf{B} = \mu_0 \, \mathbf{j}, \qquad (1.2a)$$

$$\nabla \cdot \mathbf{B} = 0, \qquad (1.2b)$$

related to the magnetic part, where $\mathbf{E}$ is the electric field, $\mathbf{B}$ the magnetic field, ρ is the electric charge density, ϵ_0 is the permittivity of free space and μ_0 is the permeability of free space. In (1.2a) $\mathbf{j}$ represents the total current density produced by neuronal activity, which, in bio-electromagnetism [41, 18], is split into two contributions,

$$\mathbf{j}(\mathbf{r}) = \mathbf{j}^p(\mathbf{r}) + \mathbf{j}^s(\mathbf{r}), \tag{1.3}$$

where $\mathbf{j}^p$ is the so called primary current, $\mathbf{j}^s$ the secondary or volume current and $\mathbf{r} \in \mathbb{R}^3$. In neuromagnetism, the primary current is widely represented as a *mathematical point dipole* [28, 60],

$$\mathbf{j}^p(\mathbf{r}) = \mathbf{M} \cdot \delta(\mathbf{r} - \mathbf{r}_0), \tag{1.4}$$

where $\mathbf{M} \in \mathbb{R}^3$ stands for the dipolar moment and δ is the Dirac delta distribution centered in the dipole position $\mathbf{r}_0 \in \mathbb{R}^3$.

The volume current is a passive current that is the result of the macroscopic electric field on charge carriers in the conducting medium [41, 18], and

$$\mathbf{j}^s = \sigma \mathbf{E} \tag{1.5}$$

holds true (Ohm's law), where σ indicates the conductivity profile of the conductive medium. While for the mathematical point dipole the primary current is present only at the source position, the secondary current flows passively everywhere in the medium.

The Forward Problem of EEG

To derive the EEG forward problem, (1.1a) and (1.2a) have to be considered. As a consequence of (1.1a), there exists a potential u such that

$$\mathbf{E} = -\nabla u, \tag{1.6}$$

so that (1.5) can be written as

$$\mathbf{j}^s = -\sigma \nabla u. \tag{1.7}$$

Applying the divergence to (1.2a), we obtain

$$\nabla \cdot \mathbf{j} = 0. \tag{1.8}$$

Combining (1.3), (1.7) and (1.8), we get an inhomogeneous Poisson equation that, together with the homogeneous Neumann boundary condition, models the EEG forward problem:

$$\nabla \cdot (\sigma \nabla u) = \nabla \cdot \mathbf{j}^p (= f), \qquad \text{in } \mathit{\Omega} \subseteq \mathbb{R}^3 \tag{1.9}$$

$$\sigma \nabla u \cdot \mathbf{n} = 0, \qquad \text{on } \partial \mathit{\Omega} \tag{1.10}$$

where $\mathit{\Omega}$ is the volume conductor and $\mathbf{n}$ is the unit outer normal vector on $\partial\Omega$. The EEG forward problem consists in finding the electric potential u on the domain Ω, assuming to know σ and $\mathbf{j}^p$. The strong formulation, as it appears in (1.9), admits a solution $u \in \mathcal{C}^2(\Omega)$ if restrictions are imposed on the source term f and the conductivity tensor σ. In this framework, the usual assumptions on this model are that, for example, the conductivity tensor is only piecewise constant, i.e., $\sigma \in L^\infty(\Omega)$ and that $\mathbf{j}^p$ is a distribution, see (1.4). The idea is then to relax the conditions required to the solution u by introducing the weak formulation of the problem, which reads: find $u \in V$ such that

$$\int_\Omega \sigma \nabla u \cdot \nabla v \, \mathrm{d}x = \int_\Omega f v \, \mathrm{d}x \,, \quad \forall v \in V.$$

The weak formulation can be deduced by multiplying the strong formulation for a so-called test function $v \in V$, integrating the resulting equation in the domain Ω and using Gauss' theorem (in a heuristic way) to manipulate the left-hand side. The weak formulation can also be written in terms of both a linear and a bilinear operator, i.e., find $u \in V$

$$a(u, v) = l(v), \quad \forall v \in V,$$

where

$$\begin{aligned} a(u, v) &= \int_\Omega \sigma \nabla u \cdot \nabla v \, \mathrm{d}x \,, \\ l(v) &= \int_\Omega f v \, \mathrm{d}x \,. \end{aligned}$$

While in the strong formulation, the solution should be looked for in $V = \mathcal{C}^2(\Omega)$, for the weak formulation, it suffices that u belongs to the Sobolev function space $H^1(\Omega)$, or, more precisely, in the quotient $H^1_*(\Omega)$, following the definitions

$$H^1(\Omega) := \left\{ f \in L^2(\Omega) : D^1 f \in L^2(\Omega) \right\},$$

and

$$H^1_*(\Omega) := \left\{ f \in H^1(\Omega) : \int_\Omega f \, \mathrm{d}x = 0 \right\}.$$

When choosing $V = H^1_*(\Omega)$, it is possible to proof consistency with the strong formulation together with existence and uniqueness of the solution. More details can be found , e.g., in [86].

The Forward Problem of MEG

Solving the MEG forward problem means computing the magnetic induction, or magnetic flux, $\mathit{\Phi}$, generated by a dipolar source in the brain. The magnetic flux is computed from the magnetic field $\mathbf{B}$ (B-field):

$$\mathit{\Phi} = \int_S \mathbf{B} \cdot d\mathbf{s},$$

where S is the surface of the sensor.

The B-field can also be deduced by Maxwell's equations. In particular, from (1.2b) we have that it exists $\mathbf{A}$ such that $\mathbf{B} = \nabla \times \mathbf{A}$. $\mathbf{A}$ is the magnetic vector potential and it satisfy the Coulomb gauge, i.e., $\nabla \cdot \mathbf{A} = 0$. By manipulating (1.2a), we obtain the following chain of equalities:

$$\begin{aligned} \mu_0 \mathbf{j} &= \nabla \times \mathbf{B} \\ &= \nabla \times (\nabla \times \mathbf{A}) = \nabla(\nabla \cdot \mathbf{A}) - \nabla^2 \mathbf{A} \\ &= -\nabla^2 \mathbf{A}, \end{aligned} \tag{1.11}$$

and the solution of the Poisson equation in (1.11) is

$$\mathbf{A}(\mathbf{r}) = \frac{\mu_0}{4\pi} \int_\Omega \frac{\mathbf{j}(\mathbf{r}')}{|\mathbf{r} - \mathbf{r}'|} \, d^3\mathbf{r}'.$$

Therefore, the B-field can be written as follows:

$$\begin{aligned}\mathbf{B}(\mathbf{r}) &= \nabla \times \left(\frac{\mu_0}{4\pi} \int_\Omega \frac{\mathbf{j}(\mathbf{r}')}{|\mathbf{r}-\mathbf{r}'|} \right) d^3\mathbf{r}' \\ &= \frac{\mu_0}{4\pi} \int_\Omega \nabla \times \left(\frac{\mathbf{j}(\mathbf{r}')}{|\mathbf{r}-\mathbf{r}'|} \right) d^3\mathbf{r}'\end{aligned}$$

If we observe that

$$\begin{aligned}\nabla_\mathbf{r} \times \left(\frac{\mathbf{j}(\mathbf{r}')}{|\mathbf{r}-\mathbf{r}'|} \right) &= \nabla_\mathbf{r} \left(\frac{1}{|\mathbf{r}-\mathbf{r}'|} \right) \times \mathbf{j}(\mathbf{r}') + \frac{1}{|\mathbf{r}-\mathbf{r}'|} \nabla_\mathbf{r} \times \mathbf{j}(\mathbf{r}') \\ &= -\frac{\mathbf{r}-\mathbf{r}'}{|\mathbf{r}-\mathbf{r}'|^3} \times \mathbf{j}(\mathbf{r}') + 0 \\ &= \mathbf{j}(\mathbf{r}') \times \frac{\mathbf{r}-\mathbf{r}'}{|\mathbf{r}-\mathbf{r}'|^3},\end{aligned}$$

where $\nabla_\mathbf{r}$ indicates that ∇ acts on functions depending on the variable $\mathbf{r}$. Then we obtain Biot-Savart's law, giving the B-field at a point $\mathbf{r} \in \mathbb{R}^3$ outside the domain Ω,

$$\mathbf{B}(\mathbf{r}) = \frac{\mu_0}{4\pi} \int_\Omega \mathbf{j}(\mathbf{r}') \times \frac{\mathbf{r}-\mathbf{r}'}{|\mathbf{r}-\mathbf{r}'|^3} d^3\mathbf{r}', \tag{1.12}$$

Furthermore, when combining (1.3), (1.12) and (1.4), one obtains [41, 18]:

$$\begin{aligned}\mathbf{B}(\mathbf{r}) &\overset{(1.3,1.12)}{=} \frac{\mu_0}{4\pi} \int_\Omega (\mathbf{j}^p(\mathbf{r}') + \mathbf{j}^s(\mathbf{r}')) \times \frac{\mathbf{r}-\mathbf{r}'}{|\mathbf{r}-\mathbf{r}'|^3} d^3\mathbf{r}' \\ &\overset{(1.4)}{=} \frac{\mu_0}{4\pi} \mathbf{M} \times \frac{\mathbf{r}-\mathbf{r}_0}{|\mathbf{r}-\mathbf{r}_0|^3} - \frac{\mu_0}{4\pi} \int_\Omega \sigma \nabla u(\mathbf{r}') \times \frac{\mathbf{r}-\mathbf{r}'}{|\mathbf{r}-\mathbf{r}'|^3} d^3\mathbf{r}'\end{aligned}$$

Namely, the B-field can be split into two contributions as well, the primary B-field $\mathbf{B}^p$, which is calculated analytically for a mathematical point dipole:

$$\mathbf{B}^p(\mathbf{r}) = \frac{\mu_0}{4\pi} \mathbf{M} \times \frac{\mathbf{r}-\mathbf{r}_0}{|\mathbf{r}-\mathbf{r}_0|^3},$$

and the secondary B-field $\mathbf{B}^s$, which has to be computed numerically when the electrical potential is computed numerically (since it depends on the electrical potential u inside the domain Ω),

$$\mathbf{B}^s(\mathbf{r}) = -\frac{\mu_0}{4\pi} \int_\Omega \sigma \nabla u(\mathbf{r}') \times \frac{\mathbf{r}-\mathbf{r}'}{|\mathbf{r}-\mathbf{r}'|^3} d^3\mathbf{r}'. \tag{1.13}$$

1.2.2. A Conservation Property

A fundamental physical property of the EEG forward problem is the conservation of charge:

$$\int_{\partial K} \mathbf{j}^s \cdot \mathbf{n} \, \mathrm{d}s = \int_K f \, dK, \ \forall K \subset \Omega,$$

where $f = -\nabla \cdot \mathbf{j}^p$ and K is a control volume in Ω. We will refer to this conservation law by indicating the couple $(\sigma\nabla u, f)$, i.e., the boundary term and the volume term, respectively. For FEMs this property carries over to the discrete solution only if the test space contains the characteristic function, which is one in K and zero everywhere else. In general, a conforming discretization does not guarantee this property, while the discontinuous Galerkin finite element method fulfills a discrete analogue. More details will follow.

1.2.3. The MEG Analytical Solution

In simplified geometries, similarly to the EEG forward problem [18], there exist analytical solutions for the MEG forward problem [78, 48].
[78] showed that the magnetic field outside a spherically symmetric conductor due to internal current sources does not depend on the profile of conductivity along the radius. He derived the following analytical MEG solution for a multi-layer homogeneous sphere model:

$$\mathbf{B}(\mathbf{r}) = \frac{\mu_0}{4\pi F^2}(F\mathbf{M} \times \mathbf{r}_0 - \mathbf{M} \times \mathbf{r}_0 \cdot \mathbf{r}\nabla F), \tag{1.14}$$

where $\mathbf{a} = \mathbf{r} - \mathbf{r}_0$, $a = |\mathbf{a}|$, $r = |\mathbf{r}|$, $F = a(ra + r^2 - \mathbf{r} \cdot \mathbf{r}_0)$ and $\nabla F = (r^{-1}a^2 + a^{-1}\mathbf{a} \cdot \mathbf{r} + 2a + 2r)\mathbf{r} - (a + 2r + a^{-1}\mathbf{a} \cdot \mathbf{r})\mathbf{r}_0$.
[48] could even demonstrate that radial anisotropy added to a spherically symmetric conductor does not affect the external magnetic field due to internal sources. From (1.14), three important features of the analytical MEG solution for a multi-layer homogeneous sphere model and a point outside the model can be deduced:

Remark 1. *Three main properties of analytical MEG solution for a multi-layer homogeneous sphere model and a measurement point outside the model [78]:*

1. *the solution does not depend on the conductivity profile of the spherical model*
2. *if the source is radial, then the B-field outside* Ω *vanishes*
3. *the normal projection of the secondary component of the B-field gives a null contribution to the total B-field, i.e.* $\boldsymbol{B}^s(\boldsymbol{r}) \cdot \boldsymbol{n} = 0$, *for* $\boldsymbol{r}$ *outside* Ω.

2. The Continuous Galerkin Finite Element Method for Solving the MEG Forward Problem

There are cases when the strong formulation is not adequate to model the physical phenomenon under examination. Therefore, strong assumption on the solution can be relaxed and the weak formulation is deduced.

Galerkin methods are approaches which can be adopted in order to discretize weak formulations, dealing therefore with discrete problems defined on finite-dimensional subspaces V_h of the test function space V already mentioned in Chapter 1.

The finite element method in its simpler form is an example of a Galerkin method, as we will see in this chapter. The continuous Galerkin finite element method (CG-FEM) is also known as standard or lagrangian FEM, as the function space V_h contains *lagrangian* ansatz functions, i.e., *hat functions*. This function space constitutes a subset of $H^1(\Omega)$, therefore the method is said to be a *conforming* FEM. In the discretization step the weak formulation becomes a linear system, the function space containing the solution and the test functions is finite-dimensional, and the problem is solved in a discretized domain as it is described in the following. The theory section mainly follows [21] and [74].

In this chapter we deduce, illustrate and validate the CG-FEM to solve the MEG forward problem. To do so, we start (in Section 2.1) with the introduction of the basics of CG-FEM; in Section 2.2, the CG-FEM discretization scheme for the EEG forward solution is recalled throughout several representations of the right-hand side, namely, the *partial integration* approach (in Section 2.4), the *subtraction* approach (in Section 2.3), and *Venant's* approach (in Section 2.5). In Section 2.6, the discretization of the MEG forward problem is deduced and a speed-up procedure is mentioned. Finally, in Sections 2.7 and 2.8, validation results in sphere models are presented and discussed, respectively.

2.1. Basics of the CG-FEM

If we consider the abstract variational problem (cfr. Chapter 1): find $u \in V$ such that

$$a(u, v) = l(v), \forall v \in V, \tag{2.1}$$

posed over an open set Ω with a Lipschitz-continuous boundary, then the *Galerkin method* for approximating the solution of such problem consists in defining similar problems in finite-dimensional subspaces of the space V. More specifically, with a general finite-dimensional subspace V_h of V, we associate to (2.1) the discrete problem: find $u_h \in V_h$ such that

$$a(u_h, v_h) = l(v_h), \forall v_h \in V_h,$$

where u_h is the so-called discrete solution.

In order to apply the Galerkin method we therefore face, by definition, the problem of constructing finite-dimensional subspaces V_h of V. The finite element method, in its simplest form, is a specific process of constructing subspaces V_h, which shall be called finite element spaces. This construction is characterized by three basic aspects:

1. a triangulation $\mathcal{T}_h$ is established over the set $\bar{\Omega}$, i.e., the set $\bar{\Omega}$ is subdivided into a finite number of subsets E, called finite elements, in such a way that the following properties are satisfied:

    - $\bar{\Omega} = \bigcup_{E \in \mathcal{T}_h} E$

    - for each $E \in \mathcal{T}_h$, the set E is closed and the interior $\mathring{E}$ is non-empty

- for each distinct $E_e, E_f \in \mathcal{T}_h$, one has $E_e \bigcap E_f = \emptyset$
- for each $E \in \mathcal{T}_h$, the boundary ∂E is Lipschitz-continuous

2. the functions $v_h \in V_h$ are piecewise polynomials
3. there should exist a basis in the space V_h whose functions have *small* supports.

The CG-FEM is characterized by the following choice of V_h:

$$V_h = X_h^r = \{v_h \in \mathcal{C}^0(\Omega) : v_h|_E \in P_r, \forall E \in \mathcal{T}_h\}, \tag{2.2}$$

i.e., the space of functions which are globally continuous and piecewise polynomials. As in this case the space V_h is a subset of V, the CG-FEM is defined as a *conforming* FEM. We now introduce two particular polynomial spaces:

Definition 2.1.1. *(Polynomial space $\mathbb{P}_d^k$) Let $k \geq 0$ be an integer, $A_d^k := \{\alpha \in \mathbb{N}^d : |\alpha|_{l^1} \leq k\}$ and $|\cdot|_{l^1}$ the 1-norm. Then the polynomial space $\mathbb{P}_d^k$ of polynomials of d variables, of total degree at most k, is defined as*

$$\mathbb{P}_d^k := \left\{ p : \mathbb{R}^d \ni z \mapsto p(x) \in \mathbb{R} : \exists (\gamma_\alpha)_{\alpha \in A_d^k} \in \mathbb{R}^{card(A_d^k)} \ s.t. \ p(x) = \sum_{\alpha \in A_d^k} \gamma_\alpha x^\alpha \right\}.$$

The dimension of $\mathbb{P}_d^k$ is equal to $card(A_d^k) = \binom{k+d}{k}$.

Definition 2.1.2. *(Polynomial space $\mathbb{Q}_d^k$) Let $k \geq 0$ be an integer, $B_d^k := \{\alpha \in \mathbb{N}^d : |\alpha|_{l^\infty} \leq k\}$ and $|\cdot|_{l^\infty}$ the ∞-norm. Then the polynomial space $\mathbb{Q}_d^k$ of polynomials of degree at most k in each variable is defined as*

$$\mathbb{Q}_d^k := \left\{ p : \mathbb{R}^d \ni z \mapsto p(x) \in \mathbb{R} : \exists (\gamma_\alpha)_{\alpha \in B_d^k} \in \mathbb{R}^{card(B_d^k)} \ s.t. \ p(x) = \sum_{\alpha \in B_d^k} \gamma_\alpha x^\alpha \right\}.$$

The dimension of $\mathbb{Q}_d^k$ is equal to $card(B_d^k) = (k+1)^d$.

In the following, the space $P_r = \mathbb{P}_1^d$ is chosen when the triangulation is made of triangles ($d = 2$) or tetrahedra ($d = 3$) and $P_r = \mathbb{Q}_1^d$ when the triangulation is made of quadrilaterals ($d = 2$) or hexahedra ($d = 3$). In both cases, every function $v_h \in V_h$ is uniquely defined by the values that it assumes at the nodes $\mathbf{N}_i$, with $i = 1, ..., N_h$ of the triangulation $\mathcal{T}_h$. Therefore, a basis of V_h can be the set of functions $\varphi_j \in V_h$, $j = 1, ..., N_h$, such that

$$\varphi_j(\mathbf{N}_i) = \delta_{i,j} = \begin{cases} 0 & i \neq j \\ 1 & i = j \end{cases} \quad i, j = 1, ..., N_h.$$

In particular, if $r = 1$, the nodes are the vertices of the elements and the generic function φ_j is linear on each element, it is equal to 1 on node $\mathbf{N}_j$ and to 0 on every other node.

A generic function $v_h \in V_h$ can be expressed in terms of a linear combination of basis functions of V_h as follows

$$v_h(\mathbf{x}) = \sum_{i=1}^{N_h} v_i \varphi_i(\mathbf{x}), \ \ \forall \mathbf{x} \in \Omega, \tag{2.3}$$

where $v_i = v_h(\mathbf{N}_i)$.

In the following section, the CG-FEM discrete scheme for the EEG forward problem is recalled starting from the discretization just introduced. In general, the main focus of this chapter is on the MEG forward problem, so here only a summary is presented. For further details see, e.g., [86].

2.2. Solving the EEG Forward Problem

The conforming weak formulation of the EEG forward problem (1.9)-(1.10) introduced in Chapter 1 reads: find $u_h \in V_h \subset H^1(\Omega)$ such that

$$\int_\Omega \sigma \nabla u_h \cdot \nabla v_h dx = \int_\Omega f v_h dx \tag{2.4}$$

holds true, $\forall v_h \in V_h$. Choosing V_h as the space of piecewise linear, continuous functions, i.e., $V_h = X_h^r$, results in the classical CG-FEM. If we express the discrete solution u_h of (2.4) in terms of the basis $\{\varphi_j\}_j$ by using (2.3), we obtain

$$u_h(\mathbf{x}) = \sum_{j=1}^{N_h} u_j \varphi_j(\mathbf{x}), \;\; \forall \mathbf{x} \in \Omega, \tag{2.5}$$

where $u_j = u_h(\mathbf{N}_j)$. If we assume that (2.5) satisfies (2.4) for each element of the basis, then we obtain the following linear system with N_h equations in the N_h unknowns u_j which is equivalent to the problem (2.4),

$$\sum_{j=1}^{N_h} u_j \int_\Omega \sigma \nabla \varphi_j \cdot \nabla \varphi_i dx = \int_\Omega f \varphi_i dx, \tag{2.6}$$

for $i = 1, ..., N_h$. (2.6) can also be rewritten in terms of a discretized version of the bilinear and linear form a and l, i.e., a_h and l_h, respectively, as follows

$$a_h(\varphi_i, \varphi_j) = l_h(\varphi_i).$$

The so-called *stiffness matrix* of dimensions $N_h \times N_h$ is defined as

$$A = (a_{i,j})_{i,j=1,...,N_h}, \tag{2.7}$$

where

$$\begin{aligned} a_{i,j} = a_h(\varphi_i, \varphi_j) &= \int_\Omega \sigma \nabla \varphi_j \cdot \nabla \varphi_i dx, \\ l_i = l_h(\varphi_i) &= \int_\Omega f \varphi_i dx. \end{aligned}$$

If we furthermore introduce the vectors:

$$\mathbf{u} = (u_j)_j, \;\; \mathbf{l} = (l_i)_i,$$

the linear system in (2.6) can be written as follows

$$A\mathbf{u} = \mathbf{l}. \tag{2.8}$$

As the support of the generic basis function φ_i is made of only the elements of the triangulation which share the node $\mathbf{N}_i$, the matrix A is sparse. In our work, the linear system (2.8) is solved by means of a preconditioned conjugate gradient (CG) solver, more specifically with the algebraic multi-grid (AMG) preconditioning.

The AMG-CG solver was already implemented in the Distributed and Unified Numerics Environment (DUNE) [1] [14, 13, 12].

Remark 2. *When defining the vector* $\boldsymbol{l}$*, we did not consider the fact that often a dipolar expression of the source is taken into account. Therefore the integral in* l_i *is in general not well-defined when* $f = \nabla \cdot \boldsymbol{j}^p = \nabla \cdot \boldsymbol{M}\delta_{\boldsymbol{r}_0}$*.*

In the following sections three strategies adopted to deal with the singularity in l_i are described.

2.3. The Subtraction Approach

As already mentioned, the mathematical point dipole model introduces a singularity on the right-hand side of the PDE in (1.9) that can be treated, for example, with the so-called subtraction approach [79, 96, 30, 17, 7, 54].
The subtraction approach assumes that a non-empty neighborhood Ω^∞ around the source in $\mathbf{r}_0$ can be found with homogeneous conductivity σ^∞. The conductivity tensor σ is then split into two parts,

$$\sigma = \sigma^\infty + \sigma^{corr}, \tag{2.9}$$

where σ^{corr} vanishes in Ω^∞. The potential u can also be split into two contributions,

$$u = u^\infty + u^{corr}. \tag{2.10}$$

The so-called *singularity potential* u^∞ is the solution of the Poisson equation in an unbounded and homogeneous conductor with constant conductivity σ^∞, and it can be computed analytically, see e.g. [30]. The *correction potential* u^{corr} becomes the unknown of a new Poisson equation:

$$-\nabla \cdot (\sigma \nabla u^{corr}) = \nabla \cdot (\sigma^{corr} \nabla u^\infty), \qquad \text{in } \Omega \subseteq \mathbb{R}^3 \tag{2.11}$$

$$\sigma \nabla u^{corr} \cdot \mathbf{n} = -\sigma \nabla u^\infty \cdot \mathbf{n}, \qquad \text{on } \partial\Omega \tag{2.12}$$

---

[1] http://www.dune-project.org

after embedding (2.9) and (2.10) in (1.9) and (1.10). The conforming weak formulation of (2.11)-(2.12) presented in [96] reads: find $u_h^{corr} \in V_h \subset H^1(\Omega)$ such that

$$\int_\Omega \sigma \nabla u_h^{corr} \cdot \nabla v_h dx = -\int_\Omega \sigma^{corr} \nabla u_h^\infty \cdot \nabla v_h dx - \int_{\partial\Omega} \sigma^\infty \nabla u^\infty \cdot \mathbf{n}\, v_h ds \tag{2.13}$$

holds true, $\forall v_h \in V_h$. When choosing V_h as the space of piecewise linear, continuous functions the classical CG-FEM is obtained.

The subtraction approach is theoretically well understood. A deep numerical analysis of the subtraction approach including proofs for uniqueness and existence has been carried out in [96] and [30].

The matrix form of (2.13) is: find $u_h^{corr} \in V_h$ such that

$$A\mathbf{u}^{corr} = \mathbf{l}^{corr}, \tag{2.14}$$

where A is the stiffness matrix defined in (2.7), $\mathbf{u}^{corr} = (u_j^{corr})_j$, and $\mathbf{l}^{corr} = (l_i^{corr})_i = -\int_\Omega \sigma^{corr} \nabla u^\infty \cdot \nabla \varphi_i dx - \int_{\partial\Omega} \sigma^\infty \nabla u^\infty \cdot \mathbf{n} \varphi_i ds$. Once the linear system (2.14) is solved, the full potential $u_h = u_h^{corr} + u^\infty$ can be assembled.

Remark 3. *When the subtraction approach is adopted for discretizing the EEG forward problem, two main points have to be considered:*

1. *the numerical accuracy of the method for sources that are very close to a conductivity jump, e.g., the brain-CSF boundary, can decrease remarkably (see [96] and [30]);*

2. *the discrete right-hand side of the linear system is a dense vector, therefore the computation can be time-consuming.*

2.4. The Partial Integration Approach

Another way to deal with the singular right-hand side of the EEG forward problem equation is to use the definition of a differential operator D acting on the Dirac delta distribution centered in $\mathbf{r}_0 \in \mathbb{R}^3$, i.e.,

$$\langle D(\delta_{\mathbf{r}_0}), \phi\rangle = -D(\phi)(\mathbf{r}_0), \tag{2.15}$$

where ϕ is a smooth function with compact support. If we use this definition on the right-hand side of (2.4) with $D = \nabla$, we obtain

$$\begin{aligned} l(v_h) &= \int_\Omega f v_h dx \\ &= \int_\Omega \nabla \cdot (\mathbf{M}\delta_{\mathbf{r}_0}) v_h dx \\ &= -\mathbf{M}\nabla v_h(\mathbf{r}_0), \end{aligned}$$

where we considered the fact that $\mathbf{M}$ is constant and the behavior of the delta distribution and the integral operator.

The name of this approach comes from the fact that definition (2.15) mimics Gauss' theorem, or *partial integration*, for multi-dimensional functions. The discrete right-hand side of the linear system in (2.6) therefore is

$$\mathbf{l} = (l_i)_i = (-\mathbf{M}\nabla\varphi_i(\mathbf{r}_0))_i.$$

The vector $\mathbf{l}$ has non-zero entries only in the support of the basis function φ_i which contains the dipole itself. Furthermore we notice that in case of $V_h = \mathbb{P}_1$, l_i is constant on each element of the triangulation $\mathcal{T}_h(\Omega)$.

2.5. Venant's Approach

A third strategy to deal with the singular right-hand side of (2.4) makes use of the principle of Saint-Venant, and we refer to it as Venant's approach. Barré de Saint-Venant formulated his famous principle in 1855, but it was more of an observation than a strict mathematical statement: "If the forces acting on a small portion of the surface of an elastic body are replaced by another statically equivalent system of forces acting on the same portion of the surface, this redistribution of loading produces substantial changes in the stresses locally, but has a negligible effect on the stresses at distances which are large in comparison with the linear dimensions of the surface on which the forces are changed"[11]. Many scientists gave a more rigorous formulation of the principle, mainly in applications of elasticity. In structural engineering this principle is extensively used and the main message is that the exact distribution of a load is not important far away from the loaded region, as long as the resultants of the load are correct. This principle can be applied also in electrostatics, where instead of loads we deal with charges, and the resultants of the loads are the moments of the electric source distribution. Therefore, a point dipole can be replaced by a distribution of electrical monopoles, as long as the moments are equivalent. Crucial issues to address are related to the choice of the position and the intensity of the charges. [20], together with [96, 86, 55], dealt with these issues and here the main steps are reported.

The choice of the charge positions relies on the fact that we are considering lagrangian finite elements and the associated lagrangian ansatz functions, whose degrees of freedom are the values of the basis functions at the nodes of the triangulation. Hence, the monopoles are placed on the nodes of the element which contains the dipolar source. With regard to the choice of charge intensities, a linear system is built, where the actual moments of the dipolar source are equalized to the ones of a discrete distribution of electrical monopoles. More details are in the following.

The moments of a dipolar source are defined as

$$^{k}T = Q\left(\frac{d}{2}\right)^{k} - Q\left(\frac{-d}{2}\right)^{k} = Q\frac{d^{k}}{2}(1-(-1)^{k}),$$

where Q is the charge strength, d is the distance between the two monopoles constituting the dipole, i.e., a source and a sink of equal strength Q. If the dipole is placed at the i-th node, we can write its target dipole moment as $^{k}T_{i}^{j}$, with $j = 1, 2, 3$. On the other side, the moments of a source distribution at an observation point $\mathbf{r}$ are defined as

$$^{k}M(\mathbf{r}) = \int_{\Omega} (\mathbf{r}' - \mathbf{r})^{k} \rho(\mathbf{r}') d^{3}\mathbf{r}',$$

where ρ is the continuous distribution of charge. When a point-like monopolar distribution of charge is considered, i.e., when

$$\rho(\mathbf{r}) = \sum_{l=1}^{N} q_l \delta(\mathbf{r} - \mathbf{r}_l),$$

where q_l are the monopolar source strengths and $\mathbf{r}_l$ are the locations of the monopoles, we get the moments

$$^{k}M(\mathbf{r}) = \sum_{i=l}^{N} (\mathbf{d}_l)^k q_l, \tag{2.16}$$

where $\mathbf{d}_l = \mathbf{r} - \mathbf{r}_l$. If we refer to monopolar load moment for the k-th monopole close to the i-th monopole, we write $^{k}M_i^j$, and the distances become $(\mathbf{d}_{il})_j^k$, with $j = 1, 2, 3$. The vector equation (2.16) can be written as a linear system, which we express for every component $j = 1, 2, 3$ of the vectors in (2.16):

$$\begin{bmatrix} (^{0}M_i)_j \\ (^{1}M_i)_j \\ \vdots \\ (^{k}M_i)_j \end{bmatrix} = \begin{bmatrix} (\mathbf{d}_{i,1})_j^0 & (\mathbf{d}_{i,2})_j^0 & \cdots & (\mathbf{d}_{i,N})_j^0 \\ (\mathbf{d}_{i1})_j^1 & (\mathbf{d}_{i2})_j^1 & \cdots & (\mathbf{d}_{iN})_j^1 \\ \vdots & \vdots & \ddots & \vdots \\ (\mathbf{d}_{i1})_j^k & (\mathbf{d}_{i2})_j^k & \cdots & (\mathbf{d}_{iN})_j^k \end{bmatrix} \cdot \begin{bmatrix} q_1 \\ q_2 \\ \vdots \\ q_N \end{bmatrix}.$$

In the next step, a quadratic positive functional $D > 0$ is introduced and minimized, in the spirit of a least squares expression and inverse regularization techniques.

$$D = \frac{1}{2}\left(^{k}T_i^j - (d_{il}^j)^k q_l\right)\left(^{k}T_i^j - (d_{is}^j)^k q_s\right) + \lambda_D \frac{1}{2} q_l g_{ls} q_s,$$

where

$$g_{ls} = \begin{cases} (d_{il} d_{is}) & l = s \\ 0 & l \leq s. \end{cases}$$

When differentiating with regard to q_t we obtain

$$\left((d_{it}^j)^k (d_{is}^j)^k + \lambda_D g_{ts}\right) q_s = (d_{it}^j)^{k k}T_i^j,$$

which can be rewritten as

$$a_{ts} \cdot \mathbf{q}_s = \mathbf{b}_t. \tag{2.17}$$

The system (2.17) is symmetric and positive definite and the order is given by the number of monopoles, which are chosen, for example, as the nodes belonging to the same element as the dipolar source, therefore the system can be solved fast. For further details about this approach and for the discussion about the choice of the parameters involved, we refer to [20]. Finally, the right-hand side of (2.4) looks like

$$\mathbf{l} = (l_i)_i = (\mathbf{q}_i)_i,$$

which is different from zero only in the neighboring nodes of the source location.

2.6. Solving the MEG Forward Problem

Once the EEG forward problem is solved, the secondary component of the B-field, $\mathbf{B}^s$, can be numerically computed. In this section, we focus on the expression of the secondary B-field, as the primary B-field, $\mathbf{B}^p$, is analytically computable (cfr. Chapter 1).

In the CG-FEM framework, the EEG forward solution u_h is projected to the discrete space V_h already introduced, leading to equation (2.5), i.e., $u_h(\mathbf{r}) = \sum_{j=1}^{N_h} u_j \varphi_j(\mathbf{r})$, $\forall \mathbf{r} \in \Omega$. Furthermore, in a CG-FEM approach the following expression of the electric flux ($\mathbf{j}_h^{CG}$) is considered:

$$\begin{aligned} \mathbf{j}_h^{CG} &= \sigma \nabla u_h \\ &= \sigma \sum_j u_j \nabla \varphi_j. \end{aligned} \tag{2.18}$$

where $(\varphi_j)_j$ is a collection of hat functions, basis of V_h. The discretization $\mathbf{B}_h^s$ of $\mathbf{B}^s$ is then given by

$$\mathbf{B}_h^s(\mathbf{r}) = -\frac{\mu_0}{4\pi} \sum_j u_j \int_\Omega \sigma \nabla \varphi_j(\mathbf{r}') \times \frac{\mathbf{r} - \mathbf{r}'}{|\mathbf{r} - \mathbf{r}'|^3} \, d^3\mathbf{r}'.$$

Note that $(u_j)_j$ are given from the EEG forward computation. If we call $\mathbf{c}_n$ the center of the n^{th} coil, then the discrete $\mathbf{B}_h^s$ evaluated in $\mathbf{c}_n$ is

$$\mathbf{B}_h^s(\mathbf{c}_n) = \sum_j u_j \underbrace{\left(-\frac{\mu_0}{4\pi}\right) \int_\Omega \sigma \nabla \varphi_j(\mathbf{r}') \times \frac{\mathbf{c}_n - \mathbf{r}'}{|\mathbf{c}_n - \mathbf{r}'|^3} \, d^3\mathbf{r}'}_{:= S_{nj}^{CG}}, \tag{2.19}$$

where $S^{CG} = \left(S_{nj}^{CG}\right)_{n,j}$ is the secondary magnetic field integration matrix. Finally, equation (2.19) can be rewritten as a matrix equation,

$$\mathbf{B}_h^s = S^{CG}\mathbf{u}. \tag{2.20}$$

An alternative treatment of $\mathbf{B}^s$ involves the already mentioned *conservation of charge property*, whose fulfillment is not guaranteed for the flux in (2.18). Such alternative is presented in the next chapter.
As described in the following, MEG forward computations are carried out for a large number of dipole sources. In order to speed up the many numerically expensive computations of the secondary B-field $\mathbf{B}^s$ for all of these sources, following [35, 95], we adapted and implemented the transfer matrix approach for the presented CG-FEM-based MEG forward modeling scheme. Details can be found in Appendix A.4.

Subtraction Approach In the particular case of the subtraction approach, the same procedure is applied to both the infinity and the correction contributions to the secondary B-field. More specifically, since we are dealing with numerical integration, both u^∞ and u^{corr} are projected to the discrete space V_h, i.e.,

$$u_h^\infty(\mathbf{r}) = \sum_i u_i^\infty \varphi_i(\mathbf{r}),$$

and

$$u_h^{corr}(\mathbf{r}) = \sum_i u_i^{corr} \varphi_i(\mathbf{r}),$$

where $(\varphi_i)_i$ represent a basis of the discrete space V_h, while u_h^∞ and u_h^{corr} are the discrete representations of u^∞ and u^{corr}, respectively. Note that u^∞ has an analytical expression. The discretizations $\mathbf{B}_{\infty,h}^s$ and $\mathbf{B}_{corr,h}^s$ of $\mathbf{B}_\infty^s$ and $\mathbf{B}_{corr}^s$, respectively, are then:

$$\mathbf{B}^s_{\infty,h}(\mathbf{r}) = -\frac{\mu_0}{4\pi}\sum_i u_i^{\infty}\int_{\Omega}\sigma\nabla\varphi_i(\mathbf{r}')\times\frac{\mathbf{r}-\mathbf{r}'}{|\mathbf{r}-\mathbf{r}'|^3}\,d^3\mathbf{r}',$$

and

$$\mathbf{B}^s_{corr,h}(\mathbf{r}) = -\frac{\mu_0}{4\pi}\sum_i u_i^{corr}\int_{\Omega}\sigma\nabla\varphi_i(\mathbf{r}')\times\frac{\mathbf{r}-\mathbf{r}'}{|\mathbf{r}-\mathbf{r}'|^3}\,d^3\mathbf{r}',$$

respectively. Note that $(u_i^{corr})_i$ are given from the EEG forward computation. Then the discrete $\mathbf{B}^s_{\infty,h}$ and $\mathbf{B}^s_{corr,h}$ evaluated in the center $\mathbf{c}_n$ of the n^{th} coil are

$$\mathbf{B}^s_{\infty,h}(\mathbf{c}_n) = \sum_i u_i^{\infty}\left(-\frac{\mu_0}{4\pi}\right)\int_{\Omega}\sigma\nabla\varphi_i(\mathbf{r}')\times\frac{\mathbf{c}_n-\mathbf{r}'}{|\mathbf{c}_n-\mathbf{r}'|^3}\,d^3\mathbf{r}', \tag{2.21}$$

and

$$\mathbf{B}^s_{corr,h}(\mathbf{c}_n) = \sum_i u_i^{corr}\left(-\frac{\mu_0}{4\pi}\right)\int_{\Omega}\sigma\nabla\varphi_i(\mathbf{r}')\times\frac{\mathbf{c}_n-\mathbf{r}'}{|\mathbf{c}_n-\mathbf{r}'|^3}\,d^3\mathbf{r}', \tag{2.22}$$

respectively.
Equations (2.21) and (2.22) can be rewritten as matrix equations,

$$\mathbf{B}^s_{\infty,h} = S^{CG}\mathbf{u}^{\infty},$$

and

$$\mathbf{B}^s_{corr,h} = S^{CG}\mathbf{u}^{corr},$$

respectively. Note that in equation (2.22), the following expression of the flux $(\mathbf{j}_h^{corr,CG})$ is considered:

$$\begin{aligned}\mathbf{j}_h^{corr,CG} &= \sigma\nabla u_h^{corr}\\ &= \sigma\sum_k u_k^{corr}\nabla\varphi_k.\end{aligned}$$

An alternative treatment of B^s_{∞} is by exploiting the fact that ∇u^{∞} has an analytical expression and that $\sigma|_{\Omega^{\infty}} = \sigma_{\infty}$ constant and isotropic [30]. We then can write

$$\begin{aligned}\mathbf{B} =&\frac{\mu_0}{4\pi}\left(\mathbf{M}\times\frac{\mathbf{d}}{|\mathbf{d}|^3}\right)\\ &-\frac{\mu_0}{4\pi}\int_{\Omega}\sigma\nabla u^{corr}\times\frac{\mathbf{d}}{|\mathbf{d}|^3}\,\mathrm{d}x\\ &-\frac{\mu_0}{4\pi}\int_{\Omega\backslash\Omega_\infty}\sigma\nabla u^{\infty}\times\frac{\mathbf{d}}{|\mathbf{d}|^3}\,\mathrm{d}x\\ &-\frac{\mu_0}{4\pi}\int_{\Omega_\infty}\sigma\nabla u^{\infty}\times\frac{\mathbf{d}}{|\mathbf{d}|^3}\,\mathrm{d}x\,,\end{aligned}\tag{2.23}$$

where we indicated with $\mathbf{d}$ the relative distance to an observation point $\mathbf{r}$ outside the computational domain Ω, i.e., $\frac{\mathbf{r}-\mathbf{r}'}{|\mathbf{r}-\mathbf{r}'|^3}$. Since ∇u^∞ is singular in the dipole position, the numerical treatment of (2.23) is not trivial. One way to deal with this issue is to reformulate (2.23) as a surface integral, as stated in the following Proposition:

Proposition 1. *It holds that*

$$\frac{\mu_0}{4\pi}\int_{\Omega_\infty}\sigma\nabla u^{\infty}\times\frac{\boldsymbol{d}}{|\boldsymbol{d}|^3}\,\mathrm{d}x = \frac{\mu_0\sigma^\infty}{4\pi}\int_{\partial\Omega_\infty}u^\infty\left(\boldsymbol{n}\times\frac{\boldsymbol{d}}{|\boldsymbol{d}|^3}\right)\mathrm{d}s\,,\tag{2.24}$$

where $\sigma|_{\Omega^\infty}=\sigma_\infty$ *is considered constant and isotropic.*

The following Lemma and Remark lead to the proof of Proposition 1.

Lemma 1. *The vector field* $\frac{\boldsymbol{d}}{|\boldsymbol{d}|^3}$ *in* (2.23), *with* $\frac{\boldsymbol{r}-\boldsymbol{r}'}{|\boldsymbol{r}-\boldsymbol{r}'|^3}$, *is conservative.*

Proof. If we consider $f(\mathbf{r})=|\mathbf{d}(\mathbf{r})|$, we have that $\nabla f=\frac{\mathbf{d}}{|\mathbf{d}|^3}$, which proves that $\frac{\mathbf{d}}{|\mathbf{d}|^3}$ is conservative. □

Remark 4. *If* φ *is a scalar function and* $\boldsymbol{F}$ *is a field vector, then*

$$\nabla\times(\varphi\boldsymbol{F})=\nabla\varphi\times\boldsymbol{F}+\varphi\nabla\times\boldsymbol{F}$$

holds true.

The proof of Proposition 1 therefore is:

Proof. [of Proposition 1] As a first step, we can exploit the fact that $\sigma|_{\Omega^\infty} = \sigma_\infty$ is constant and isotropic:

$$\frac{\mu_0}{4\pi}\int_{\Omega_\infty} \sigma \nabla u^\infty \times \frac{\mathbf{d}}{|\mathbf{d}|^3}\,\mathrm{d}x = \frac{\mu_0 \sigma^\infty}{4\pi}\int_{\Omega_\infty} \nabla u^\infty \times \frac{\mathbf{d}}{|\mathbf{d}|^3}\,\mathrm{d}x\,.$$

Then the identity in Remark 4 can be integrated over the volume Ω_∞ and can be considered with $\varphi = u^\infty$ and $\mathbf{F} = \frac{\mathbf{d}}{|\mathbf{d}|^3}$, resulting in:

$$\begin{aligned}\frac{\mu_0 \sigma^\infty}{4\pi}\int_{\Omega_\infty} \nabla u^\infty \times \frac{\mathbf{d}}{|\mathbf{d}|^3}\,\mathrm{d}x =& \frac{\mu_0 \sigma^\infty}{4\pi}\int_{\Omega_\infty} \nabla \times \left(u^\infty \frac{\mathbf{d}}{|\mathbf{d}|^3}\right)\mathrm{d}x \\ &- \frac{\mu_0 \sigma^\infty}{4\pi}\int_{\Omega_\infty} u^\infty \nabla \times \frac{\mathbf{d}}{|\mathbf{d}|^3}\,\mathrm{d}x\,.\end{aligned} \tag{2.25}$$

Proposition 1 is proven when applying Gauss' theorem to (2.25) and having that a conservative field vector is curl-free, i.e., $\nabla \times \frac{\mathbf{d}}{|\mathbf{d}|^3} = 0$. ☐

Therefore we can write

$$\begin{aligned}\mathbf{B} =& \frac{\mu_0}{4\pi}\left(\mathbf{M} \times \frac{\mathbf{d}}{|\mathbf{d}|^3}\right) \\ &- \frac{\mu_0}{4\pi}\int_{\Omega} \sigma \nabla u^{corr} \times \frac{\mathbf{d}}{|\mathbf{d}|^3}\,\mathrm{d}x \\ &- \frac{\mu_0}{4\pi}\int_{\Omega\setminus\Omega_\infty} \sigma \nabla u^\infty \times \frac{\mathbf{d}}{|\mathbf{d}|^3}\,\mathrm{d}x \\ &- \frac{\mu_0 \sigma^\infty}{4\pi}\int_{\partial\Omega_\infty} u^\infty \left(\mathbf{n} \times \frac{\mathbf{d}}{|\mathbf{d}|^3}\right)\mathrm{d}s\,.\end{aligned} \tag{2.26}$$

From the implementation point of view, the analytical expression of ∇u^∞ is evaluated at the quadrature points and the subdomain Ω_∞ is represented by a patch of elements in $\mathcal{T}_h(\Omega)$. A similar concept was used in [36] and applied to magnetocardiogram forward simulations.

2.7. Validation in Sphere Models

In this section, we validate, compare and evaluate the convergence of the CG-FEM developed and implemented for solving the MEG forward problem when different discretizations of the right-hand side are adopted, namely the *subtraction* approach, the *partial integration* approach and *Venant's* approach, in the spherical volume conductor models described in Appendix A.1. The volume conductor models used in the validation studies are 4-layer homogeneous sphere models represented via hexahedral meshes with three different resolutions, namely 4 mm, 2 mm and 1 mm. Details on the models and meshes are in Tables A.1 and A.2, respectively. We considered 10,000 tangentially oriented dipoles, distributed in 10 logarithmically scaled eccentricities (see Table A.3), and we evaluated the secondary and the full B-field in 256 point-magnetometers outside the sphere model at a fixed radius of 110 mm (see Figure A.1). The errors were assessed via the $RDM\%$ and $MAG\%$, defined in (A.1) and (A.2), respectively. More details about the input data and error measures can be found in Appendix A.

We implemented the CG-FEM for the MEG forward problem in *duneuro* [64]. More details are in Appendix A.5.

Statistical results of numerical accuracies are visualized with mean curves, boxplots and cumulative relative frequencies curves. As a general remark, we consider only tangentially-oriented sources for the validations and evaluations in the next sections, because, as seen in Section 2.7, radial sources do not produce any magnetic field outside spherical volume conductor models.

Following formulas (1.13) and (1.12), we measure errors of the vector fields $\mathbf{B}^s$ and $\mathbf{B}$. These errors thus include parts from the radial and the two tangential sensor orientations and thus enable an overall view on the MEG forward modeling accuracy. On the one hand, radially-oriented sensor orientations are dominant in realistic MEG sensor configurations (see Figure 3.15), while on the other hand, and as seen in Section 1.2.3, because of the cancellation effect of primary and secondary B-fields, tangentially-oriented sensor orientations are especially delicate numerical test-cases.

Study 0: Preparatory Work using an Analytical Approach

To recall the most important symmetry properties of the MEG forward problem in spherical volume conductor models, to prepare the numerical studies below and to enable an easier interpretation of their results, we first tested and visualized the properties of the MEG analytical solution for a multi-layer homogeneous sphere model, as reported in Remark 1. Here, we consider radial and tangential point-magnetometers, i.e., we have projected the B-field ($\mathbf{B}^p$, $\mathbf{B}^s$, $\mathbf{B}$) onto the radial $\mathbf{n}$ and tangential $\mathbf{t}$ directions at sensor locations (Figure A.1).

In Figure 2.1a, we compared, for the tangentially-oriented sources at logarithmically scaled eccentricities and the 256 radial point-magnetometers, the L^2-norm of primary $\mathbf{B}^p$ (in pink) and secondary $\mathbf{B}^s$ (in blue) B-fields, i.e.,

$$||\mathbf{B}^p \cdot \mathbf{n}||_2, ||\mathbf{B}^s \cdot \mathbf{n}||_2. \tag{2.27}$$

We notice that the only contribution to radial point-magnetometers is given by the primary component of the B-field, $\mathbf{B}^s$, as proven in [78].

In Figure 2.1b, we plotted the L^2-norm of the full B-field for radial point-magnetometers normalized to the maximum over all tested sources, which is achieved for the most eccentric source, i.e.,

$$\frac{||\mathbf{B} \cdot \mathbf{n}||_2}{\max ||\mathbf{B} \cdot \mathbf{n}||_2}. \tag{2.28}$$

We can see how the magnitude of the full B-field increases for sources with an increasing eccentricity. In Figure 2.2, we investigated the analytical solutions in the spherical volume conductor model for tangential point-magnetometers (Figure A.1, middle). Figure 2.2 shows the L^2-norm of the primary (in pink) and secondary (in blue) tangential B-field components, i.e.,

$$||\mathbf{B}^p \cdot \mathbf{t}||_2, ||\mathbf{B}^s \cdot \mathbf{t}||_2, \tag{2.29}$$

for tangentially-oriented sources at different eccentricities. In this Figure we can see that, for tangential point-magnetometers, the deeper the sources are, the more the primary and secondary B-fields give identical contributions, but with opposite signs, to the full B-field, i.e., they more and more cancel each other out.

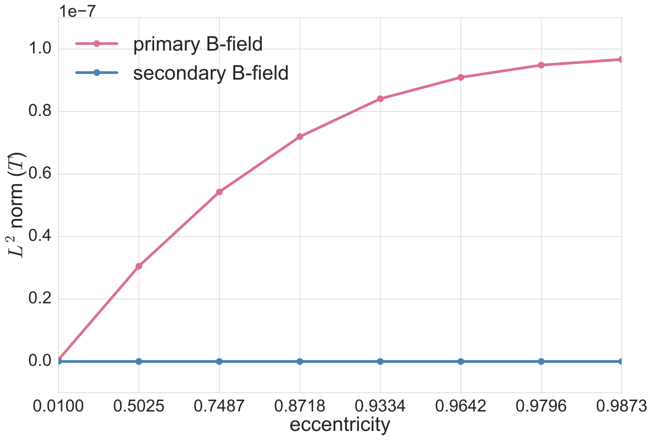

Figure 2.1a.: Analytical solutions in spherical volume conductor model for radial point-magnetometers: L^2-norm of the primary ($\mathbf{B}^p$, pink) and secondary ($\mathbf{B}^s$, blue) B-fields (see equations in (2.27)) for tangentially-oriented sources at logarithmically scaled eccentricities. Values are expressed in Tesla (T).

Towards the sphere center, sources become more and more radial and the full B-field goes down to zero. However, as Figure 2.2 also shows, with increasing source eccentricity the relative contribution of the primary tangential B-field component increases when compared to the secondary B-field component. The tangential full B-field projection (i.e., $\mathbf{B} \cdot \mathbf{t}$) and, together with it, the difference between primary and secondary tangential B-field components (i.e., $\mathbf{B}^p \cdot \mathbf{t}$ and $\mathbf{B}^s \cdot \mathbf{t}$) thus increase with increasing source eccentricity.

Study 1: CG-FEM and the Subtraction Approach

In this Section, we validated the MEG forward problem solution when the CG-FEM was adopted and the right-hand side of the Poisson equation (1.9) was discretized using the subtraction approach described in Section 2.3. For the validation we compared results for 4 mm, 2 mm and 1 mm resolution meshes described in Table A.2.

To observe the convergence of the method, we focus on the results given for the secondary B-field, which is computed numerically, when the mesh resolution is increased, namely from the coarsest resolution of 4 mm over 2 mm to the highest resolution of 1 mm. We studied the behavior of the RDM% and MAG% errors

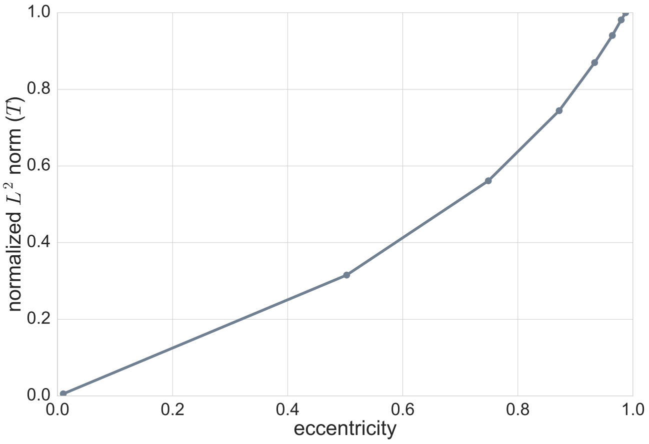

Figure 2.1b.: Analytical solutions in spherical volume conductor model for radial point-magnetometers: L^2-norm of the radial full B-field component relative to the one for the most eccentric source (see equation (2.28)) for tangentially-oriented sources at logarithmically scaled eccentricities. Values are expressed in Tesla (T)

for 10,000 tangentially oriented and randomly distributed dipoles at different eccentricities. Results can be seen in Figure 2.3.

The RDM% and MAG% error mean curves (Figure 2.3, left column) are overall increasing with increasing source eccentricity, as hypothesized by the theory of the subtraction approach [96] and well-known already from EEG results [30]. Most importantly, for increasing mesh resolution, error statistics improve considerably. For the most relevant eccentricity of 0.9796, the highest resolved model ($seg\_1\_res\_1$) reaches mean RDM% and MAG% errors of 0.88% and -0.01%, respectively. On the right column, we can study the boxplots of the RDM% and MAG% of the same scenario analyzed before. Both in the RDM% and MAG% cases, there is an overall increase of the median, total range (TR) and interquartile range (IQR) when increasing the source eccentricity and decreasing the mesh resolution.

If we focus on the 1 mm mesh and 0.9796 eccentricity, the RDM% median is only around 0.76%; the IQR is $\approx$ 0.75% and the TR reaches $\approx$ 3%. In particular, the IQR for dipoles of eccentricity 0.9796 increases drastically from $\approx$ 0.75% (1 mm) to almost 10% (2 mm) and 20% (4 mm). The TR behaves similarly. The median MAG% is extremely low, i.e., $\approx$ 0.015%; the IQR is $\approx$ 0.8% and the TR is $\approx$ 7.5%.

For this eccentricity, we notice a huge difference among the three mesh resolutions:

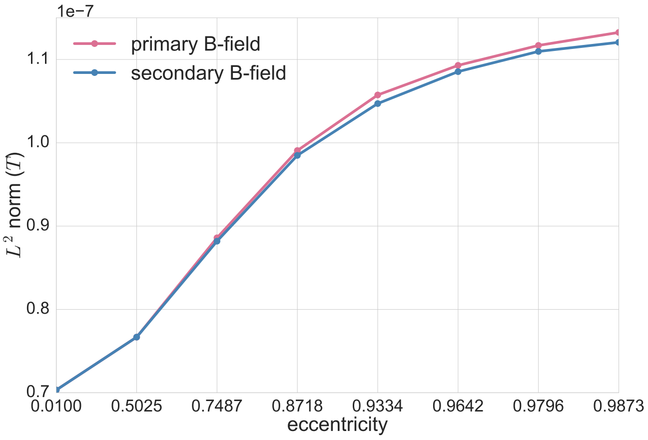

Figure 2.2.: Analytical solutions in spherical volume conductor model for tangential point-magnetometers: L^2-norm of the primary ($\mathbf{B}^p$, pink) and secondary ($\mathbf{B}^s$, blue) B-fields (see equations in (2.29)) for tangentially-oriented sources at logarithmically scaled eccentricities. Values are expressed in Tesla (T).

the medians grow from $\approx 0.015\%$ (1 mm), to $\approx 2.12\%$ (2 mm), up to $\approx 22.17\%$ (4 mm). The same trend is noticeable for the IQR: $\approx 0.8\%$ (1 mm), $\approx 8\%$ (2 mm) and $\approx 50\%$ (4 mm).

In general, we observe an increase of RDM% and MAG% values when the dipoles reach the last layer of hexahedra within the brain compartment, i.e., when the eccentricities are higher than the green, red and blue dashed lines for the 4 mm, 2 mm and 1 mm scenarios, respectively.

In Figure 2.4, we can analyze how the secondary B-field errors propagate to the full B-field solutions. As a general remark, we notice that dipoles with a very low eccentricity, i.e., 0.01, are in fact radially oriented dipoles, as they are very close to the center of the sphere. For those dipoles, there is a cancellation between primary and secondary B-field, resulting in a null full B-field. Therefore, when computing the MAG% error for those dipoles, the denominator is zero in (A.2), leading to an explosion in MAG% values, which is clearly visible in Figure 2.4. With regard to the main behavior of the errors, we observe same trends as in the secondary B-field study in Figure 2.3. In particular, for the most relevant eccentricity, i.e., 0.9796, and 1 mm resolution, the mean RDM% and MAG% reach $\approx 1.01\%$ and $\approx$ -0.01%, respectively, and the median RDM% and MAG% are $\approx 0.9\%$ and $\approx$ -0.0025%, respectively.

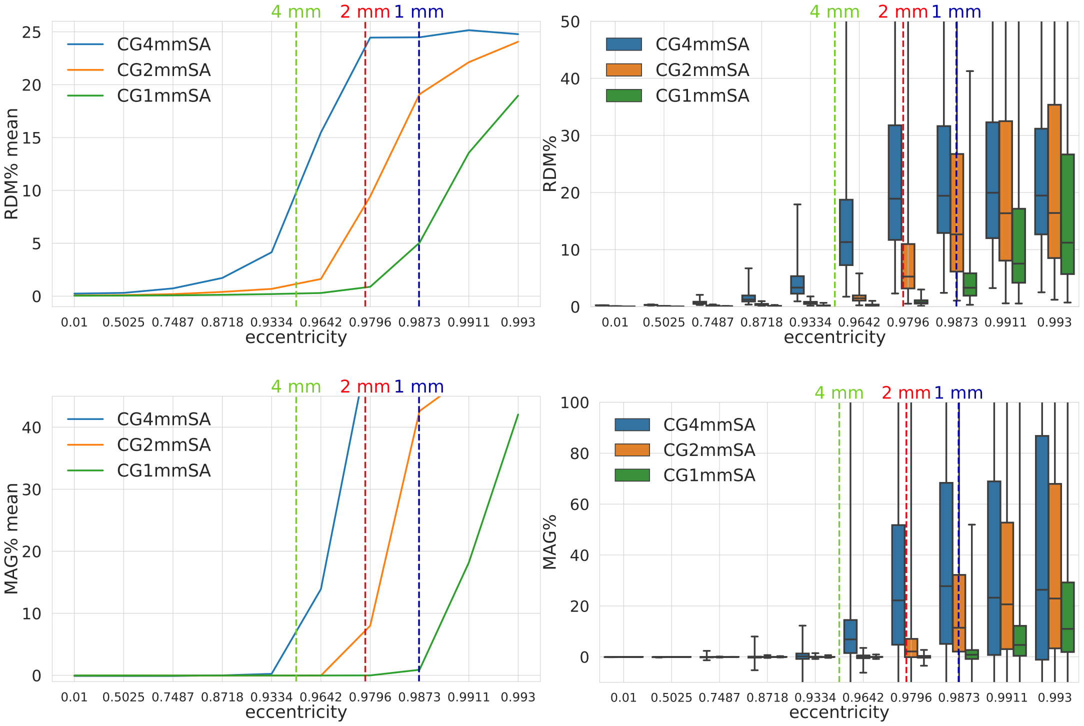

Figure 2.3.: Validation and convergence analysis for secondary B-field $\mathbf{B}^s$ computation (1.13) of CG-FEM when the *subtraction approach* is used in a 4 mm (blue), 2 mm (yellow) and 1 mm (green) hexahedral sphere model: visualized are the means (left column) and the boxplots (right column) of the RDM% (top row) and MAG% (bottom row), for tangentially oriented sources at logarithmically-scaled eccentricities. Dashed lines represent the eccentricities of 4 mm (green), 2 mm (red) and 1 mm (blue) distances to the brain-CSF boundary. Note the different scaling of the y-axes.

Study 2: CG-FEM and the Partial Integration Approach

In this section, a similar comparison as in the previous section is conducted. The secondary and full B-fields are compared to the analytical solution when the resolution of the mesh of the computational domain is increased, from 1 mm to 2 mm and 4 mm.

In this particular section, results for the partial integration approach introduced in Section 2.4 are analyzed via the RDM% and MAG% errors, for both the secondary and the full B-field visualized in Figure 2.5 and 2.6, for 10,000 tangentially oriented and randomly distributed dipoles at 10 different eccentricities already

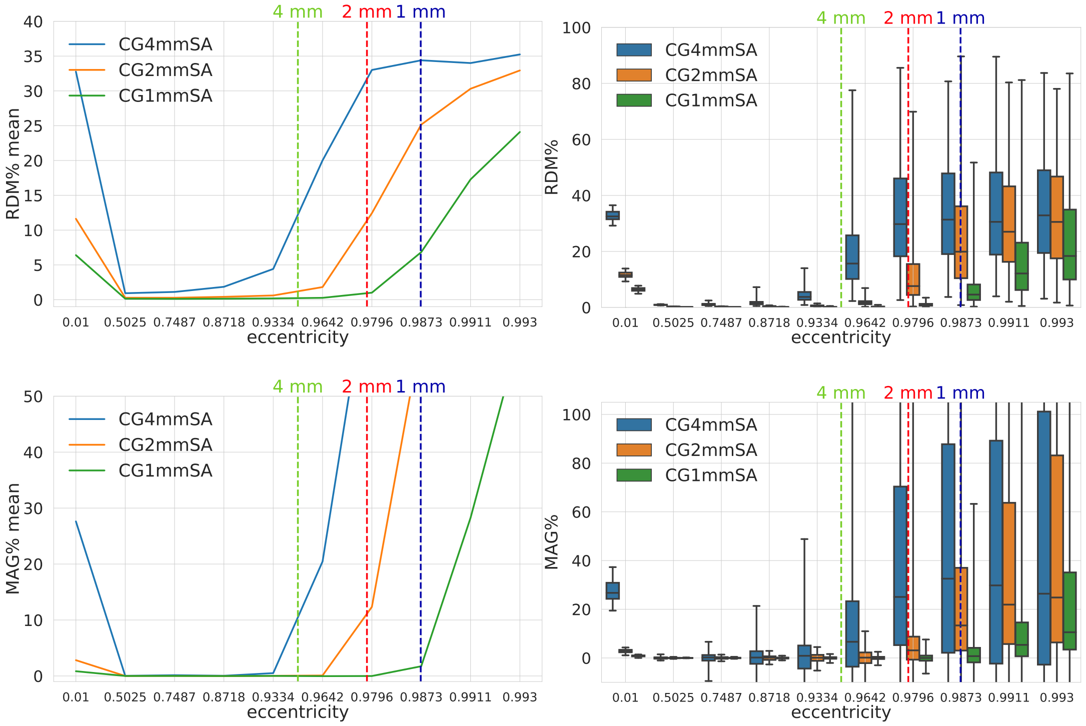

Figure 2.4.: Validation and convergence analysis for solving the MEG forward problem, i.e., the full B-field **B** (1.12), of CG-FEM when the *subtraction approach* is used in a 4 mm (blue), 2 mm (yellow) and 1 mm (green) hexahedral sphere model: visualized are the means (left column) and the boxplots (right column) of the RDM% (top row) and MAG% (bottom row), for tangentially oriented sources at logarithmically-scaled eccentricities. Dashed lines represent the eccentricities of 4 mm (green), 2 mm (red) and 1 mm (blue) distances to the brain-CSF boundary. Note the different scaling of the y-axes.

described.

Also in this scenario, we notice a general increase of errors when decreasing the mesh resolution, from 1 mm to 4 mm, and when increasing the source eccentricities. In particular, for the most relevant eccentricity of 0.9796, the highest resolved model (*seg_1_res_1*) reaches mean RDM% and MAG% errors of ≈ 0.87% and ≈ -0.03%, respectively. On the right column, we can study the boxplots of the RDM% and MAG% of the same scenario analyzed in Study 2.7. Both in the RDM% and MAG% cases, there is an overall increase of the median, TR and IQR when increasing the source eccentricity and decreasing the mesh resolution. If we focus on the 1 mm mesh and 0.9796 eccentricity, the RDM% median is only around 0.75%; the IQR is ≈ 0.5% and the TR reaches ≈ 4%. The median values increase from ≈ 0.75%, to ≈ 3% and ≈ 9%. We do not notice a large variation of IQR values, while the TR for dipoles of eccentricity 0.9796 increases drastically from ≈ 5% (1 mm) to almost 15% (2 mm) and 50% (4 mm). The median MAG% is extremely low, i.e., ≈ 0.004%; the IQR is ≈ 0.4% and the TR is ≈ 5%. For this eccentricity, we do not notice a huge difference among the three mesh resolutions.

In this particular case of the partial integration approach, we notice that the RDM% medians are overall below 11% for 4 mm resolution, below 5% for 2 mm and below 4% for 1 mm. The MAG% medians do not exceed 2% for 4 mm, 0.4% for 2 mm and 0.2% for 1 mm, independently of the eccentricities. In particular, when analyzing results for the most eccentric dipoles, i.e., with an eccentricity of 0.993, the RDM% and MAG% means are ≈ 4.3% and ≈ 0.5%, respectively. The medians are around 4% and 0.2%, the IQRs around 4% and 1.2% and the TRs reach ≈ 15% and ≈ 20% for RDM% and MAG%, respectively. With regard to the full B-field, similar general considerations done for the subtraction approach hold for the partial integration approach. First, we notice huge RDM% and MAG% values for the least eccentric dipoles, i.e., almost radial dipoles; second, some numerical oscillations for the 4 mm results are visible for the highest eccentricities. Overall, RDM% and MAG% means do not exceed 9.6% and 4.3% for 4 mm; 3.9% and 0.5% for 2 mm and 3.3% and 0.7% for 1 mm, respectively.

Study 3: CG-FEM and Venant's Approach

In this section, we present the results of validating the MEG forward problem solution when the CG-FEM was adopted and the right-hand side of the Poisson equation (2.4) was discretized using Venant's approach, described in Section 2.5. For the validation we compared results for 4 mm, 2 mm and 1 mm resolution meshes presented above, and 10,000 tangentially-oriented sources.

RDM% and MAG%s are evaluated both for the secondary B-field $\mathbf{B}^s$ and the full B-field $\mathbf{B}$, following equations (1.13) and (1.12), respectively. More details are in Appendix A.

Similarly to the partial integration approach, we present results for both the most reasonable eccentricity dipoles, i.e., 0.9796, and the most eccentric dipoles, i.e.,

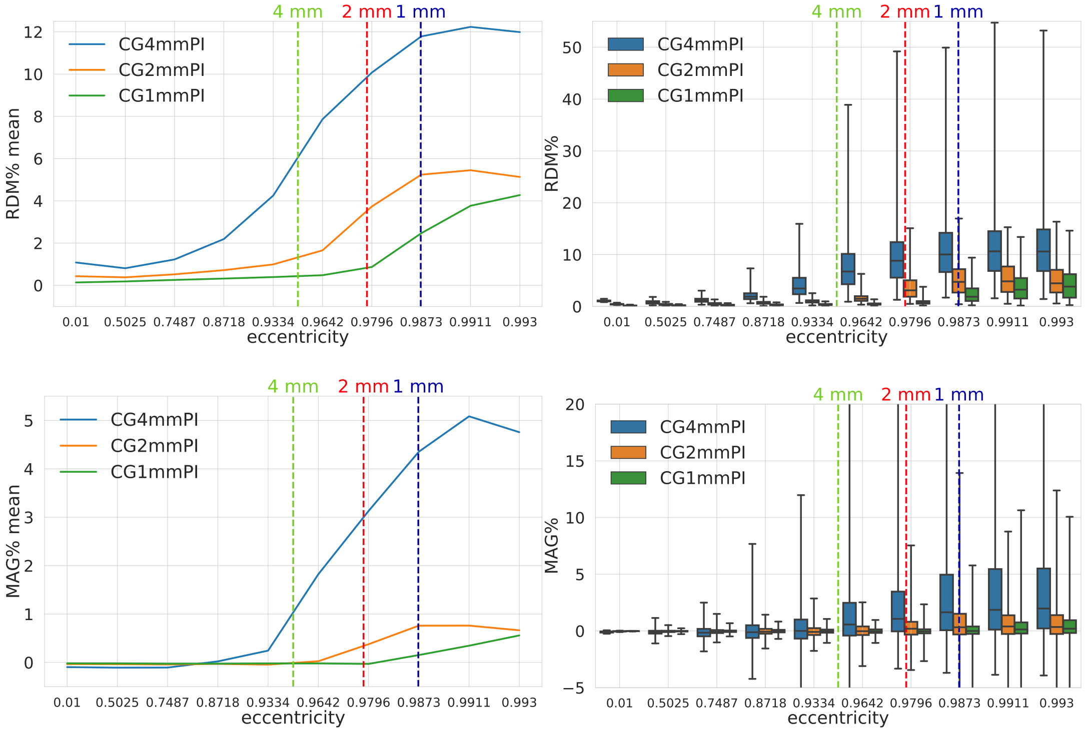

Figure 2.5.: Validation and convergence analysis for secondary B-field $\mathbf{B}^s$ computation (1.13) of CG-FEM when the *partial integration* approach is used in a 4 mm (blue), 2 mm (yellow) and 1 mm (green) hexahedral sphere model: visualized are the means (left column) and the boxplots (right column) of the RDM% (top row) and MAG% (bottom row), for tangentially oriented sources at logarithmically-scaled eccentricities. Dashed lines represent the eccentricities of 4 mm (green), 2 mm (red) and 1 mm (blue) distances to the brain-CSF boundary. Note the different scaling of the y-axes.

0.993, as in both scenarios the RDM% and MAG% results show the reliability of the method also for the most extreme scenarios.

We start with the analysis of the RDM% and MAG% results for the secondary B-field computed in a 1 mm resolution mesh, for the dipoles with eccentricity of 0.9796 and we refer to Figure 2.7. The RDM% and MAG% means are ≈ 0.74% and ≈ -0.02%, respectively. From the boxplots in the right column of Figure 2.7 we can see RDM% and MAG% medians of ≈ 0.65% and ≈ -0.025%, IQRs of around 0.5% and 0.15%, TRs of ≈ 3% and ≈ 4%, respectively. RDM% medians are drastically decreasing when increasing the resolution of the mesh: from ≈ 9% in the 4 mm resolution mesh, to ≈ 3% in the 2 mm resolution mesh and ≈

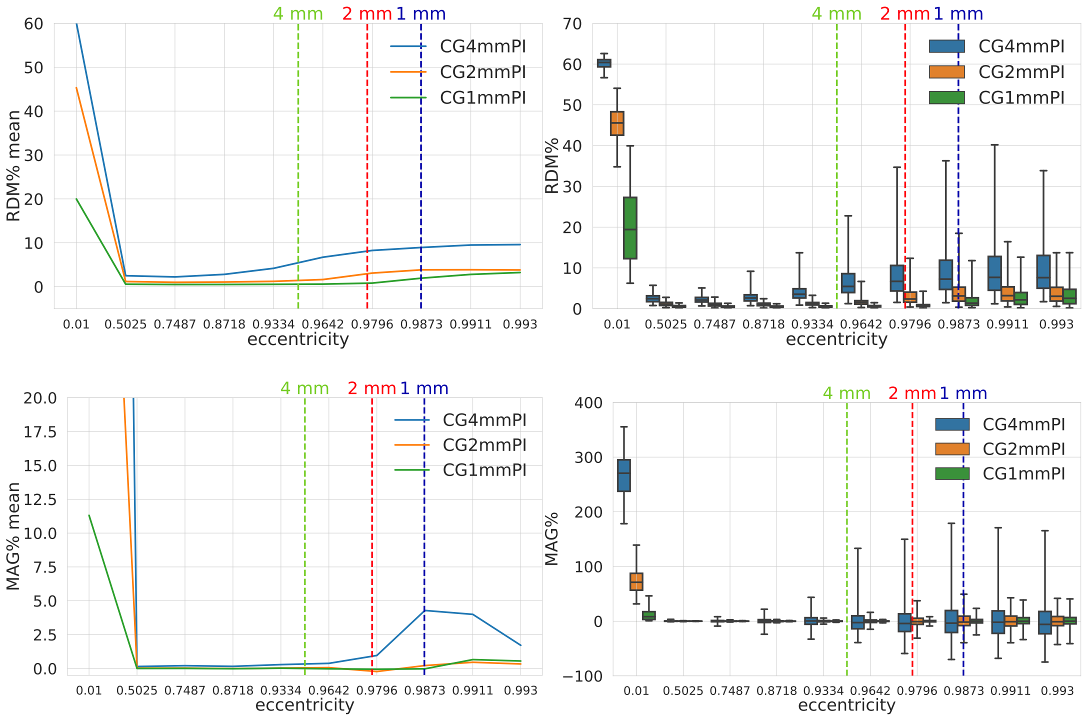

Figure 2.6.: Validation and convergence analysis for solving the MEG forward problem, i.e., the full B-field **B** (1.12), of CG-FEM when the *partial integration* approach is used in a 4 mm (blue), 2 mm (yellow) and 1 mm (green) hexahedral sphere model: visualized are the means (left column) and the boxplots (right column) of the RDM% (top row) and MAG% (bottom row), for tangentially oriented sources at logarithmically-scaled eccentricities. Dashed lines represent the eccentricities of 4 mm (green), 2 mm (red) and 1 mm (blue) distances to the brain-CSF boundary. Note the different scaling of the y-axes.

1% in the 1 mm resolution mesh. The same holds for TR values: from 30%, to 12% and 4% in a 4 mm, 2 mm and 1 mm resolution mesh, respectively. The IQR values behave similarly. The same general behavior can be noticed for MAG% boxplots, even if the maximum upper quartile remains below 5%.

When we analyze results for the most eccentric dipoles, we first of all notice that the performance of Venant's approach is very high. The mean RDM% and MAG% are ≈ 0.74% and ≈ -0.02%, respectively. The RDM% and MAG% medians are around 2.5% and 0.07%, the IQRs are approximately 3.5% and 0.7%, the TRs are ≈ 12% and 20%. The overall RDM% and MAG% means do not exceed 12% and 4.5% for the 4 mm resolution mesh; 4.4% and 0.5% for the 2 mm resolution mesh and 3.2% and 0.3% for the 1 mm resolution mesh. In particular we observe that MAG% errors are extremely low, independently of the mesh resolution or dipole position. Also for the full B-field the solutions are extremely accurate, when excluding the analysis of the innermost dipoles, due to their radial orientation. The overall RDM% and MAG% mean values do not exceed 9.2% and 2.1% for the 4 mm resolution mesh; 3.3% and 0.3% for the 2 mm resolution mesh and 2.3% and 0.6% for the 1 mm resolution mesh, respectively.

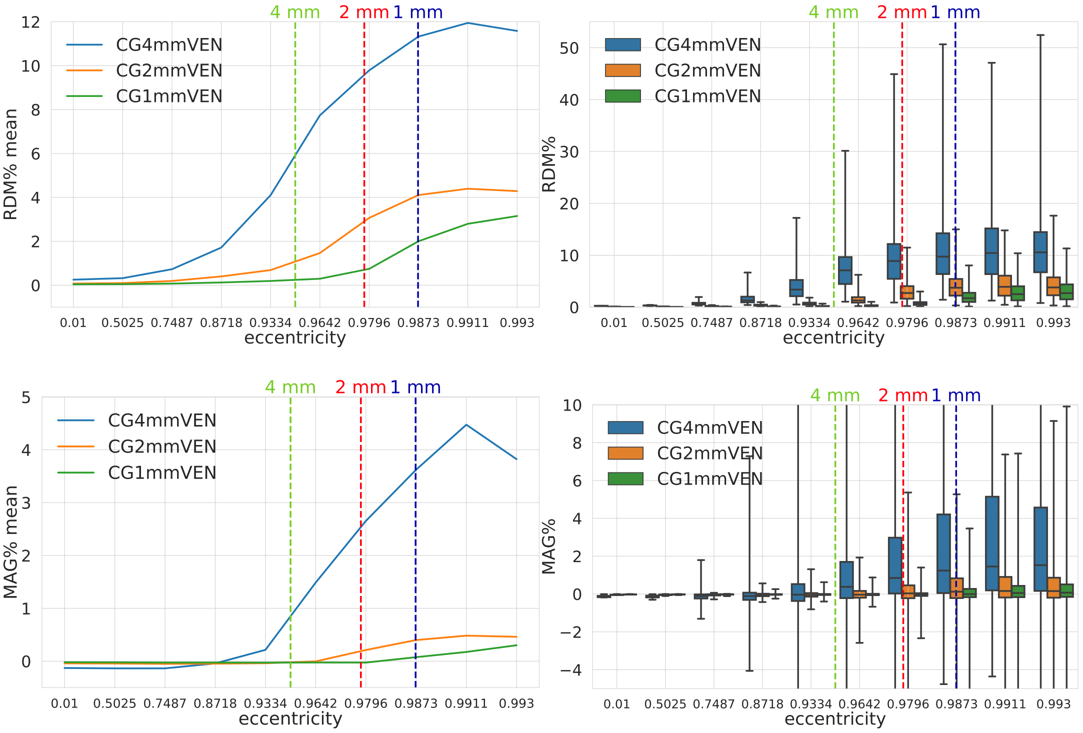

Figure 2.7.: Validation and convergence analysis for secondary B-field $\mathbf{B}^s$ computation (1.13) of CG-FEM when the *Venant's* approach is used in a 4 mm (blue), 2 mm (yellow) and 1 mm (green) hexahedral sphere model: visualized are the means (left column) and the boxplots (right column) of the RDM% (top row) and MAG% (bottom row), for tangentially oriented sources at logarithmically-scaled eccentricities. Dashed lines represent the eccentricities of 4 mm (green), 2 mm (red) and 1 mm (blue) distances to the brain-CSF boundary. Note the different scaling of the y-axes.

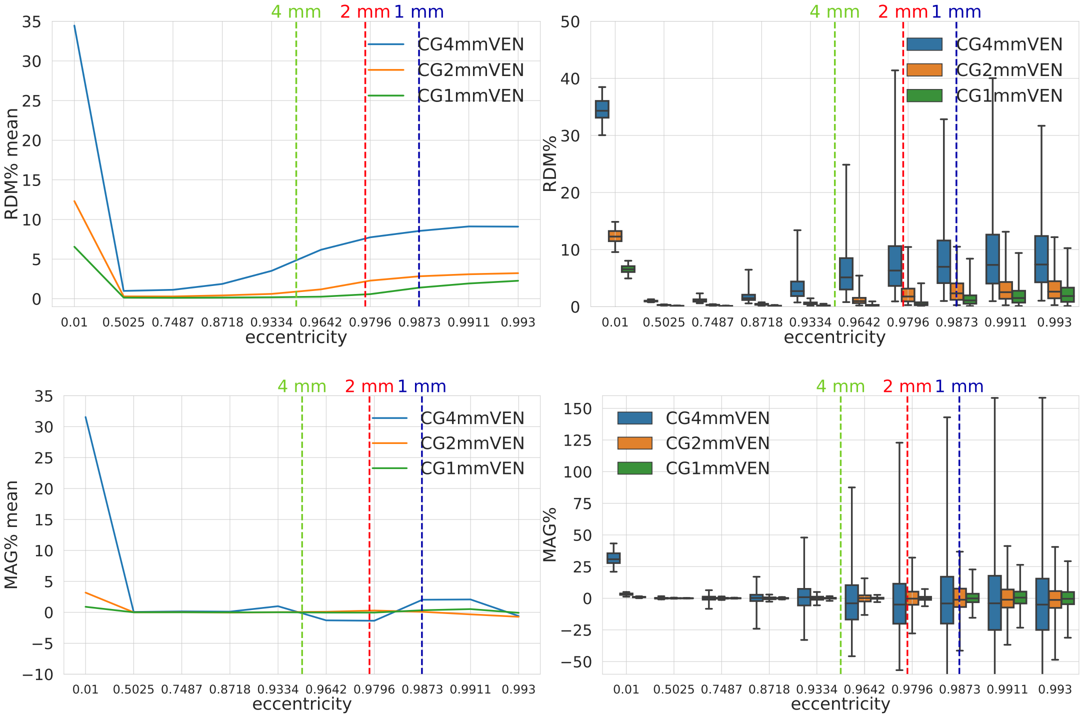

Figure 2.8.: Validation and convergence analysis for solving the MEG forward problem, i.e., the full B-field **B** (1.12), of CG-FEM when the *Venant's* approach is used in a 4 mm (blue), 2 mm (yellow) and 1 mm (green) hexahedral sphere model: visualized are the means (left column) and the boxplots (right column) of the RDM% (top row) and MAG% (bottom row), for tangentially oriented sources at logarithmically-scaled eccentricities. Dashed lines represent the eccentricities of 4 mm (green), 2 mm (red) and 1 mm (blue) distances to the brain-CSF boundary. Note the different scaling of the y-axes.

Study 4: CG-FEM Comparison between Different Source Models

In this section we compare the accuracy of all the three approaches we described to discretize the right-hand side of the Poisson equation, namely the subtraction approach (SA), the partial integration approach (PI) and Venant's approach (VEN), for each mesh resolution, namely 4, 2 and 1 mm resolution meshes, see Table A.2. We computed and visualized RDM% and MAG% for both the secondary and full B-field, for 10,000 tangentially oriented dipoles at 10 logarithmically-scaled eccentricities.

In Figure 2.9, the secondary B-field results corresponding to the 4 mm resolution mesh are reported.
As a general remark about RDM% values, we observe that VEN and SA perform almost in an identical way until the eccentricity of 0.9334, i.e., the eccentricity which corresponds to the brain-CSF boundary layer in the 4 mm mesh. For higher eccentricities, SA RDM% values are much higher than those of PI and VEN, which perform almost identically. The difference in RDM% mean between SA and PI/VEN reaches 15 *percentage points* (pp). Note that for eccentricities higher than 0.9334, all of the three approaches lead to RDM% values above 5%, therefore the accuracy of the method is lower independently of the approach used for the discretization of the right-hand side.
With regard to the MAG% values, the general behavior is the following. For eccentricities smaller than 0.9334, the three approaches deliver MAG% values whose differences are negligible. On the contrary, for eccentricities higher than 0.9334, the SA performs worse than PI and VEN, reaching differences up to 180 pp, when considering the means. However, these values are out of the displayed graph range. PI and VEN behave similarly, with a slightly better performance of VEN, i.e., with a difference up to 1 pp in mean.
As expected, the main increase of RDM% and MAG% occurs when dipoles approach the boundary layer of hexahedra between brain and CSF compartments, i.e., dipoles with eccentricities higher than 0.9334. From Figure 2.9, it is remarkable how PI and VEN perform better than SA already at the eccentricity of 0.9642, where many outliers are visible in the TRs of Figure 2.9, right column. On the other side, when considering dipoles with eccentricities lower than 0.9334, we can notice how both RDM% mean and median of the PI method are performing slightly worse than both SA and VEN, which are behaving identically. In particular, the RDM% mean is ≈ 1 pp higher for the PI approach (Figure 2.9, top left).
The behavior of PI for less eccentric dipoles is even more visible for the full B-field results in Figure 2.10, where RDM% mean and median reach 60%. SA is not delivering reliable results for very high eccentricities, but also PI and VEN have high errors in such a low-resoluted mesh. In general, the 4 mm resolution sphere model is too coarse to have accurate results and this is valid for every discretization approach considered in this study.

Next comparison involves a 2 mm resoluted spherical mesh, and the three

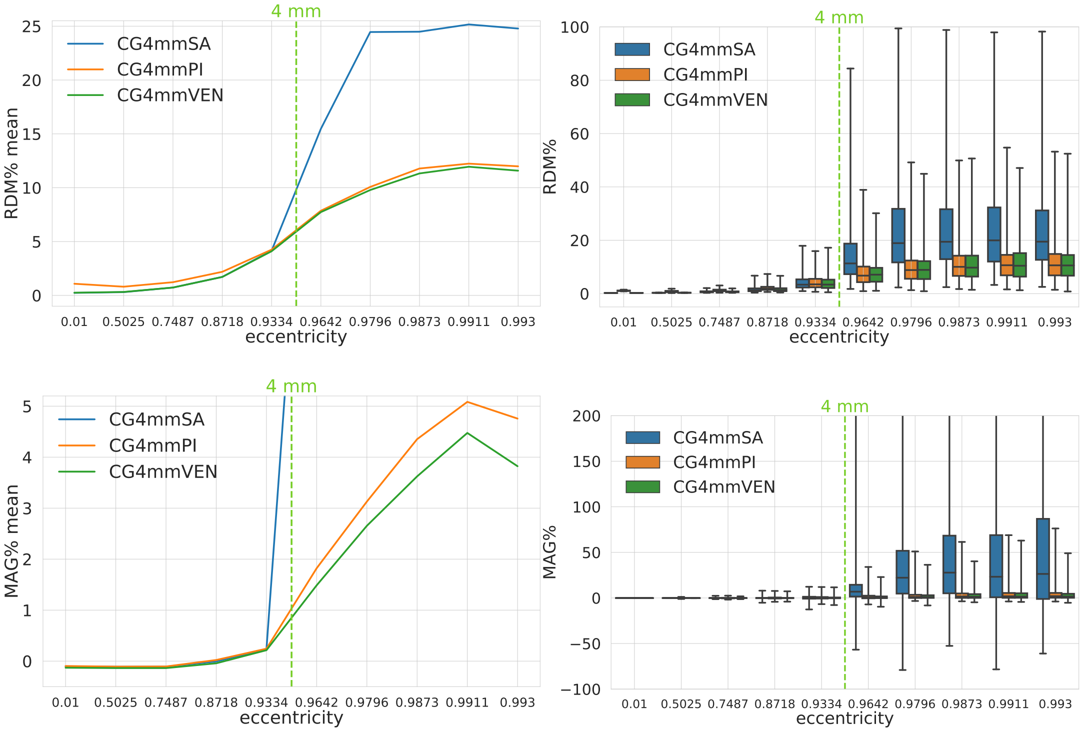

Figure 2.9.: Accuracy comparison of the secondary B-field $\mathbf{B}^s$ computation (1.13) of CG-FEM when the subtraction (blue), the partial integration (yellow) and Venant's (green) approaches are used in a 4 mm hexahedral sphere model: visualized are the means (left column) and the boxplots (right column) of the RDM% (top row) and MAG% (bottom row), for tangentially oriented sources at logarithmically-scaled eccentricities. The green dashed line represents the eccentricity of 4 mm distance to the brain-CSF boundary. Note the different scaling of the y-axes.

right-hand side discretization procedures already mentioned before, i.e., SA, PI and VEN.

Main considerations already presented for the 4 mm case are valid also in this scenario. In particular, first, we see that from the boundary-eccentricity of 0.9796, in this case, errors for all the three approaches are drastically increasing and the highest increase is visible for SA, both for the secondary and full B-field, in Figures 2.11 and 2.12, respectively. With regard to the secondary B-field, the difference between SA and VEN reaches 8 pp for RDM% mean values and almost 80 pp for MAG% mean values. Second, PI behaves topographically slightly worse for lower eccentricities and this behavior is enhanced when looking

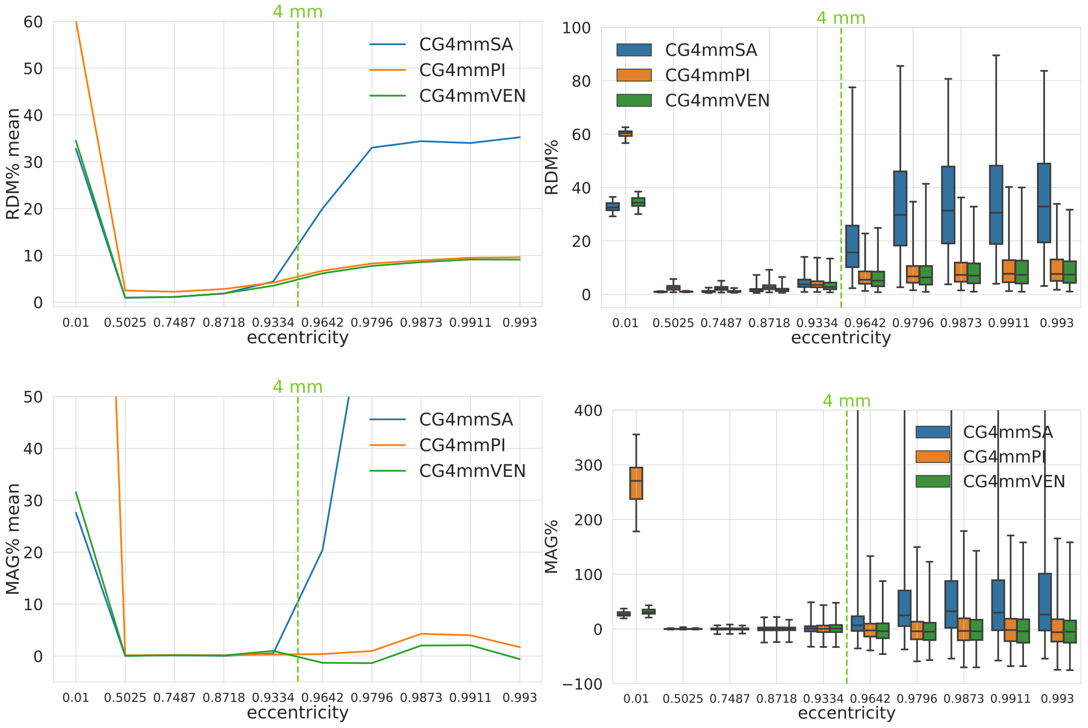

Figure 2.10.: Accuracy comparison for solving the MEG forward problem, i.e., the full B-field **B** (1.12), of CG-FEM when the subtraction (blue), the partial integration (yellow) and Venant's (green) approaches are used in a 4 mm hexahedral sphere model: visualized are the means (left column) and the boxplots (right column) of the RDM% (top row) and MAG% (bottom row), for tangentially oriented sources at logarithmically-scaled eccentricities. The green dashed line represents the eccentricity of 4 mm distance to the brain-CSF boundary. Note the different scaling of the y-axes.

at full B-field results. The difference between PI and VEN is around 0.5 pp. Third, for eccentricities higher than 0.9796, VEN slightly outperforms PI both topographically and in magnitude, with a difference of around 1 pp and lower than 0.5 pp, when considering the RDM% and MAG% means, respectively.

From the boxplots of Figure 2.11, we observe that, for high eccentricities, TRs of SA are up to 80 pp higher than TRs of PI, and SA IQR values up to 7 times higher than PI IQR values. On the other side, for less eccentric dipoles, PI TR values are up to 5 times SA TR values and PI IQRs are the double of SA IQRs. The fact that PI performs worse for almost radially oriented dipoles in the secondary B-field leads to extremely high RDM% and MAG% values for the full B-field which are visible in Figure 2.12.

When the 1 mm resolution mesh is used and the discretization approaches are

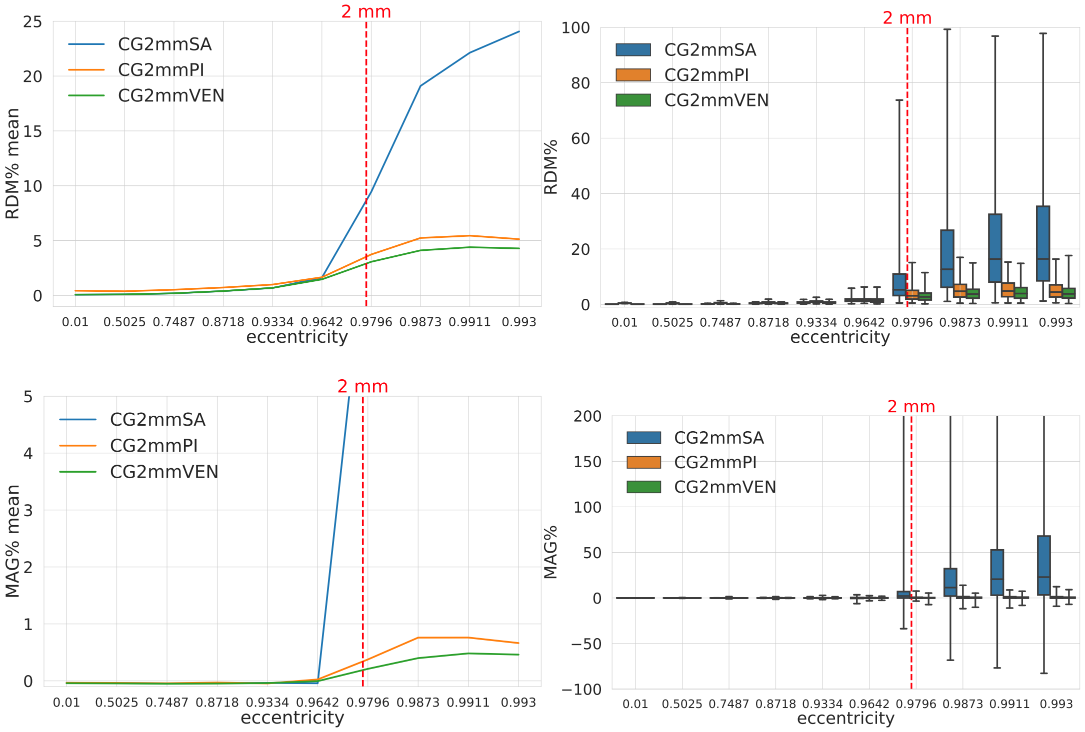

Figure 2.11.: Accuracy comparison of the secondary B-field $\mathbf{B}^s$ computation (1.13) of CG-FEM when the subtraction (blue), the partial integration (yellow) and Venant's (green) approaches are used in a 2 mm hexahedral sphere model: visualized are the means (left column) and the boxplots (right column) of the RDM% (top row) and MAG% (bottom row), for tangentially oriented sources at logarithmically-scaled eccentricities. The red dashed line represents the eccentricity of 2 mm distance to the brain-CSF boundary. Note the different scaling of the y-axes.

compared, we again face the same scenario described for 4 and 2 mm, even if differences are slightly attenuated in this case.

In more details, when looking at the RDM% boxplot in Figure 2.13, right column, we see that for eccentricity of 0.9873, i.e., the 1 mm boundary-eccentricity, the SA median is almost the double as the VEN median; SA IQRs are the double as VEN IQRs and SA TRs are more than 4 times larger than VEN TRs. With regard to MAG%, already for the eccentricity of 0.9796 we see that PI and VEN are better than SA and VEN is better than PI. The corresponding medians are not differing in a remarkable sense, but SA IQRs are almost 5 times higher than

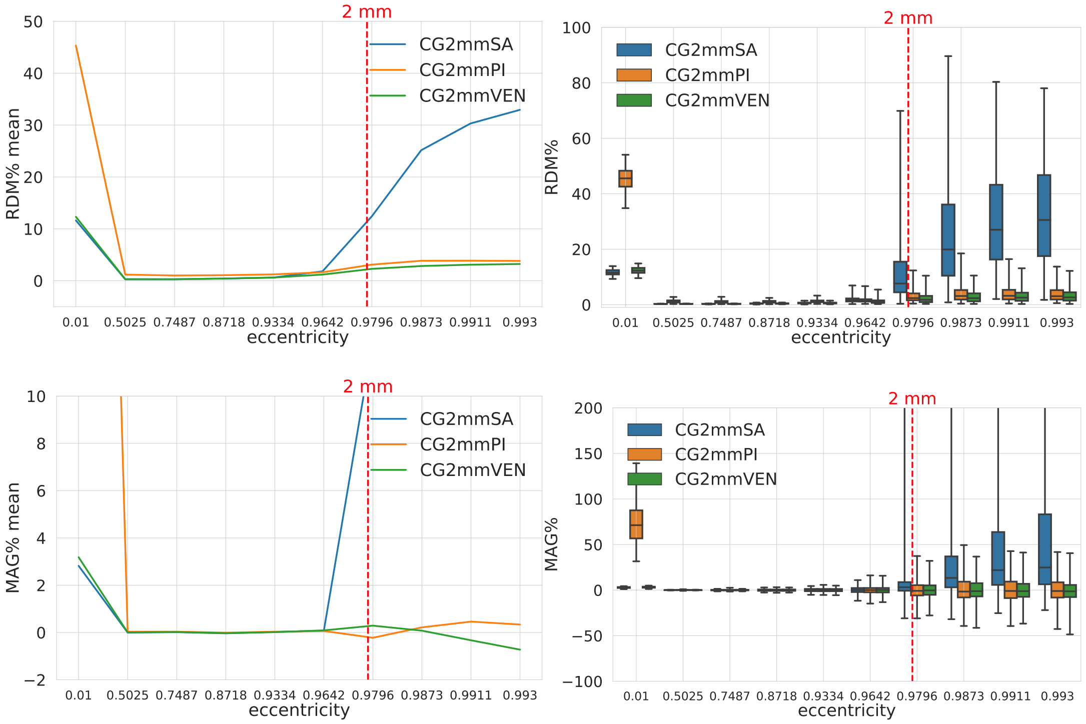

Figure 2.12.: Accuracy comparison for solving the MEG forward problem, i.e., the full B-field **B** (1.12), of CG-FEM when the subtraction (blue), the partial integration (yellow) and Venant's (green) approaches are used in a 2 mm hexahedral sphere model: visualized are the means (left column) and the boxplots (right column) of the RDM% (top row) and MAG% (bottom row), for tangentially oriented sources at logarithmically-scaled eccentricities. The red dashed line represents the eccentricity of 2 mm distance to the brain-CSF boundary. Note the different scaling of the y-axes.

VEN IQRs and SA TR values are approximately the double of VEN TRs. From Figure 2.13, left column, we see that, for eccentric dipoles, the difference between SA and PI RDM% means reaches 20 pp, while the difference between PI and VEN is around 1 pp; the MAG% difference between SA and VEN is more than 70 pp and there is no relevant difference between MAG% PI and VEN. On the other hand, for low eccentricities the difference between the three methods in terms of mean RDM% and MAG% are present but negligible.

When the full B-field is compared for different right-hand side discretizations in the 1 mm resolution mesh, in general, the errors are remarkably smaller and the differences between approaches are less underlined. Still, when looking at the RDM% boxplots in Figure 2.14, we see that VEN performs better than

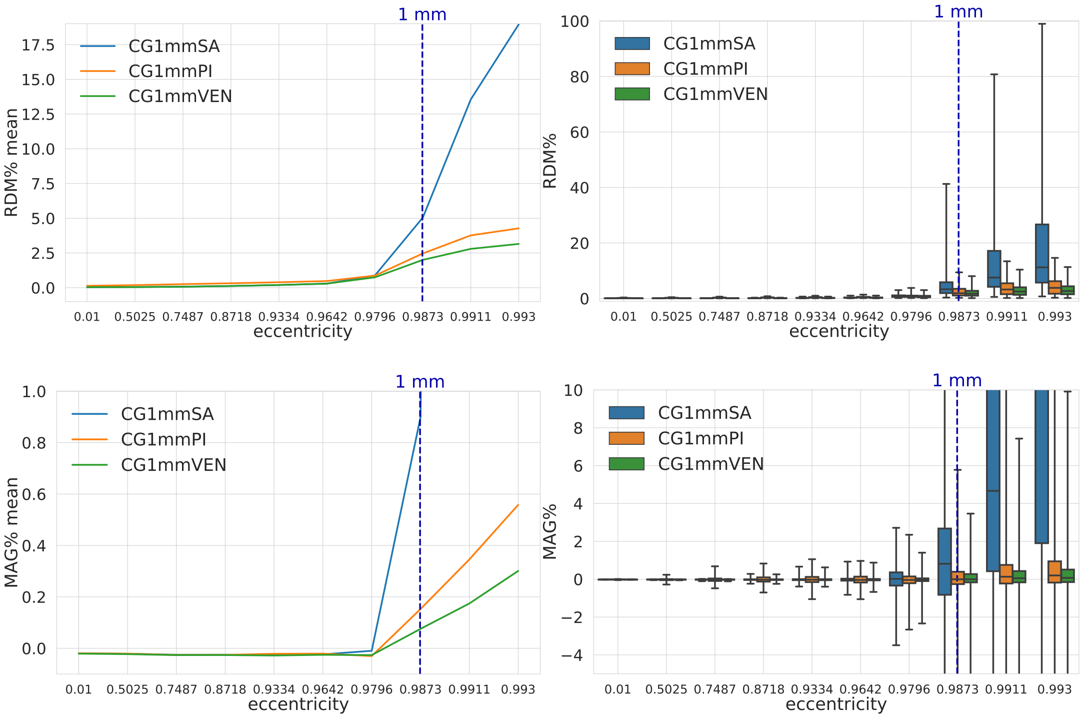

Figure 2.13.: Accuracy comparison of the secondary B-field $\mathbf{B}^s$ computation (1.13) of CG-FEM when the subtraction (blue), the partial integration (yellow) and Venant's (green) approaches are used in a 1 mm hexahedral sphere model: visualized are the means (left column) and the boxplots (right column) of the RDM% (top row) and MAG% (bottom row), for tangentially oriented sources at logarithmically-scaled eccentricities. The blue dashed line represents the eccentricity of 1 mm distance to the brain-CSF boundary. Note the different scaling of the y-axes.

PI and SA for very eccentric dipoles, and PI delivers worse results than VEN and SA for lower eccentricities. Both PI and VEN are reliable approaches for extremely eccentric dipoles, as the RDM% remains below $\approx 2.5\%$. In general, MAG% values are very low. PI performs worse only for the eccentricity of 0.01, and the three methods are almost identical. For the eccentricity of 0.9796, SA performs slightly better. For the most eccentric dipoles, the absolute value of MAG% PI and VEN is always below 0.5%. With regard to RDM% mean values, PI values are approximately 0.5 pp worse than SA and VEN values for low eccentricities, while the difference between SA and VEN values is more than 20 pp for the highest eccentricity. With regard to MAG% mean values, we notice some numerical oscillations for high eccentricities in combination with VEN. The difference between SA and VEN values are again very high, reaching 60 pp.

Finally, in Figure 2.15 and 2.16 there is a comparison among all different source

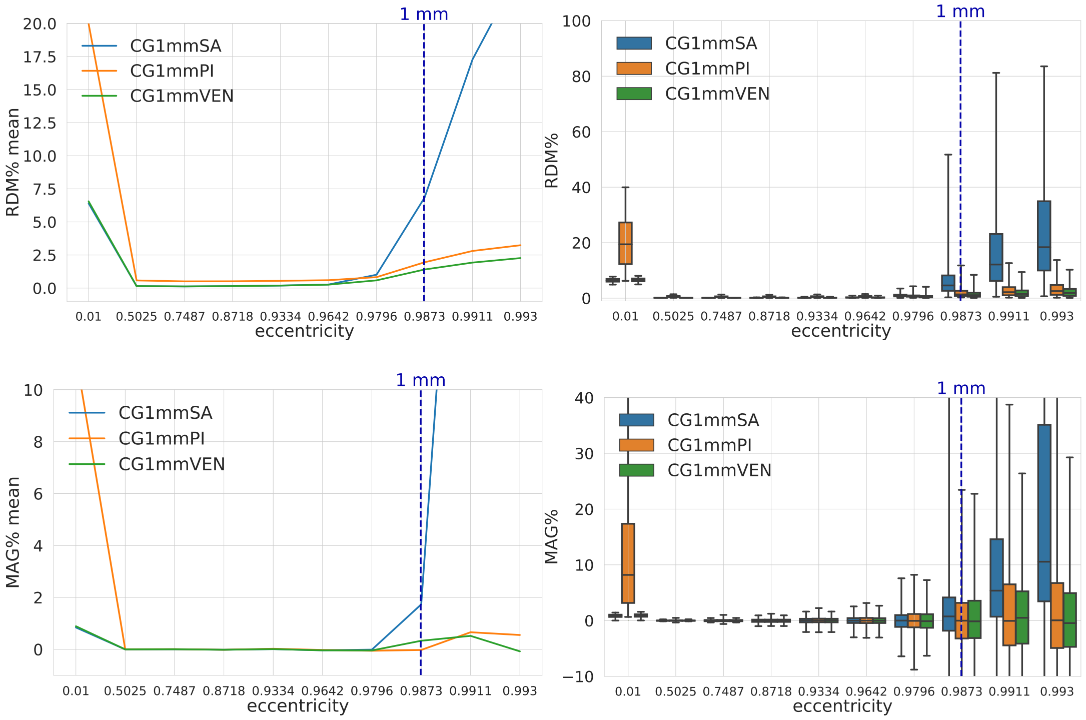

Figure 2.14.: Accuracy comparison for solving the MEG forward problem, i.e., the full B-field **B** (1.12), of CG-FEM when the subtraction (blue), the partial integration (yellow) and Venant's (green) approaches are used in a 1 mm hexahedral sphere model: visualized are the means (left column) and the boxplots (right column) of the RDM% (top row) and MAG% (bottom row), for tangentially oriented sources at logarithmically-scaled eccentricities. The blue dashed line represents the eccentricity of 1 mm distance to the brain-CSF boundary. Note the different scaling of the y-axes.

discretizations, i.e., SA, PI and VEN and all different mesh resolutions, i.e., 4 mm, 2 mm and 1 mm, for the secondary and full B-fields, respectively.

The comparison is visualized by means of the so called cumulative relative frequencies, i.e., the ordinate of each point of a curve indicates the amount of sources that has an error below the respective abscissa value. The best method is therefore the one whose RDM% and MAG% graphs are the closest to the zero vertical line.

From Figure 2.15 we observe that the overall most accurate method is VEN in a 1 mm resolution mesh. We can indeed observe that more than 95% of the dipoles have an RDM% of 4.4 and a MAG% between -0.3% and 0.6%. The curve for PI 1 mm does not differ much from the one for VEN 1 mm, but 95% of the sources have RDM% of 9% and MAG% between approximately -0.4% and 2%. VEN 2 mm, PI 2 mm and SA 1 mm follow with similar and still high performances. In general, the curve corresponding to SA is very steep for very low RDM% and MAG% values and then it grows slowly, reaching the 95% dashed line almost always for RDM% and MAG% values higher than 10% and 8%, respectively. On the other side, PI and VEN curves have a less steep behavior for the smallest RDM% and MAG% values, but they reach higher values faster for higher RDM% and MAG% values. A similar general behavior is observed for the full B-field and omitted in this section.

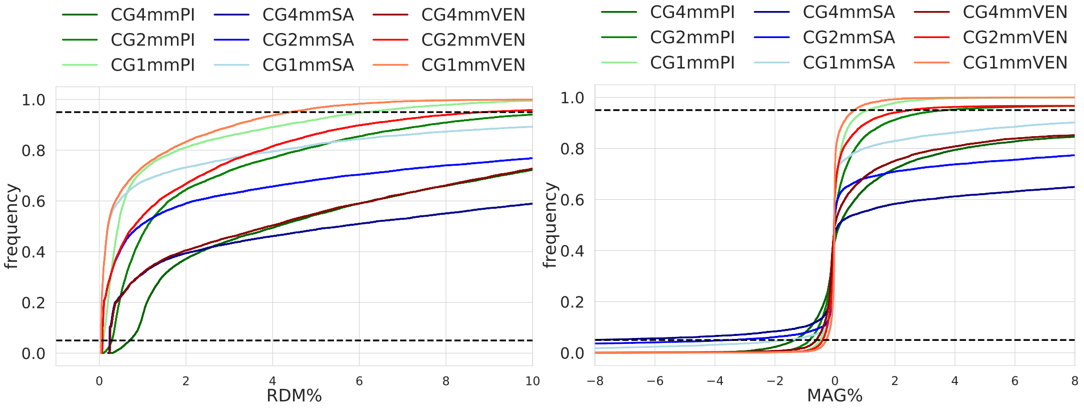

Figure 2.15.: Cumulative relative frequencies of RDM% (on the left) and MAG% (on the right) of the secondary B-field $\mathbf{B}^s$ (1.13) computed with CG-FEM for tangentially oriented sources at logarithmically-scaled eccentricities for three different source models, i.e., subtraction approach (SA) (in blue), partial integration approach (PI) (in green) and Venant's approach (VEN) (in red), and three different mesh resolutions, i.e., 4 mm, 2 mm and 1 mm. The dashed horizontal lines depict the frequencies of 5% and 95%.

Study 5: CG-FEM and the Boundary Subtraction Approach

In this section we study the performances of CG-FEM for computing the secondary component of the B-field when the boundary formulation of Biot-Savart's

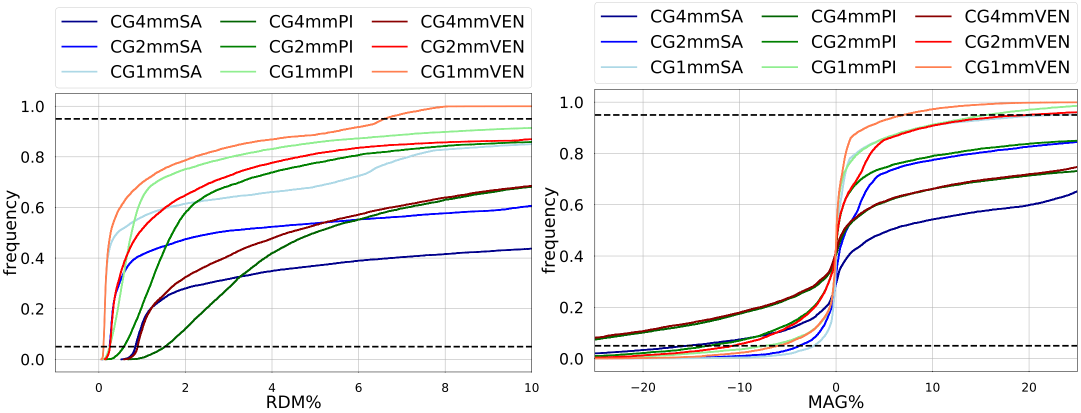

Figure 2.16.: Cumulative relative frequencies of RDM% (on the left) and MAG% (on the right) of the MEG forward problem solution, i.e., the full B-field $\mathbf{B}$ (1.12), computed with CG-FEM for tangentially oriented sources at logarithmically-scaled eccentricities for three different source models, i.e., subtraction approach (SA) (in blue), partial integration approach (PI) (in green) and Venant's approach (VEN) (in red), and three different mesh resolutions, i.e., 4 mm, 2 mm and 1 mm. The dashed horizontal lines depict the frequencies of 5% and 95%.

law for the subtraction approach introduced in Section 2.6 is used. First, we analyzed the influence of the numerical integration of $\mathbf{B}^s_\infty$ (*intBinf*, following the definition of DUNE) and the one of the size of the patch representing Ω^∞ (*extens*) (see 2.26) on the accuracy of the solution. Second, we compared the accuracy of the boundary formulation 2.26 and the standard volumetric formulation 2.21-2.22 of Biot-Savart's law for computing the secondary B-field. We therefore performed two simulation tests in a 2 mm sphere model (see details in the Appendix A) where we computed $\mathbf{B}^s$ for 1,000 tangentially oriented dipoles (a subset of dipoles presented in Appendix A) in 256 point-magnetometers with three Cartesian orientations each. We compared then numerical results with the analytical solutions by computing RDM% and MAG% medians.

In the first simulation we fixed *intBinf* to 2 and we let the size of the patch vary. Starting from the single element where the dipole is located, we extended the patch by including the elements which are sharing a vertex with the already considered element of the patch. In this simulation we considered 0, 1, 2 and 3 extensions. From Figure 2.17, we see that RDM% and MAG% medians when only the single element where the dipole is located are very high, whereas when

1,2 or 3 extensions have been considered RDM% and MAG% medians are almost identical. We therefore deduce that it is fundamental to have a patch that has at least one extension, meaning that the patch should at least contains $3^3 = 27$ elements.

In the second simulation we fixed *extens* to 1 and considered *intBinf* equal to 2,3 and 4. From the results visualized in Figure 2.18, we deduce that *intBinf* should be at least 2, and as the computational cost is quite high (see Figure 2.19) we recommend not to exceed 2.

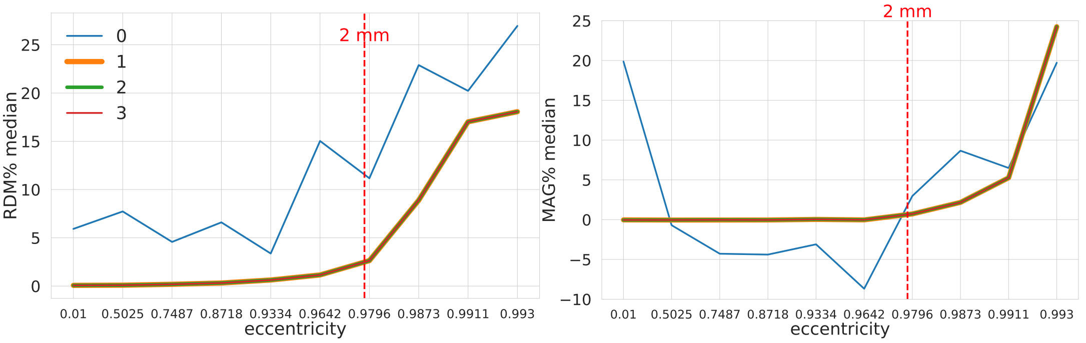

Figure 2.17.: RDM% (on the left) and MAG% (on the right) medians of the secondary B-field $\mathbf{B}^s$ (1.13) computed with CG-FEM for 1,000 tangentially oriented sources for three different patch sizes: 1, 3^3,5^3,7^3, corresponding to 0,1,2 and 3 extensions of the patch composed by the single element of the dipole.

Finally, we compared the secondary B-field computed via the standard Biot-

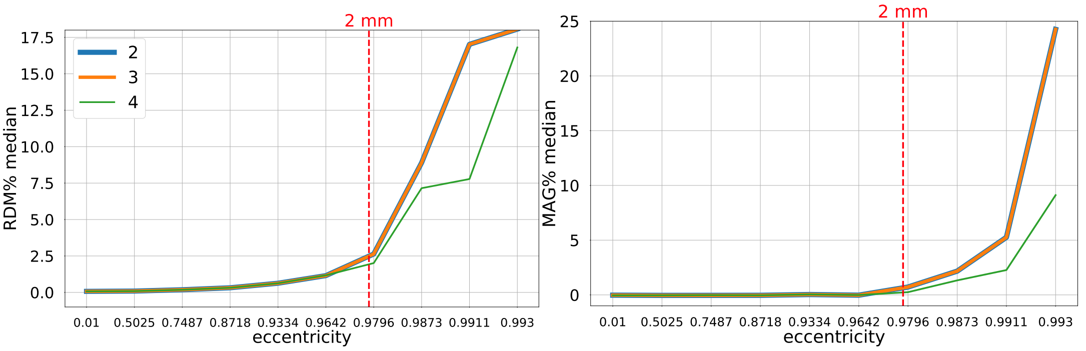

Figure 2.18.: RDM% (on the left) and MAG% (on the right) medians of the secondary B-field $\mathbf{B}^s$ (1.13) computed with CG-FEM for 1,000 tangentially oriented sources for three different integration order for computing B^s_∞ (from 2 to 4).

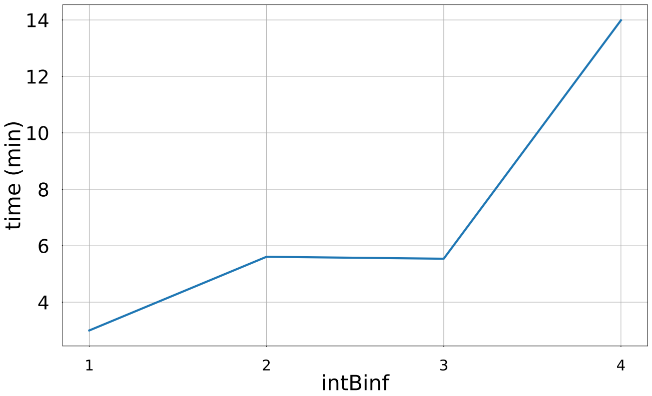

Figure 2.19.: Computational time (in minutes) for computing the secondary B-field $\mathbf{B}^s$ (1.13) with CG-FEM for different integration order for B^s_∞ (from 1 to 4).

Savart's law formulation and the one computed via the boundary formulation of Biot-Savart's law. We conducted this comparison in a 2 mm sphere model, 10,000 tangentially oriented dipoles and 256 point-magnetometers described in A.1 and A.2, respectively. Results are reported in Figure 2.20, where RDM% and MAG% boxplots and medians are shown.

The boundary subtraction approach leads to overall more accurate results for eccentricities greater or equal to 0.9642 in terms of both RDM% and MAG% errors.

In contrast, RDM% and MAG% errors are almost identical for lower eccentricities.

In particular, for most eccentric dipoles, RDM% and MAG% means are up to 10 pp and more than 60 pp lower, respectively (Figure 2.20, on the left). When studying Figure 2.20, on the right, we see that RDM% medians are up to 6 pp lower when the boundary formulation is used. Both IQR and TR are remarkably reduced. In MAG% boxplots the most visible gain in accuracy when adopting the boundary formulation is shown. MAG% medians are almost 20 pp lower reaching a maximum value of $\approx 3.3\%$. IQRs are up to almost 50 pp smaller and TRs behave similarly.

Since we wanted to compare the numerical performance of the boundary subtraction approach, we limited our analysis to the secondary component of the B-field.

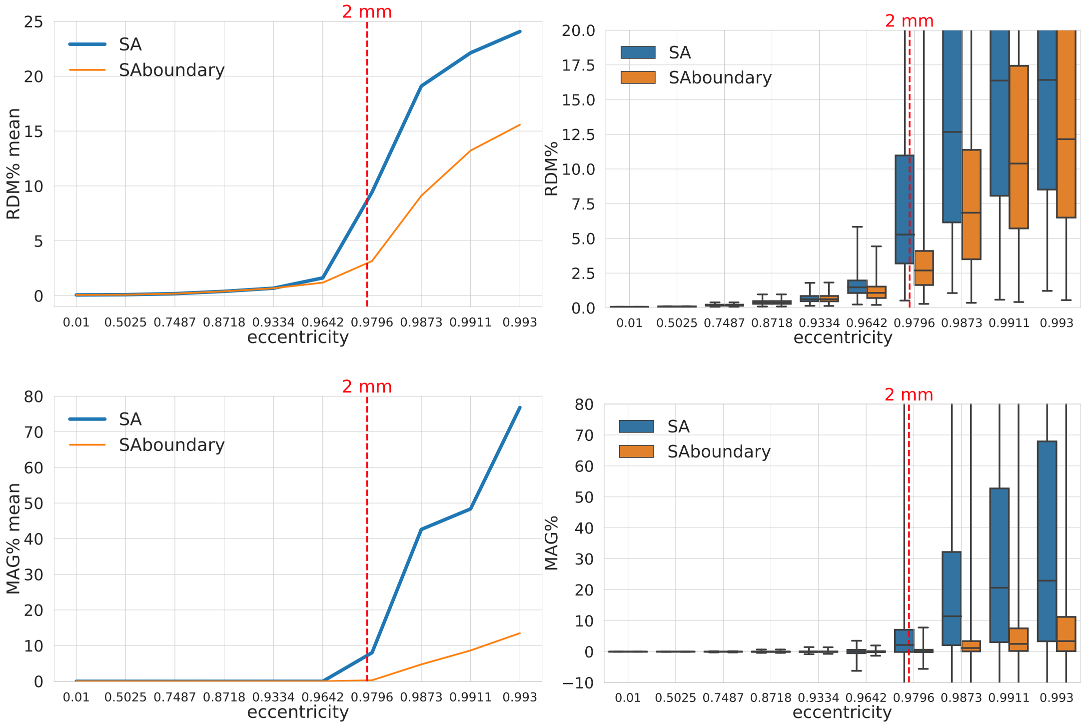

Figure 2.20.: Accuracy comparison of the secondary B-field $\mathbf{B}^s$ computation (1.13) of CG-FEM when the standard subtraction (blue) and the boundary subtraction approaches (yellow) are used in a 2 mm hexahedral sphere model: visualized are the means (left column) and the boxplots (right column) of the RDM% (top row) and MAG% (bottom row), for tangentially oriented sources at logarithmically-scaled eccentricities. The red dashed line represents the eccentricity of 2 mm distance to the brain-CSF boundary. Note the different scaling of the y-axes.

2.8. Conclusions

This chapter is about how we developed, implemented and evaluated the CG-FEM for solving the MEG forward problem. First, we introduced and summarized the main mathematical theory of the CG-FEM. Second, we introduced the CG-FEM discretization of the weak EEG forward problem formulation in its general case. Third, we described three possible ways to deal with the dipolar representation of the source, namely the subtraction approach, the partial integration approach, and Venant's approach, and for each approach we presented the discrete CG right-hand side formulation. Fourth, we deduced the MEG CG discrete representation of the general case, together with each source discretization approaches and we discussed some implementation aspects as the transfer matrix approach. Fifth, the CG-FEM for solving the MEG forward problem was evaluated and results gathered and visualized in boxplots, mean curves and cumulative relative frequency curves.

In a first analysis, we tested and visualized the symmetry properties of the MEG analytical solution for a multi-layer homogeneous sphere model, as described in Remark 1 and as proven by [78]. First of all, radial sources have a zero magnetic field outside a multi-layer sphere volume conductor model. Then, for tangential sources, only the primary B-field contributes to the full B-field for radial point-magnetometers (Figure 2.1a). For tangential sources and tangential point-magnetometers, we additionally showed that the more eccentric the source is, the more its primary B-field contributes to the full B-field relative to the contribution of the secondary B-field. The deeper the tangential source is, the more the secondary B-field weakens the primary B-field until for sources in the center of the sphere model, where the primary and secondary B-fields totally compensate for each other (Figure 2.2 together with Figure 2.1b). In contrast, the more eccentric the sources are, the less symmetric the return currents are and the less their secondary B-field compensates the magnetic field of the primary current (Figure 2.2). This is in line with the fact that the strength of the full B-field for both radial and tangential magnetometers is decreasing for decreasing eccentricities (Figure 2.1b), as expected by the theory where it is proven that MEG sensors are blind for radial sources [78]. In a second analysis, we studied the convergence of the CG-FEM for each discretization of the dipolar source, namely the subtraction approach (SA), the partial integration approach (PI) and Venant's approach (VEN). Subsequently, the performances of CG-FEM for all the three discretization schemes were compared. We visualized RDM% and MAG% values both for the secondary and full B-field. As a final study, we tested and compared a boundary formulation of Biot-Savart's law when computing $\mathbf{B}^s_\infty$ (boundary SA) with the standard volumetric formulation (SA). The general behavior of results can be summarized throughout the following points:

- CG-FEM for solving the MEG forward problem converges: when increasing the mesh resolution, the results get better;

- errors increase for increasing eccentricity. The convergence of the CG-FEM when the SA is used depends on the vicinity of the dipole to the brain-CSF boundary, as studied in details in [96]. We could assume that similar considerations apply for PI and VEN;

- with regard to the secondary B-field, there is a strong increase of RDM% and MAG% values when the considered dipoles belong to the boundary layer of elements between brain and CSF;

- the full B-field has high errors for dipoles with a low eccentricity. The more the dipoles approach the center of the sphere, the more their orientations become radial. It is well known (see Remark 1) that the full B-field is silent for radial dipoles, therefore there are divisions by zero in the error measures, which lead to high RDM% and MAG% values;

- for the most relevant sources, i.e., dipoles with eccentricity of 0.9796, and the mesh with highest resolution (1 mm), the minimum mean RDM% value of 0.87% is reached when the PI is adopted, while the minimum mean MAG% value of -0.01% is reached when the SA is adopted;

- a spherical model with 4 mm resolution is too coarse and the results delivered are not accurate, i.e., median and mean RDM% and MAG% are way above 5%;

- a spherical model with 2 and 1 mm resolution is such that the delivered results are accurate, i.e., median and mean RDM% and MAG% are always below approximately 5%;

- SA and VEN perform better than PI for eccentricities lower than the boundary-eccentricities, i.e., the eccentricities of the distances to the brain-CSF boundary, for each mesh resolution;

- PI and VEN perform better than SA for eccentricities higher than the boundary-eccentricity;

- VEN performs better than PI for eccentricities higher than the boundary-eccentricity;

- for the boundary SA a patch with a least 27 elements and a quadrature rule with integration order of 2 for B^s_∞ should be adopted;

- the boundary SA outperforms the standard formulation of SA for eccentricities higher or equal to the boundary-eccentricity.

A similar comparison has been delivered in [86], where SA, PI and VEN CG-FEM computations of the magnetic secondary and full flux are compared in one tetrahedral and in one hexahedral mesh. A precise comparison between this study and the content of this chapter is not easy to conduct as they computed the magnetic flux by integrating the magnetic vector potential along the contour of the coils, with only a tangential orientation, while in our study we compare all the three Cartesian components of the B-field. Nevertheless, we clearly see similarities in the general behavior. For example, PI and VEN perform better than SA for high eccentricities, while SA and VEN perform better than PI for lower eccentricities. Furthermore, for high eccentricities, the errors of the full flux get very high.

To the best of our knowledge, not many recent studies on finite element methods applied to solve the MEG forward problem have been presented.
[82] applied a CG-FEM approach in a 10 cm single-layer homogeneous sphere model and RDM% errors were measured. The minimum RDM% found by these authors for far less eccentric sources of 0.95 was 3%. Still, the comparison is not straightforward because of the different approaches, the different element meshes (tetrahedra versus hexahedra), and the different source models which have been used. In general, tetrahedral meshes can better approximate surfaces but, for realistic head models, the generation of such models is difficult in practice and might cause unrealistic model features, e.g., holes in tissue compartments such as the foramen magnum and the optic canals in the skull are often artificially closed to allow constrained Delaunay tetrahedralization (CDT). Furthermore, CDT modeling necessitates the generation of nested, non-intersecting, and non-

touching surfaces. However, in reality, surfaces might touch, for example, the inner skull and the outer brain surfaces. Hexahedral models, as investigated here, have larger geometry approximation errors, but do not suffer from the above limitations and can be easily generated from voxel-based MRI data. However, with new methods like in [65], such geometry approximation errors can be avoided without the need of generating geometry conforming tetrahedral meshes.

[83] used both a sphere model and a realistically shaped model. In both cases only three compartments were modeled, namely the brain, the skull and the scalp (brain and scalp with the same conductivity values, and skull with a 1:80 conductivity ratio). The authors used a lower amount of sources and lower mesh resolutions, but locally-refined tetrahedra meshes. In both scenarios, magnetometer sensors were covering only the top half of the models.

A CG-FEM MEG forward modeling study in a human (and rabbit) head volume conductor model was performed by [44]. The authors distinguished 12 or more homogeneous and isotropic realistically shaped head tissue compartments and used 2 mm FEM models. Since the focus was on sensitivity analysis and suppression ratio (i.e., the magnetic field of radial dipole divided by the one of the corresponding tangential dipole, was found to be in average 0.19 ± 0.07 in the realistic human head model) and not on validation in sphere models like in our study, we can not further compare these results to our results.

Another example of a CG-FEM and Biot-Savart's law scheme used to compute the electric potential and the B-field was presented by [79]. Similar to our approach, the authors used a 1 mm hexahedral mesh of a 4-layer piecewise homogeneous and isotropic sphere model. Also the arrangement of sources and sensors was similar to our work. The main focus of their work was, however, on source modeling: it was found that from the different tested source modeling approaches, the subtraction approach, also used in our study at hand, was the most accurate one.

In [86], Chapter 2.10.4, for solving the MEG forward problem, three different CG-FEM source modeling approaches (i.e., subtraction, Venant's and partial integration) were compared in a 1 mm hexahedral (and in tetrahedral) meshes. Both the secondary and the full B-fields were compared to the analytical solution in a multi-layer homogeneous sphere model for tangentially oriented magnetometers. Also in this comparison it was found that the subtraction approach outperforms the other source modeling methods with regard to numerical accuracy for all sources apart from the most eccentric one. The subtraction method is therefore most sensitive to very close conductivity jumps and thus needs high resolution meshes especially in the source area, a result which is in line with ours. Deeper comparisons are again not easy because of different set-ups, but we are planning a direct comparison of the SimBio[2] code used by [86] and our *duneuro* implementation in future studies.

In [87], a guideline for EEG and MEG forward modeling using CG-FEM Venant's modeling was presented in realistic head models with a varying number of layers and conductivity profiles. The main result was that it is highly recommended to include the CSF and distinguish between gray and white matter and that, especially for the MEG, the modeling of skull spongiosa and compacta might be neglected. Furthermore, the numerical errors of a lower resolved (about 1 million nodes) 6 compartment anisotropic (6CA) model in reference to a higher resolved (about 2 millions nodes) version of 6CA were studied and expressed in terms of topography and magnitude errors: 95% of the sources had an RDM% of less than 2.5% and a MAG% of less than 10%.

In this chapter, we did not evaluate the computational costs of the CG-FEM schemes for the computation of the MEG forward solution.

---

[2] https://www.mrt.uni-jena.de/simbio/index.php/Main_Page

3. The Discontinuous Galerkin Finite Element Method for Solving the MEG Forward Problem

The discontinuous Galerkin finite element method (DG-FEM) originates from the idea of including boundary conditions in the weak formulation of a partial differential equation (PDE) via Nitsche's method [62], instead of restricting the test function space. The main idea of DG-FEM is an extension of this concept, namely, translating conservation properties into penalty terms in the weak formulation of a PDE. A DG-FEM forward modeling approach has recently been proposed for solving the EEG forward problem by [31].

The aim of this chapter is to derive and validate DG-FEM for solving the MEG forward problem. In order to prepare the DG-FEM derivation, we now recall some main properties of DG-FEM for the EEG.

First, we recall the volume triangulation $\mathcal{T}_h(\Omega)$ introduced in 2.1, which is a finite collection of disjoint and open subsets forming a partition of the domain Ω, where $h \in \mathbb{R}$ corresponds to the mesh-width. Furthermore, the triangulation induces the *internal skeleton*

$$\Gamma_{int} := \{\gamma_{e,f} = \partial E_e \cap E_f | E_e, E_f \in \mathcal{T}_h(\Omega), E_e \neq E_f, |\gamma_{e,f}| > 0\} \tag{3.1}$$

and the *skeleton* $\Gamma := \Gamma_{int} \cup \partial\Omega$. Let Y_h^r be the so-called *broken polynomial space*, that is defined as piecewise polynomial space on the partition $\mathcal{T}_h(\Omega)$:

$$Y_h^r := \{v \in L^2(\Omega) : v|_E \in P_r(E), \forall E \in \mathcal{T}_h(\Omega)\}, \tag{3.2}$$

where P_r denotes the space of polynomial functions of degree $r \in \mathbb{N}$. They describe functions that exhibit element-wise polynomial behavior but may be discontinuous across element interfaces.
In the following we assume that the conductivity tensor σ is constant on each element E_i and denote its value by σ_i.
Note the difference between the CG-FEM function space X_h^r defined in (2.2) and Y_h^r in (3.2). While in (2.2) functions are globally continuous and locally, i.e., on each element, polynomial, the space defined in (3.2) contains globally L^2 functions which are not globally continuous.
Furthermore, we recall the definition of the *jump* of a function $u \in Y_h^r$ on the intersection between two elements E_e and E_f of the triangulation $\mathcal{T}_h(\Omega)$ with outer normal $\mathbf{n}_e \in \mathbb{R}^3$ and $\mathbf{n}_f \in \mathbb{R}^3$, respectively:

$$[\![u]\!] := u|_{E_e}\mathbf{n}_e + u|_{E_f}\mathbf{n}_f \in \mathbb{R}^3.$$

Note that the normals $\mathbf{n}_e$ and $\mathbf{n}_f$ are opposing vectors, i.e. $\mathbf{n}_e = -\mathbf{n}_f$. In addition, the *weighted average* of u on the interface is defined as

$$\{u\} := \frac{\sigma_f}{\sigma_e + \sigma_f} u|_{E_e} + \frac{\sigma_e}{\sigma_e + \sigma_f} u|_{E_f}.$$

Finally, we recall the following property:

$$[\![uv]\!] = [\![u]\!]\{v\} + \{u\}[\![v]\!]. \tag{3.3}$$

For more details we refer, e.g., to [31].

3.1. Solving the EEG Forward Problem

In the DG-FEM context, the strategy to derive the weak form of the EEG forward problem is to first divide the whole domain Ω into elements of the triangulation $\mathcal{T}_h$, and then apply Gauss' theorem locally, on each element of the triangulation, where the discrete test and ansatz functions are polynomials (see (3.2)).

In [31], the *symmetric interior penalty Galerkin* (SIPG) DG discretization for (1.9)-(1.10) is obtained, and it reads: find $u_h \in Y_h^r$ such that

$$a_h(u_h, v_h) + J_h(u_h, v_h) = l_h(v_h), \;\; \forall v_h \in Y_h^r, \tag{3.4}$$

with

$$\begin{aligned} a_h(u_h, v_h) = &\int_\Omega \sigma \nabla_h u_h \cdot \nabla_h v_h \,\mathrm{d}x - \int_{\Gamma_{int}} \{\sigma \nabla_h u_h\} \cdot [\![v_h]\!] \,\mathrm{d}s \\ &- \int_{\Gamma_{int}} \{\sigma \nabla_h v_h\} \cdot [\![u_h]\!] \,\mathrm{d}s \,, \end{aligned}$$

$$J_h(u_h, v_h) = \eta \int_{\Gamma_{int}} \frac{\hat{\sigma}_\gamma}{h_\gamma} [\![u_h]\!] \cdot [\![v_h]\!] \,\mathrm{d}s \,,$$

and

$$l_h(v_h) = \int_\Omega f v_h \,\mathrm{d}s \,,$$

where η indicates the penalty parameter (which has to be chosen large enough to ensure coercivity), $\hat{\sigma}_\gamma$ and h_γ denote local definitions of the electric conductivity and the mesh width on an edge γ, respectively. In this particular case, $\hat{\sigma}_\gamma$ is chosen according to [29] and h_γ as the harmonic average of the conductivities of the adjacent elements [37]:

$$\hat{\sigma}_{\gamma_{e,f}} := \frac{min\,(|E_e|, |E_f|)}{|\gamma_{e,f}|},$$

and

$$h_{\gamma_{e,f}} := \frac{2\sigma_e \sigma_f}{\sigma_e + \sigma_f}.$$

The proposed discretization (3.4) is consistent and adjoint-consistent with the strong problem (1.9)-(1.10), and for a sufficiently large constant $\eta > 0$ it has a unique solution. Further details and proofs are in [31].

Remark 5. *In the DG discretization we make use of the so-called piecewise gradient, ∇_h, which is defined in the interior of each element K in the volume* *triangulation* $\mathcal{T}_h(\Omega)$. *It holds that*

$$\nabla_h v_h = \nabla(v_h|_K), \;\; \forall v_h \in Y_h^r. \tag{3.5}$$

In the following, when no ambiguity arises, we will use ∇, $a(\cdot,\cdot)$, $J(\cdot,\cdot)$, $l(\cdot)$, Γ_{int}, instead of ∇_h, $a_h(\cdot,\cdot)$, $J_h(\cdot,\cdot)$, $l_h(\cdot)$, Γ_{int}^h, respectively.

3.2. The Discrete Conservative Flux

As already seen, e.g., in (1.12), the MEG forward solution depends on the electric current density which is a quantity that is conservative in nature. In the continuum, the strong formulation of Poisson's equation, which we recall here:

$$\begin{aligned} \nabla \cdot (\sigma \nabla u) &= \nabla \cdot \mathbf{j}^p, && \text{in } \mathit{\Omega} \subseteq \mathbb{R}^3 \\ \sigma \nabla u \cdot \mathbf{n} &= 0, && \text{on } \partial \mathit{\Omega} \end{aligned}$$

leads to a conservation of charge property:

$$\int_{\partial K} (\sigma \nabla u) \cdot \mathbf{n} \, \mathrm{d}s = \int_K f \, \mathrm{d}x \,, \; \forall K \subset \Omega, \tag{3.6}$$

where $f = -\nabla \cdot \mathbf{j}^p$ and K is a control volume in Ω. We will refer to this conservation law by indicating the couple $(\sigma\nabla u, f)$, i.e., the boundary term and the volume term, respectively. We can point out that in the current setting, the current $\mathbf{j}$ is solenoidal, or diverge-free, hence it holds that

$$\int_{\partial K} \nabla \cdot (\mathbf{j}^s + \mathbf{j}^p) \, \mathrm{d}x = 0, \; \forall K \subset \Omega. \tag{3.7}$$

We have already mentioned in Section 1.2.2 that for FEMs the conservation of charge property carries over to the discrete solution only if the test space contains the characteristic function, which is one in K and zero everywhere else. In general, a conforming discretization, like CG-FEM, does not guarantee this property, while the DG-FEM fulfills a discrete analogue, as we see in the following.

In order to deduce the DG discrete conservation property, the strategy is to test the strong formulation with an *indicator* function χ_K which is defined as

$$\chi_k(\mathbf{x}) := \begin{cases} 1 & \text{if } \mathbf{x} \in K \\ 0 & \text{otherwise} \end{cases}$$

where K is a control volume in Ω, i.e., $K \in \mathcal{T}_h(\Omega)$. Note that $\chi_K \in Y_h^r$.
When we plug-in χ_k in (3.4), we have:

$$a_h(u_h, \chi_k) + J_h(u_h, \chi_k) = l_h(\chi_k),$$

which is equivalent to

$$\int_{\partial K} \left(\{\sigma \nabla u_h\} - \eta \frac{\hat{\sigma}_\gamma}{h_\gamma} [\![u_h]\!] \right) \cdot \mathbf{n}_K \, \mathrm{d}s = \int_K f \, \mathrm{d}x \, ,$$

exploiting the following facts:

1. $\nabla \chi_k$ denoted here $\nabla_h \chi_k = \nabla(\chi_k|_K) = 0$;

2. $[\![\chi_k]\!] = \chi_k|_K \mathbf{n}_K = \mathbf{n}_K$.

In the adopted notation, we can write that

$$\left(\{\sigma \nabla u_h\} - \eta \frac{\hat{\sigma}_\gamma}{h_\gamma} [\![u_h]\!], f \right)$$

is the general discrete DG conservation law for u_h.

3.3. The Subtraction Approach

When dealing with the subtraction approach already introduced in Section 2.3, two Poisson's equations have to be taken into account:

$$\nabla \cdot (\sigma^\infty \nabla u^\infty) = f, \ \text{ in } \mathbb{R}^3, \tag{3.8}$$

where u^{∞} is the solution in an unbounded domain and has an analytical expression, and

$$\begin{aligned} -\nabla \cdot (\sigma \nabla u^{corr}) &= \nabla \cdot (\sigma^{corr} \nabla u^{\infty}), && \text{in } \Omega \subseteq \mathbb{R}^3 \\ \sigma \nabla u^{corr} \cdot \mathbf{n} &= -\sigma \nabla u^{\infty} \cdot \mathbf{n}, && \text{on } \partial\Omega \end{aligned}$$

where u^{corr} is the new unknown. Within the subtraction approach, the conservation of charge for u^{corr} is $(\sigma \nabla u^{corr}, \nabla \cdot (\sigma^{corr} \nabla u^{\infty}))$, and the one for u^{∞} is $(\sigma^{\infty} \nabla u^{\infty}, f)$.

Remark 6. *We can observe that the sum of the conservation of charge for u^{corr} and the one for u^{∞} gives the general conservation property in* (3.6) *for u.*

There are equivalent ways to obtain the DG discretization of Poisson's equation when the subtraction approach is adopted. Here we start from the SIPG formulation in (3.4) and we plug-in the discrete splitting of u_h, i.e., $u_h = u_h^{corr} + u^{\infty}$:

$$\begin{aligned} & a(u_h^{corr} + u^{\infty}, v_h) + J(u_h^{corr} + u^{\infty}, v_h) = l(v_h) \\ \Leftrightarrow\ & a(u_h^{corr}, v_h) + J(u_h^{corr}, v_h) = -a(u^{\infty}, v_h) - J(u^{\infty}, v_h) + l(v_h). \end{aligned} \tag{3.9}$$

If we analyze each element separately we have:

$$\begin{aligned} a(u_h^{corr}, v_h) = & \int_{\Omega} \sigma \nabla u_h^{corr} \cdot \nabla v_h \, \mathrm{d}x - \int_{\Gamma_{int}} \{\sigma \nabla u_h^{corr}\} \cdot [\![v_h]\!] \, \mathrm{d}s \\ & - \int_{\Gamma_{int}} \{\sigma \nabla v_h\} \cdot [\![u_h^{corr}]\!] \, \mathrm{d}s \,, \end{aligned}$$

$$J(u_h^{corr}, v_h) = \eta \int_{\Gamma_{int}} \frac{\hat{\sigma}_{\gamma}}{h_{\gamma}} [\![u_h^{corr}]\!] \cdot [\![v_h]\!] \, \mathrm{d}s \,,$$

$$\begin{aligned} a(u^{\infty}, v_h) = & \int_{\Omega} \sigma \nabla u^{\infty} \cdot \nabla v_h \, \mathrm{d}x - \int_{\Gamma_{int}} \{\sigma \nabla u^{\infty}\} \cdot [\![v_h]\!] \, \mathrm{d}s \\ & - \int_{\Gamma_{int}} \{\sigma \nabla v_h\} \cdot [\![u^{\infty}]\!] \, \mathrm{d}s \,, \end{aligned}$$

$$J(u^{\infty}, v_h) = \eta \int_{\Gamma_{int}} \frac{\hat{\sigma}_{\gamma}}{h_{\gamma}} [\![u^{\infty}]\!] \cdot [\![v_h]\!] \, \mathrm{d}s \,.$$

First of all, we notice that $[\![u^{\infty}]\!] = 0$, as u^{∞} is continuous on the internal skeleton, assuming that the dipole $\mathbf{r}_0 \notin \Gamma_{int}$. Therefore the right-hand side of (3.9) becomes:

$$\tilde{l}(u^{\infty}, v_h) := \underbrace{- \int_{\Omega} \sigma \nabla u^{\infty} \cdot \nabla v_h \, \mathrm{d}x}_{(I)} + \int_{\Gamma_{int}} \{\sigma \nabla u^{\infty}\} \cdot [\![v_h]\!] \, \mathrm{d}s + \underbrace{\int_{\Omega} f v_h \, \mathrm{d}x}_{(II)} \,.$$

In order to manipulate (I), we split the conductivity σ between the infinity part σ^{∞} and the the correction part σ^{corr},

$$(I) = \int_{\Omega} \sigma^{\infty} \nabla u^{\infty} \cdot \nabla v_h \, \mathrm{d}x + \int_{\Omega} \sigma^{corr} \nabla u^{\infty} \cdot \nabla v_h \, \mathrm{d}x \,.$$

We present the following Lemma

Lemma 2. *(Element-wise integration by part formula)*
For $f, g \in Y_h^r$ it holds that

$$\int_{\Omega} \nabla f \cdot \nabla g \, \mathrm{d}x = - \int_{\Omega} \nabla \cdot \nabla f g \, \mathrm{d}x + \int_{\partial\Omega} \nabla f \cdot \boldsymbol{n} f \, \mathrm{d}s + \int_{\Gamma_{int}} [\![\nabla f]\!] \{g\} + \{\nabla f\} [\![g]\!] \, \mathrm{d}s \,.$$

Proof. For $f, g \in Y_h^r$ we can write that

$$\nabla \cdot (\nabla f g) = (\nabla \cdot \nabla f g) + \nabla f \cdot \nabla g. \tag{3.10}$$

If we consider the integral of (3.10) over the domain Ω we have:

$$\int_{\Omega} \nabla \cdot (\nabla f g) \, \mathrm{d}x = \int_{\Omega} (\nabla \cdot \nabla f g) \, \mathrm{d}x + \int_{\Omega} \nabla f \cdot \nabla g \, \mathrm{d}x \,. \tag{3.11}$$

It is not possible to apply Gauss' theorem to the first term of the right-hand side of (3.11) over the whole domain Ω, but it is when considering the integrand over an element E of the triangulation $\mathcal{T}_h(\Omega)$, were both f and g are polynomials, and it gives:

$$\int_\Omega (\nabla \cdot \nabla f g)\,\mathrm{d}x = \sum_{E \in \mathcal{T}_h(\Omega)} \int_E (\nabla \cdot \nabla f g)\,\mathrm{d}x$$
$$= \int_{\partial\Omega} \nabla f \cdot \mathbf{n} g \,\mathrm{d}s + \int_{\Gamma_{int}} [\![\nabla f g]\!]\,\mathrm{d}s\,. \tag{3.12}$$

After plugging-in the right-hand side of (3.12) in (3.11), using the multiplicative property in (3.3) and reordering the terms, the Lemma is proven. ☐

If we apply Lemma 2 with $f \coloneqq \sigma^\infty u^\infty$ and $g \coloneqq v_h$ we have that

$$(I) = \int_\Omega \nabla \cdot (\sigma^\infty \nabla u^\infty) v \,\mathrm{d}x + \int_{\partial\Omega} (\sigma^\infty \nabla u^\infty \mathbf{n})\, v_h \,\mathrm{d}s$$
$$+ \int_{\Gamma_{int}} \{\sigma^\infty \nabla u^\infty\} [\![v]\!]\,\mathrm{d}s + \int_\Omega \sigma^{corr} \nabla u^\infty \cdot \nabla v_h \,\mathrm{d}x\,.$$

Note that we used the fact that $\sigma^\infty \nabla u^\infty$ is continuous on the internal skeleton and thus $[\![\sigma^\infty \nabla u^\infty]\!] = 0$. Furthermore, it holds that

$$(II) = \int_\Omega \nabla \cdot (\sigma^\infty \nabla u^\infty) v_h \,\mathrm{d}x\,, \tag{3.13}$$

as f is the source term also for equation (3.8). Finally, we use again the splitting of the conductivity, i.e., $\sigma - \sigma^\infty = \sigma^{corr}$, and we have

$$\tilde{l}(u^\infty, v_h) = -\int_\Omega \sigma^{corr} \nabla u^\infty \nabla v \,\mathrm{d}x - \int_{\partial\Omega} \sigma^\infty \nabla u^\infty \mathbf{n} v \,\mathrm{d}s$$
$$+ \int_{\Gamma_{int}} \{\sigma^{corr} \nabla u^\infty\} [\![v]\!]\,\mathrm{d}s\,.$$

The DG discretization of the subtraction approach then reads: find $u_h^{corr} \in Y_h^r$ such that

$$a(u_h^{corr}, v_h) + J(u_h^{corr}, v_h) = \tilde{l}(u^\infty, v_h), \;\; \forall v_h \in Y_h^r. \tag{3.14}$$

In order to obtain the discrete conservation law for the subtraction approach, we plug-in $v_h = \chi_K$ in (3.14) and we get:

$$a(u_h^{corr}, \chi_K) + J(u_h^{corr}, \chi_K) = \tilde{l}(u^\infty, \chi_K), \tag{3.15}$$

where

$$
\begin{aligned}
a(u_h^{corr}, \chi_K) + J(u_h^{corr}, \chi_K) &= \\
&= \int_{\partial K} \left(\{\sigma \nabla u_h^{corr}\} - \eta \frac{\hat{\sigma}_\gamma}{h_\gamma} [\![u_h^{corr}]\!] \right) \mathbf{n}_K \, \mathrm{d}s \,,
\end{aligned}
$$

and

$$
\begin{aligned}
\tilde{l}(u^\infty, \chi_K) = &- \int_\Omega \sigma^{corr} \nabla u^\infty \cdot \nabla \chi_K \, \mathrm{d}x - \int_{\partial\Omega} \sigma^\infty \nabla u^\infty \cdot \mathbf{n} \chi_K \, \mathrm{d}s \\
&- \int_{\Gamma_{int}} \{\sigma^{corr} \nabla u^\infty\} \cdot [\![\chi_K]\!] \, \mathrm{d}s \,.
\end{aligned}
\tag{3.16}
$$

We rewrite the second term of (3.16) as

$$
- \int_{\partial K} [\![\sigma^\infty \nabla u^\infty]\!] \, \mathrm{d}s = 0,
$$

because the flux of u^∞ is continuous.
Finally, we can use the fact that $\nabla \chi_K = \delta_{\partial K} \cdot \mathbf{n}_k$ and Gauss' theorem and write

$$
\begin{aligned}
\tilde{l}(u^\infty, \chi_K) &= - \int_{\Gamma_{int} \bigcap \partial K} \{\sigma^{corr} \nabla u^\infty\} \mathbf{n}_K \, \mathrm{d}s \\
&= - \int_{\Gamma_{int} \bigcap \partial K} \sigma^{corr} \nabla u^\infty \mathbf{n}_K \, \mathrm{d}s \\
&= - \int_K \nabla \cdot (\sigma^{corr} \nabla u^\infty) \, \mathrm{d}x \,.
\end{aligned}
$$

The discrete DG conservation property for u_h^{corr} when the subtraction approach is used can then be indicated as

$$
\left(\{\sigma \nabla u_h^{corr}\} - \eta \frac{\hat{\sigma}_\gamma}{h_\gamma} [\![u_h^{corr}]\!], -\nabla \cdot (\sigma^{corr} \nabla u^\infty) \right) .
$$

At this point, we can also observe that it holds

$$
(\sigma \nabla u^\infty, f + \nabla \cdot (\sigma^{corr} \nabla u^\infty)) \,.
$$

3.4. The Partial Integration Approach

The general strong formulation and the conservation law do not change when the partial integration approach is adopted. In particular, it holds that $(\sigma\nabla u, f)$ is the couple describing the continuous conservation law.

As to the discrete formulation, the starting point is again equation (3.4). The partial integration approach is a so called direct approach, meaning that the unknown of the weak formulation is not modified and the right-hand side is treated directly exploiting, in this case, the definition of the Dirac delta distribution. Therefore the left-hand side of (3.4) does not change, but the right-hand side becomes:

$$\begin{aligned} l(v_h) &= \int_\Omega f v_h \, \mathrm{d}x \\ &= \int_\Omega \nabla \cdot (\mathbf{M}\delta_{\mathbf{y}}) v_h \, \mathrm{d}x \\ &= -\int_\Omega \mathbf{M} \cdot \nabla \delta_{\mathbf{y}} v_h \, \mathrm{d}x \\ &= -\mathbf{M} \cdot \nabla v_h(\mathbf{y}). \end{aligned} \tag{3.17}$$

Remark 7. *The test function $v_h \in Y_h^r$ is globally defined on Ω but the right-side of* (3.17) *is different from zero only on the element of $\mathcal{T}_h(\Omega)$ where the dipolar source lies, i.e., for that v_h such that $\boldsymbol{y} \in supp(v_h)$.*

In this context, the following Proposition holds:

Proposition 2. *When the partial integration approach is adopted, the discrete DG conservative flux, i.e., $\{\sigma\nabla u_h\} - \eta\frac{\hat{\sigma}_\gamma}{h_\gamma}[\![u_h]\!]$, is solenoidal.*

Proof. In order to deduce the discrete DG conservation law, we consider the SIPG with the right-hand side in (3.17), and we plug-in $v_h = \chi_K$. Again, the left-hand side does not change with respect to (3.4), and (3.17) becomes:

$$\begin{aligned} l_h(v_h) &= -\mathbf{M} \cdot \nabla \chi_K(\mathbf{y}) \\ &= 0, \end{aligned}$$

meaning that the DG numerical flux is solenoidal when the partial integration approach is adopted. $\square$

We can write that

$$\left(\{\sigma\nabla u_h\} - \eta\frac{\hat{\sigma}_\gamma}{h_\gamma}[\![u_h]\!], 0\right)$$

is the discrete DG conservation law for u_h when the partial integration approach is adopted, which reflects the solenoidal property of the full flux (see (3.7)). The effect of Proposition 2 on the numerical computation of the B-field are examined in the following.

3.5. Solving the MEG Forward Problem

In this section we describe the DG discrete representation of the MEG forward problem in an analogous way as for the CG-FEM, in Section 2.6. Following (2.18), we can consider the analogous formula for the electric flux in the DG-FEM scheme, i.e.,

$$\sigma\nabla u_h = \sigma\sum_i u_i\nabla\varphi_i, \tag{3.18}$$

where $(\varphi_i)_i$ is a basis of Y_h^r. As already mentioned, in general this discrete formulation of the flux does not verify the conservation of charge property. Conversely and despite the CG-FEM case, in the DG-FEM approach we can consider another expression of the discrete electric flux, i.e.,

$$\mathbf{j}_h^{DG} = \{\sigma\nabla u_h\} - \eta\frac{\hat{\sigma}_\gamma}{h_\gamma}[\![u_h]\!] \tag{3.19}$$

that verifies the conservation of charge law, as described in Section 3.2. The main idea is to embed this *conservative current* (or *conservative flux*, i.e., flux fulfilling the property of conservation of charge) in the computation of $\mathbf{B}^s$.
We have to notice that $\mathbf{j}_h^{DG}$ is defined only on the internal skeleton Γ_{int} (3.1) and not in the entire volume Ω. In order to integrate $\mathbf{j}_h^{DG}$ when computing $\mathbf{B}^s$ (1.13), we thus need to extend the current into the volume. One way to do so is to interpolate $\mathbf{j}_h^{DG}$ in the space of the lowest-order Raviart Thomas function

(RT_0). RT_0 is $H(div)$- conforming and its degrees of freedom (DOFs) are the evaluations of the basis functions along the projections normal to the faces of each element, exactly where $\mathbf{j}_h^{DG}$ is defined. The space $H(div;\Omega)$ is defined as:

$$H(div;\Omega) \coloneqq \{\mathbf{v} \in L^2(\Omega)^3 : \nabla\cdot\mathbf{v} \in L^2(\Omega)\}, \tag{3.20}$$

and RT_0 as [33, 61]:

$$RT_0(\mathcal{T}_h(\Omega)) \coloneqq \{\mathbf{v} \in H(div;\Omega) : (\nabla\cdot\mathbf{v}\,)|_E \in P_0(E), \forall E \in \mathcal{T}_h(\Omega)\}. \tag{3.21}$$

As we considered hexahedral elements (see Appendix A.1), we have $P_0 = \mathbb{Q}_0$ in (3.21). For a regular, hexahedral mesh with edge length h, as in our case, a RT_0 basis function $\boldsymbol{\psi}_k$ has as support the two hexahedral elements $E_e, E_f \in \mathcal{T}_h(\Omega)$ sharing the face $f_k = E_e \cap E_f$ with normal vector $\mathbf{n}_k$ and centroid $\bar{\mathbf{x}}_k$. It can be defined by

$$\boldsymbol{\psi}_k(\mathbf{x}) = \begin{cases} \left(1 + \frac{(\mathbf{x}-\bar{\mathbf{x}}_k)\cdot\mathbf{n}_k}{h}\right)\mathbf{n}_k & \text{if } \mathbf{x} \in \bar{E}_e \cap \bar{E}_f \\ 0 & \text{otherwise.} \end{cases}$$

For more insights see [33] and [61], and Figure 3.1, where the basis function $\boldsymbol{\psi}_k$ has been visualized. For the discretization of $\mathbf{B}^s$ we start from observing that the conservative flux $\boldsymbol{\Psi}(u_h)$ is a function of $(\mathcal{C}^0)^3$ on Γ_{int} which depends on the potential u_h:

$$\boldsymbol{\Psi}(u_h) = \mathbf{j}_h^{DG} = \{\sigma\nabla u_h\} - \eta\frac{\hat{\sigma}_\gamma}{h_\gamma}[\![u_h]\!].$$

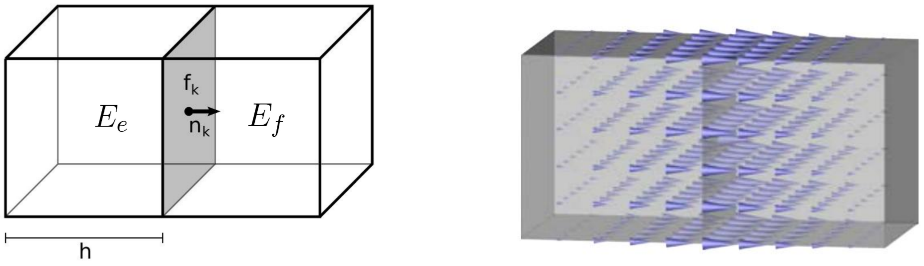

Figure 3.1.: Visualization of a zeroth-order Raviart-Thomas basis function (on the right) and its support (on the left). The support is made of two hexahedral elements E_e and E_f, which are sharing the face f_k with unit outer normal $\mathbf{n}_k$. The vector valued function is equal to $1\cdot\mathbf{n}_k$ on the face f_k and it decays when reaching the other parallel faces.

If $(\varphi_i)_i$ is a basis of Y_h^1, then the correction potential can be written as

$$u_h = \sum_i u_i \varphi_i,$$

and, due to linearity, we have

$$\mathbf{\Psi}(u_h) = \sum_i u_i \mathbf{\Psi}(\varphi_i).$$

If we now apply the extension operator $\mathcal{E}_{RT0}$ into RT_0 to $\mathbf{\Psi}(u_h)$ and we exploit again linearity, we obtain:

$$\mathcal{E}_{RT0}(\mathbf{\Psi}(u_h)) = \sum_i u_i \mathcal{E}_{RT0}\left(\mathbf{\Psi}(\varphi_i)\right) \in L^2(\Omega).$$

Finally, $\mathbf{B}^s$ can be then approximated as follows:

$$\mathbf{B}^s(\mathbf{r}) \simeq -\frac{\mu_0}{4\pi} \sum_i u_i \int_\Omega \mathcal{E}_{RT0}(\mathbf{\Psi}(\varphi_i))(\mathbf{r}') \times \frac{\mathbf{r}-\mathbf{r}'}{|\mathbf{r}-\mathbf{r}'|^3}\, d^3\mathbf{r}'.$$

If we call $\mathbf{c}_n$ the center of the n^{th} coil, then the discretization of $\mathbf{B}^s$ evaluated in $\mathbf{c}_n$ reads,

$$\mathbf{B}^s(\mathbf{c}_n) \simeq \sum_i u_i \underbrace{\left(-\frac{\mu_0}{4\pi}\right) \int_\Omega \mathcal{E}_{RT0}(\mathbf{\Psi}(\varphi_i))(\mathbf{r}') \times \frac{\mathbf{c}_n-\mathbf{r}'}{|\mathbf{c}_n-\mathbf{r}'|^3}\, d^3\mathbf{r}'}_{:=S_{ni}^{DG}}. \tag{3.22}$$

$S^{DG} = \left(S_{ni}^{DG}\right)_{n,i}$ is the secondary magnetic field integration matrix related to the DG-FEM scheme. Equation (3.22) can be rewritten into a matrix equation,

$$\mathbf{B}_h^s = S^{DG}\mathbf{u}, \tag{3.23}$$

where $\mathbf{B}_h^s$ represents the discretization of $\mathbf{B}^s$.

Remark 8. *The extension to the volumetric element of the i^{th} basis function of the space Y_h^1 can be described as:*

$$\mathcal{E}_{RT_0}(\mathbf{\Psi}(\varphi_i)) = \sum_k \alpha_i^k \boldsymbol{\psi}_k, \tag{3.24}$$

where $(\boldsymbol{\psi}_k)_k$ *form a basis of* RT_0 *and* α_i^k *are the DOFs, which can be derived as*

$$\alpha_i^k = \boldsymbol{\Psi}(\varphi_i(\bar{\boldsymbol{x}}_k)) \cdot \boldsymbol{n}_k, \tag{3.25}$$

with $\bar{\boldsymbol{x}}_k$ *and* $\boldsymbol{n}_k$ *the centroid and the external normal of the face* f_k*, respectively (see Figure 3.1).*

In the particular case of the subtraction approach, the procedure described above only applies for $\mathbf{B}^s_{corr,h}$, with the flux

$$\mathbf{j}_h^{DG} = \mathbf{j}_h^{corr,DG} = \{\sigma \nabla u_h^{corr}\} - \eta \frac{\hat{\sigma}_\gamma}{h_\gamma} [\![u_h^{corr}]\!]. \tag{3.26}$$

The infinity contribution has to be added in a subsequent moment. In the classical subtraction approach $\mathbf{B}^s_{\infty,h} = \mathbf{B}^s_{\infty,h}(u_h^\infty)$, where u_h^∞ is interpolated in Y_h^r, is summed to $\mathbf{B}^s_{corr,h}$. Alternatively, the analytical formula of ∇u^∞ can be directly used.

In the case of the partial integration approach, the procedure described above applies for the full B field $\mathbf{B}_h$, as a direct consequence of Proposition 2, i.e., since the DG conservative flux is solenoidal when the partial integration approach is adopted.

Finally, as described in the following, MEG forward computations are carried out for a large number of dipole sources. In order to speed up the many numerically expensive computations of the secondary B-field $\mathbf{B}^s$ for all of these sources, following [95], we adapted and implemented transfer matrix approaches for the two presented DG-FEM-based MEG forward modeling schemes (conservative and non-conservative). Details can be found in Appendix A.4.

3.6. Validation in Sphere Models

In this section we describe the methods and the input data we used to validate the new DG-FEMs described in the previous sections of this chapter. First of all, we implemented the two new DG-FEM approaches, namely, DG-FEMs with a non-conservative and a conservative representation of the electric flux in *duneuro*, see

Appendix A.5 [64]. The input data we used for our simulations are the same as the ones used in the CG-FEM validation, in Chapter 2. More specifically, the volume conductor models with which we tested our new DG-FEM implementations are 4-layer homogeneous sphere models represented via hexahedral meshes with three different resolutions, namely 4 mm, 2 mm and 1 mm. Details on the models and meshes are in Tables A.1 and A.2, respectively. We considered 10,000 tangentially oriented dipoles, distributed in 10 logarithmically scaled eccentricities (see Table A.3), and we evaluated the secondary and the full B-field in 256 point-magnetometers outside the sphere model at a fixed radius of 110 mm (see Figure A.1). The errors were assessed via the $RDM\%$ and $MAG\%$, defined in (A.1) and (A.2), respectively. More details about the input data and error measures can be found in Appendix A. Statistical results of numerical accuracies are visualized with mean curves, boxplots and cumulative relative frequency curves.

Study 1: DG-FEM and Conservative versus Non-Conservative Flux

In this analysis the focus is on DG-FEM and the necessity of embedding the conservative flux (3.19) in the evaluation of the secondary B-field $\mathbf{B}^s$. We thus validated and compared the DG-FEM MEG forward methods with non-conservative (3.18) and conservative (3.19) flux. As a general remark, we recall that we consider only tangentially-oriented sources for the validations and evaluations in the next sections, because, as seen in Section 2.7, radial sources do not produce any magnetic field outside spherical volume conductor models. Following formulas (1.13) and (1.12), we measured errors of the vector fields $\mathbf{B}^s$ and $\mathbf{B}$. These errors thus include parts from the radial and the two tangential sensor orientations and thus enable an overall view on the MEG forward modeling accuracy. On the one hand, radially-oriented sensor orientations are dominant in realistic MEG sensor configurations (see Figure 3.15), while on the other hand, and as seen in Section 2.7, because of the cancellation effect of primary and secondary B-fields, tangentially-oriented sensor orientations are especially delicate numerical test-cases.

The RDM% and MAG% statistical errors can be seen in Figure 3.2. Note that only a 4 mm mesh (*seg_4_res_4*) has been used, because the lower the resolution, the higher we expect the difference to be. With increasing source eccentricity, an overall increase of the RDM% (top row) and MAG% (bottom row) errors can be observed as shown by the mean error (left column) and by the boxplot statistics (right column). The boxplots indicate mainly increasing error statistics with regard to median, total range (TR), interquartile range (IQR) and also maxima for both conservative and non-conservative flux implementations.

As a general result, the employment of the conservative flux (in green) delivers better results than the one of the non-conservative flux (in dark red). The difference between the two implementations is more evident with increasing eccentricity of the sources.

Let us now discuss in more detail the eccentricity of 0.9796, i.e., 1.59 mm from the brain-CSF boundary. For the eccentricity of 0.9796, the maximum difference of 20 pp in mean RDM% is achieved between the conservative and the non-conservative DG flux approaches. For the least eccentric sources, this difference goes down to about 2 pp (see the 0.01 eccentricity in top left subfigure of Figure 3.2). With regard to the boxplot of the RDM%, the median values of the conservative flux case are overall smaller than the ones of the non-conservative flux. For sources with eccentricity value of 0.9796 the RDM% median difference is greater than 20 pp; the IQR difference is approximately 15 pp and the TR is constant and similar for both approaches. In the MAG% boxplot (right column), the much better performance of the conservative flux approach is especially clearly visible. The MAG% median difference reaches 40 pp for realistic sources of eccentricity 0.9796. For the same sources, the TRs, IQRs and means are in general large, with a ratio 1:4 between conservative and non-conservative flux values. For lower eccentricities, we observe overall smaller errors.

Study 2: DG-FEM and the Subtraction Approach

Since we have seen in the last study that the conservative flux DG-FEM approach (3.19) performs remarkably better than the non-conservative approach (3.18), for the remainder of this work, we proceed with DG-FEM as in (3.22). The second study proposed is about the convergence of the DG-FEM for computing

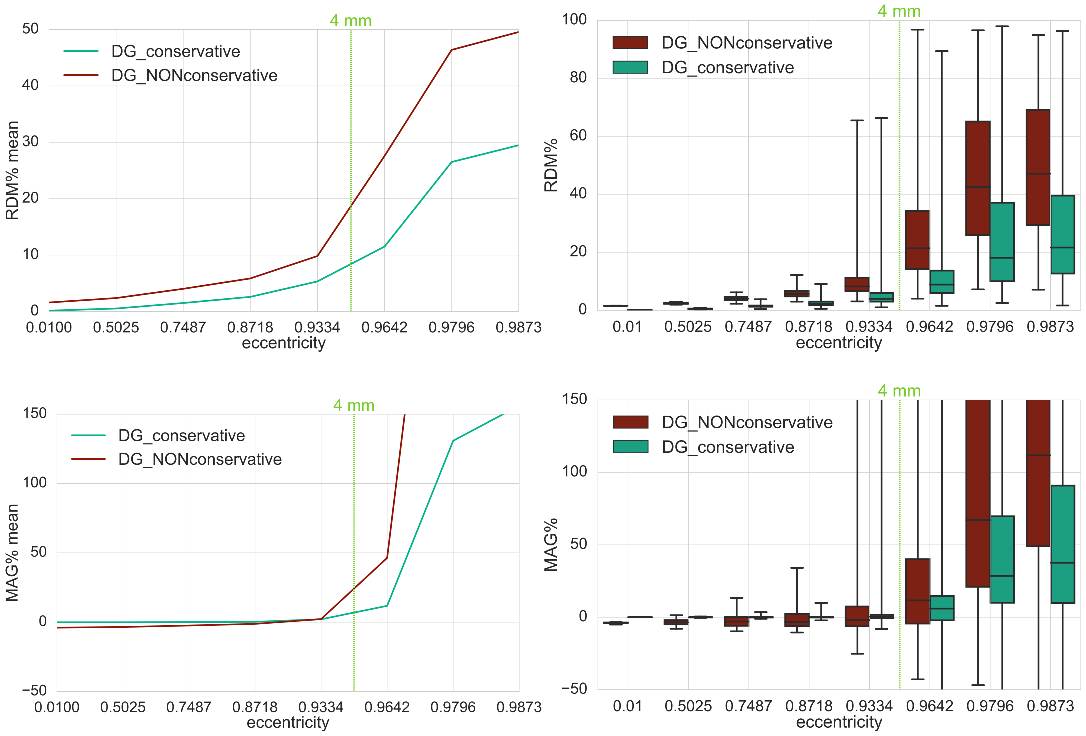

Figure 3.2.: Accuracy comparison for secondary B-field $\mathbf{B}^s$ computation (1.13) between DG-FEM with non-conservative flux ((3.18), red) and DG-FEM with the conservative flux ((3.19), in green) in a 4 mm hexahedral sphere model: visualized are the means (left column) and the boxplots (right column) of the RDM% (top row) and MAG% (bottom row), for tangentially oriented sources at logarithmically-scaled eccentricities. The dashed green line represents the eccentricity of 4 mm distance to the brain-CSF boundary. Note the different scaling of the y-axes (top row).

the secondary B-field $\mathbf{B}^s$ when the mesh resolution is increased, namely from the coarsest resolution of 4 mm over 2 mm to the highest resolution of 1 mm. We studied the behavior of the RDM% and MAG% errors for 10,000 tangentially oriented and randomly distributed dipoles at 10 different eccentricities. More details can be found in Appendix A. Results can be seen in Figure 3.3. The RDM% and MAG% mean error curves (Figure 3.3, left column) are overall increasing with increasing source eccentricity, as hypothesized by the theory of the subtraction approach [96] and well-known already from EEG results [30]. Most importantly, for increasing mesh resolution, error statistics improve considerably. For the most relevant eccentricity of 0.9796, the highest resolved model ($seg\_1\_res\_1$) reaches mean RDM% and MAG% errors of 1.5% and 0.1%, respectively. On the right column, we can study the boxplots of the RDM% and MAG% of the same scenario analyzed before. Both in the RDM% and MAG% cases, there is an overall increase of the median, TR and IQR when increasing the source eccentricity and decreasing the mesh resolution. If we focus on the 1 mm mesh and 0.9796 eccentricity, the RDM% median is only around 1.2%; the IQR is 0.8% and the TR reaches 20%. In particular, the IQR for dipoles of eccentricity 0.9796 increases drastically from 0.8% (1 mm) to almost 10% (2 mm) and 30% (4 mm). The TR behaves similarly. The median MAG% is extremely low, i.e., ≈ 0.017%; the IQR is ≈ 0.8% and the TR is ≈ 25%. For this eccentricity, we notice a large difference among the three mesh resolutions: the medians grow from 0.017% (1 mm), to 2.8% (2 mm), up to 28.6% (4 mm). The same trend is noticeable for the IQR: 0.8% (1 mm), 7% (2 mm) and 60% (4 mm). However, these values are out of the displayed graph range. The TR again behaves similarly.

In Figure 3.4, we can analyze how the secondary B-field errors propagate to the full B-field solutions. As a general remark, we notice that dipoles with a very low eccentricity, i.e., 0.01, are in fact radially oriented dipoles, as they are very close to the center of the sphere. For those dipoles, there is a cancellation between primary and secondary B-field, resulting in a null full B-field. Therefore, when computing the MAG% error for those dipoles, the denominator is zero in (A.2), leading to a strong increase of MAG% values, which is clearly visible in Figure 3.4. With regard to the main behavior of the errors, we observe the same trends as the secondary B-field study in Figure 3.3. In particular, for the most relevant eccentricity, i.e., 0.9796, and 1 mm resolution, the mean RDM% and MAG% reach 1.75% and 0.12%, respectively, and the median RDM% and MAG% are 1.6% and 0.3%, respectively.

Study 3: DG-FEM and the Partial Integration Approach

In this section we analyze convergence results of the DG-FEM simulations in the three spherical meshes of Table A.2 when the partial integration approach is adopted. RDM% and MAG% error measures are visualized in Figure 3.5 and 3.6 for the secondary and full B-field, respectively.

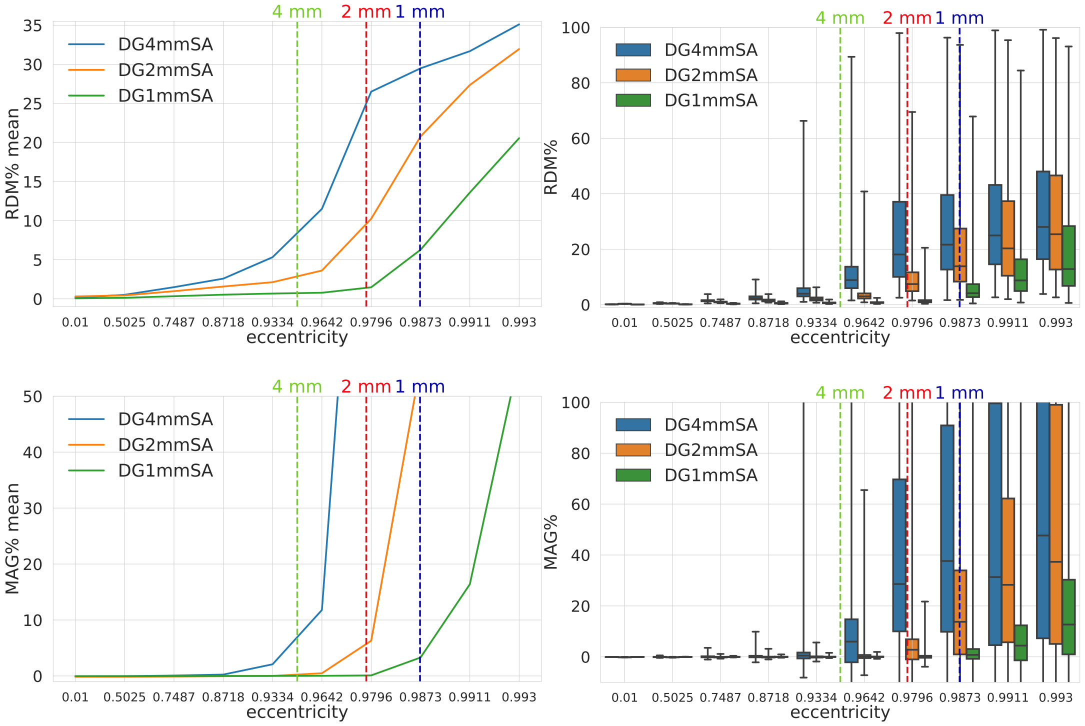

Figure 3.3.: Validation and convergence analysis for secondary B-field $\mathbf{B}^s$ computation (1.13) of DG-FEM when the *subtraction approach* is used in a 4 mm (blue), 2 mm (yellow) and 1 mm (green) hexahedral sphere model: visualized are the means (left column) and the boxplots (right column) of the RDM% (top row) and MAG% (bottom row), for tangentially oriented sources at logarithmically-scaled eccentricities. Dashed lines represent the eccentricities of 4 mm (green), 2 mm (red) and 1 mm (blue) distances to the brain-CSF boundary. Note the different scaling of the y-axes.

First of all, we notice the convergence of the method for the partial integration: when the resolution of the mesh is increasing the errors decrease. Second, the overall error values increase for higher eccentricities. Third, all the values are increasing when the dipoles belong to the layer of elements of the brain-CSF boundary, namely, after the boundary-eccentricity of 0.9334 for the 4 mm resolution mesh, 0.9642 for the 2 mm resolution mesh and 0.9796 for the 1 mm resolution mesh. The RDM% mean (Figure 3.5, left column) for the most relevant eccentricity of 0.9796, and the most accurate mesh (1 mm) is ≈ 1.3% and there is a big difference when comparing the topographical performances of the different mesh resolution for the same eccentricity: from ≈ 11% (4 mm), over 4% (2 mm) to 1.3% (1 mm).

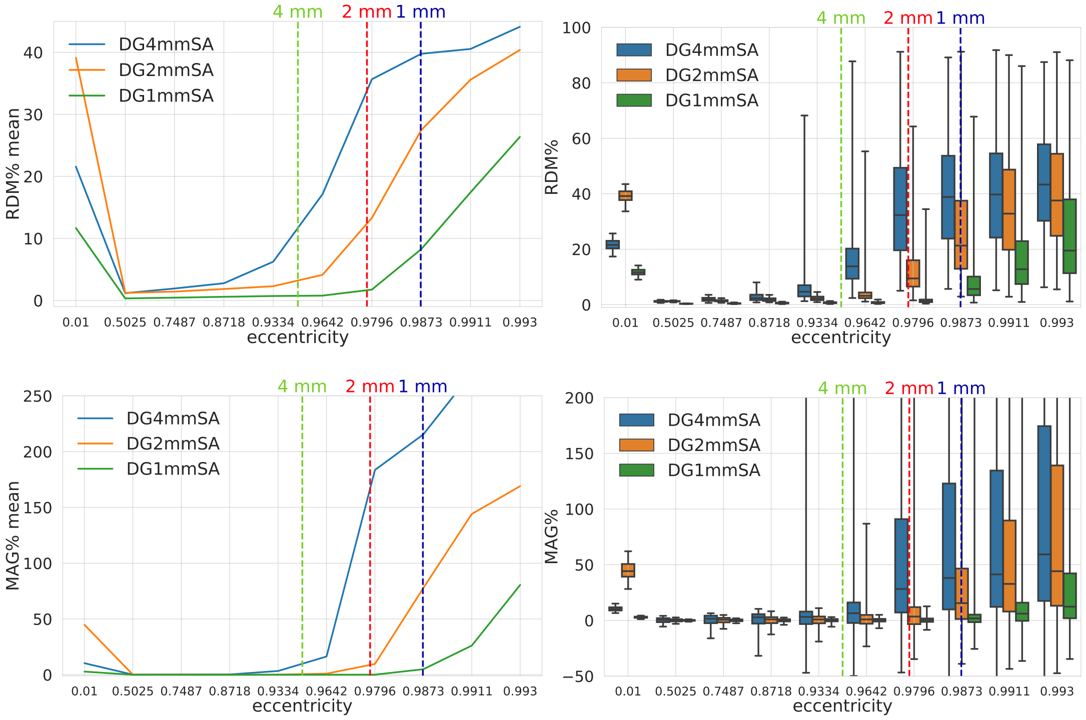

Figure 3.4.: Validation and convergence analysis for solving the MEG forward problem, i.e., the full B-field **B** (1.12), of DG-FEM when the *subtraction approach* is used in a 4 mm (blue), 2 mm (yellow) and 1 mm (green) hexahedral sphere model: visualized are the means (left column) and the boxplots (right column) of the RDM% (top row) and MAG% (bottom row), for tangentially oriented sources at logarithmically-scaled eccentricities. Dashed lines represent the eccentricities of 4 mm (green), 2 mm (red) and 1 mm (blue) distances to the brain-CSF boundary. Note the different scaling of the y-axes.

With regard to MAG% means, we can observe that in general the values are very low and they do not exceed ≈ 5.7% independently of the eccentricity and the mesh resolution. For the most relevant eccentricity of 0.9796, and the most accurate mesh (1 mm) the mean MAG% is 0.04%. When analyzing the RDM% boxplot in Figure 3.5, right column, for the most relevant eccentricity of 0.979, we observe an increase in medians, IQRs and TRs when the resolution of the mesh decreases. In particular, RDM% medians go from 10%, over 3.7% to 1.15% for 4 mm, 2 mm and 1 mm resolution meshes respectively. IQRs decrease from 6% over 2.5% until 0.5% for 4 mm, 2 mm and 1 mm resolution meshes. The TRs behave similarly. With regard to the MAG% boxplots for the most relevant eccentricity, the medians are always very low: 0.6%, -0.3% and -0.0004% for 4 mm, 2 mm and 1 mm resolution meshes, respectively. IQRs behave similarly and some outliers are present, the TR is indeed quite large for 4 mm resolution, i.e., ≈ 40%, and it decreases to 10% for 2 mm and to 5% for 1 mm resolution meshes.

If we consider the most eccentric dipoles, RDM% and MAG% values do not explode. More specifically, RDM% and MAG% means are 16% and 5.7% (4 mm), 8% and 1.5% (2 mm), 3% and 0.04 (1 mm).

The performances of the partial integration approach are in general very high.

In Figure 3.6, we can analyze how the secondary B-field errors propagate to the

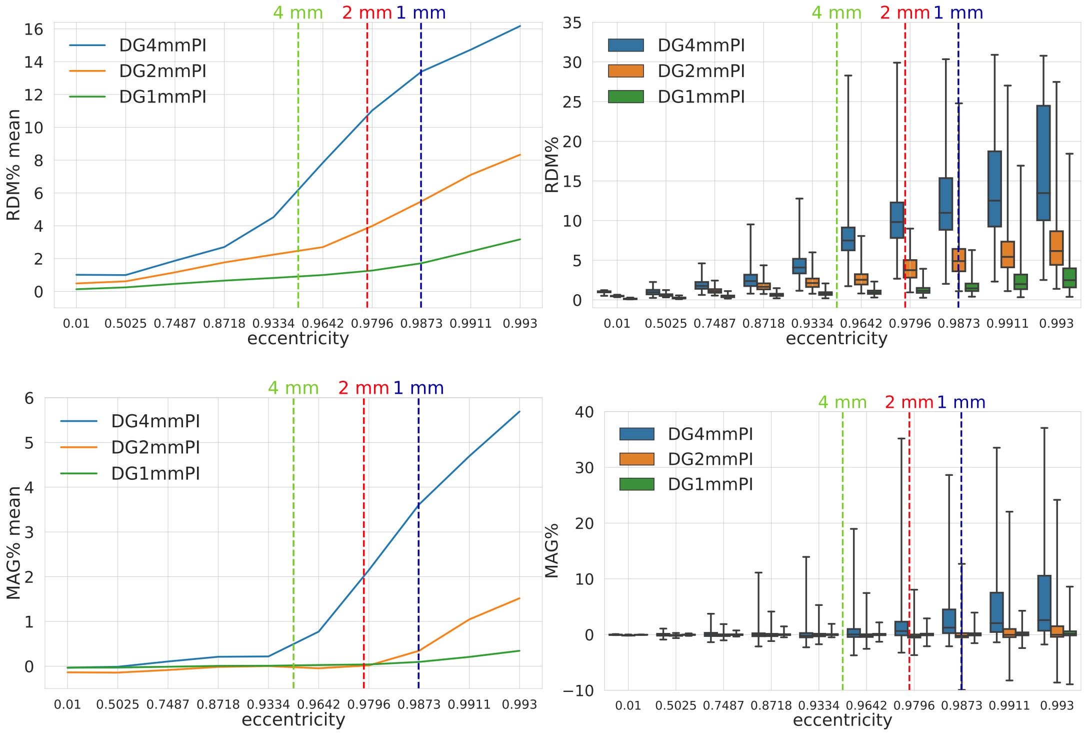

Figure 3.5.: Validation and convergence analysis for secondary B-field $\mathbf{B}^s$ computation (1.13) of DG-FEM when the *partial integration* approach is used in a 4 mm (blue), 2 mm (yellow) and 1 mm (green) hexahedral sphere model: visualized are the means (left column) and the boxplots (right column) of the RDM% (top row) and MAG% (bottom row), for tangentially oriented sources at logarithmically-scaled eccentricities. Dashed lines represent the eccentricities of 4 mm (green), 2 mm (red) and 1 mm (blue) distances to the brain-CSF boundary. Note the different scaling of the y-axes.

full B-field solutions. Even in this case, there are high errors for low eccentricities, clearly visible in Figure 3.6. With regard to the main behavior of the errors, we observe the same trends as in the secondary B-field study in Figure 3.5. In particular, for the most relevant eccentricity, i.e., 0.9796, and 1 mm resolution, the mean RDM% and MAG% reach 1.2% and 0.23%, respectively. For lower mesh resolutions the RDM% mean values are 3% and 7% and MAG% mean values are -9% and -28%, for 2 and 4 mm resolution meshes, respectively. RDM% and MAG% medians are very close to RDM% and MAG% means.

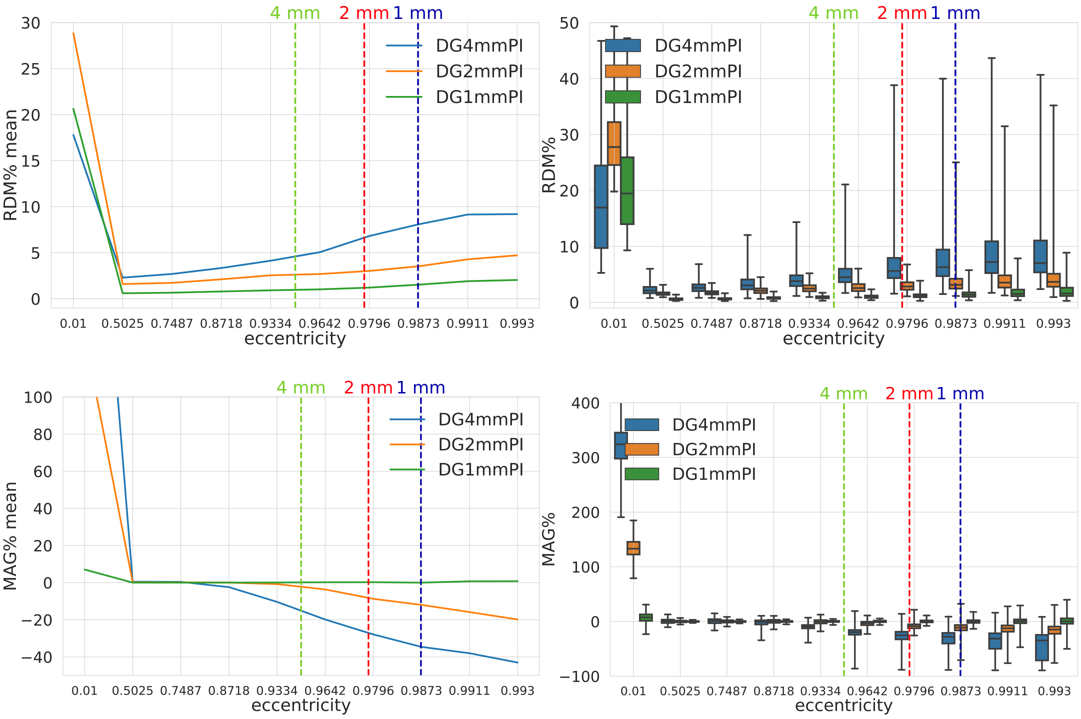

Figure 3.6.: Validation and convergence analysis for solving the MEG forward problem, i.e., the full B-field $\mathbf{B}$ (1.12), of DG-FEM when the *partial integration* approach is used in a 4 mm (blue), 2 mm (yellow) and 1 mm (green) hexahedral sphere model: visualized are the means (left column) and the boxplots (right column) of the RDM% (top row) and MAG% (bottom row), for tangentially oriented sources at logarithmically-scaled eccentricities. Dashed lines represent the eccentricities of 4 mm (green), 2 mm (red) and 1 mm (blue) distances to the brain-CSF boundary. Note the different scaling of the y-axes.

Study 4: DG-FEM Comparison between Different Source Models

Similarly to what has been presented for the CG-FEM in Chapter 2, in the following we compare the accuracy of the two approaches we described to discretize the right-hand side of the Poisson equation, namely the subtraction approach (SA) and the partial integration approach (PI), for each mesh resolution, namely 4 mm, 2 mm and 1 mm, see Table A.2.

We computed and visualized RDM% and MAG% for both the secondary and full B-field for 10,000 tangentially oriented dipoles at 10 logarithmically-scaled eccentricities. See Appendix A for more details.

In Figure 3.7, secondary B-field error measure results corresponding to the 4 mm resolution mesh are reported. As a general remark about RDM% values, SA performs slightly better than PI until the eccentricity of 0.9334, i.e., the eccentricity which corresponds to brain-CSF boundary layer of 4 mm hexahedral elements. This difference is ≈ 1 pp in the mean RDM%. For higher eccentricities, SA RDM% values are higher than the one of PI, reaching up to 20 pp in terms of mean RDM%.

Note that for eccentricities higher than 0.9334, both approaches lead to RDM% mean values above 5%, therefore the accuracy of the method is low independently of the approach used for the discretization of the right-hand side.

With regard to the MAG% values, the general behavior is the following. For eccentricities smaller than 0.9334, both SA and PI deliver MAG% values whose differences are negligible, while for eccentricities higher than 0.9334 PI performs better than SA, reaching differences up to 300 pp in terms of mean MAG%. The main increase of RDM% and MAG% occurs when dipoles approach the boundary layer of hexahedron between brain and CSF compartments, i.e., dipoles with eccentricities higher than 0.9334.

For eccentricities lower than the boundary eccentricity, the mean RDM% and MAG% differences are negligible. Therefore we can state that for such a coarse mesh, when the most significant eccentricity is the one of 0.9334, the methods are delivering almost identical results. The behavior of PI for low eccentric dipoles is even more visible for the full B-field results in Figure 3.8, where mean MAG% and median exceed 300%. Again SA is not delivering accurate results for very high eccentricities, but also PI has high errors for such a coarsely resolved mesh. In general, a 4 mm resolution sphere model is too coarse to have accurate results. This is valid for every discretization approach considered in this study.

In the next comparison we fixed the mesh resolution at 2 mm and we compare RDM% and MAG% for both SA and PI. Results for both the secondary and the full B-field are visualized in Figure 3.9 and 3.10, respectively.

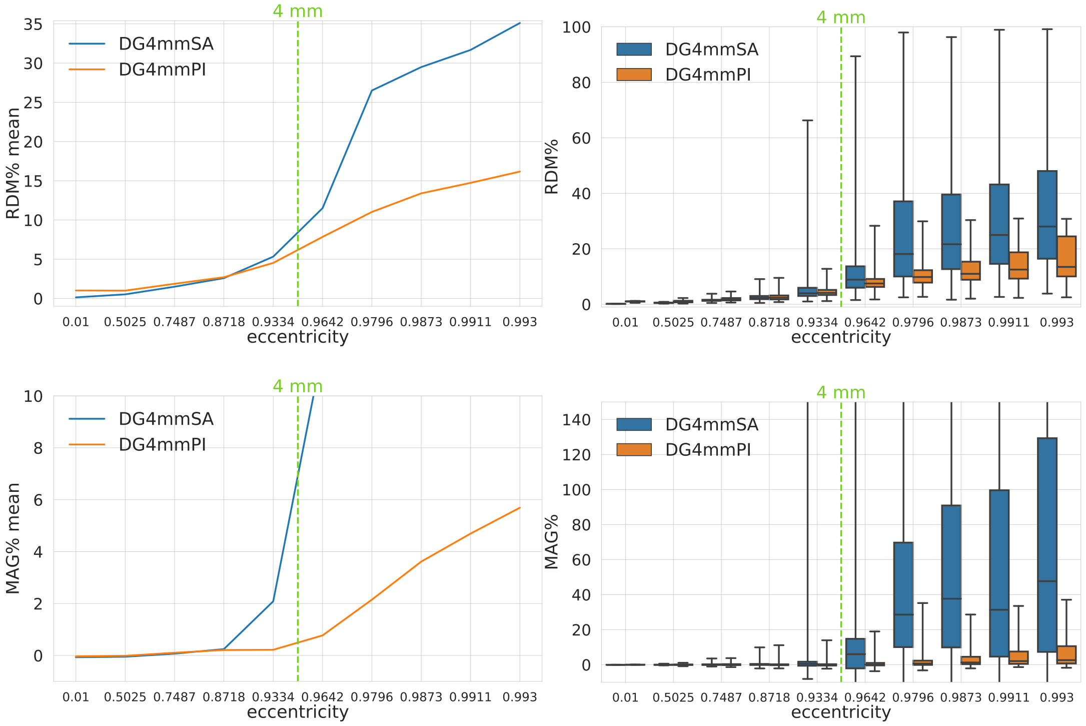

Figure 3.7.: Accuracy comparison of the secondary B-field $\mathbf{B}^s$ computation (1.13) of DG-FEM when the subtraction (blue) and the partial integration (yellow) approaches are used in a 4 mm hexahedral sphere model: visualized are the means (left column) and the boxplots (right column) of the RDM% (top row) and MAG% (bottom row), for tangentially oriented sources at logarithmically-scaled eccentricities. The green dashed line represents the eccentricity of 4 mm distance to the brain-CSF boundary. Note the different scaling of the y-axes.

The same general considerations described for the 4 mm case hold also for this scenario. In particular, the SA RDM% values are slightly better for eccentricities lower than the boundary eccentricity, i.e., 0.9796 in this case. At the same eccentricity, the mean RDM% difference is around 6 pp, where PI outperforms SA, and for higher eccentricities this difference reaches up to 23 pp.

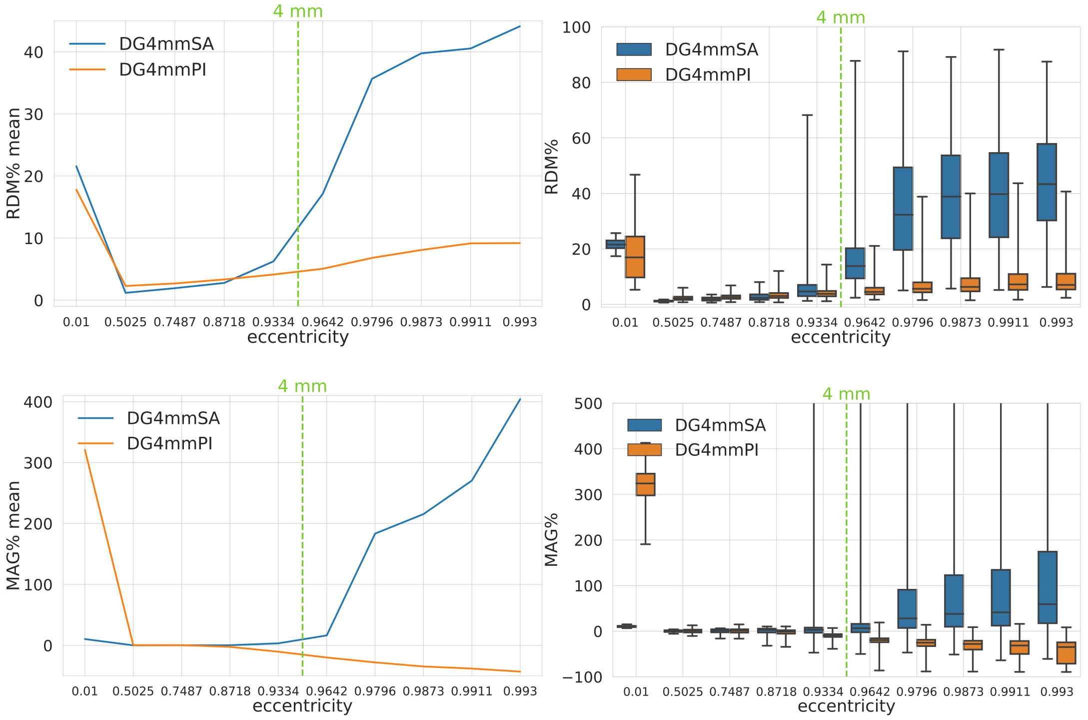

Figure 3.8.: Accuracy comparison for solving the MEG forward problem, i.e., the full B-field **B** (1.12) of DG-FEM when the subtraction (blue) and the partial integration (yellow) approaches are used in a 4 mm hexahedral sphere model: visualized are the means (left column) and the boxplots (right column) of the RDM% (top row) and MAG% (bottom row), for tangentially oriented sources at logarithmically-scaled eccentricities. The green dashed line represents the eccentricity of 4 mm distance to the brain-CSF boundary. Note the different scaling of the y-axes.

The same trend can be seen for MAG% mean values: at the most relevant eccentricity the difference is around 6 pp and goes up to 115 pp.
Furthermore, from the boxplots in Figure 3.9 (right column), when considering the most relevant eccentricity, we observe a RDM% median and IQR difference of ≈ 5 pp and a TRs difference of up to 60 pp, revealing the high performance of PI over SA. With regard to MAG% values, the median difference between PI and SA is around 3 pp, the IQR difference exceeds 7 pp and the TR difference reaches more than 500 pp.

With regard to the comparison of the full B-field visualized in Figure 3.10, we again observe the numerical instability for RDM% and MAG% measures when almost radial dipoles are considered. Furthermore, the same trend as the

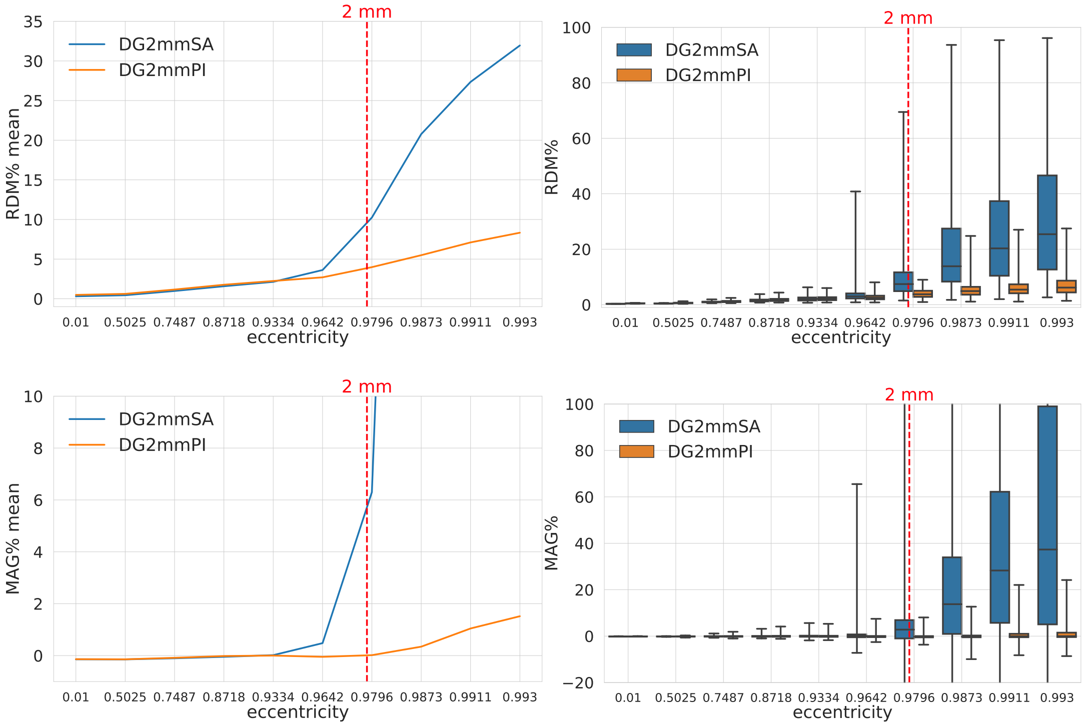

Figure 3.9.: Accuracy comparison of the secondary B-field $\mathbf{B}^s$ computation (1.13) of DG-FEM when the subtraction (blue) and the partial integration (yellow) approaches are used in a 2 mm hexahedral sphere model: visualized are the means (left column) and the boxplots (right column) of the RDM% (top row) and MAG% (bottom row), for tangentially oriented sources at logarithmically-scaled eccentricities. The red dashed line represents the eccentricity of 2 mm distance to the brain-CSF boundary. Note the different scaling of the y-axes.

secondary B-field is notable; in particular, PI outperforms SA for eccentricities greater or equal to the most relevant eccentricity, i.e., 0.9796, where the mean RDM% difference is around 10 pp and the absolute mean MAG% difference is around 1 pp.

In the next comparison, we focused on the most highly resolved mesh (1 mm) and analyzed the performances of both SA and PI. As already seen for the other mesh resolutions, the main increase can be seen after the boundary eccentricity, that is 0.9873, in this case.

If we analyze results for the most relevant eccentricity, i.e., 0.9796, the two methods are both delivering extremely accurate results and in general, the differences might be considered negligible. In the specific, when comparing mean

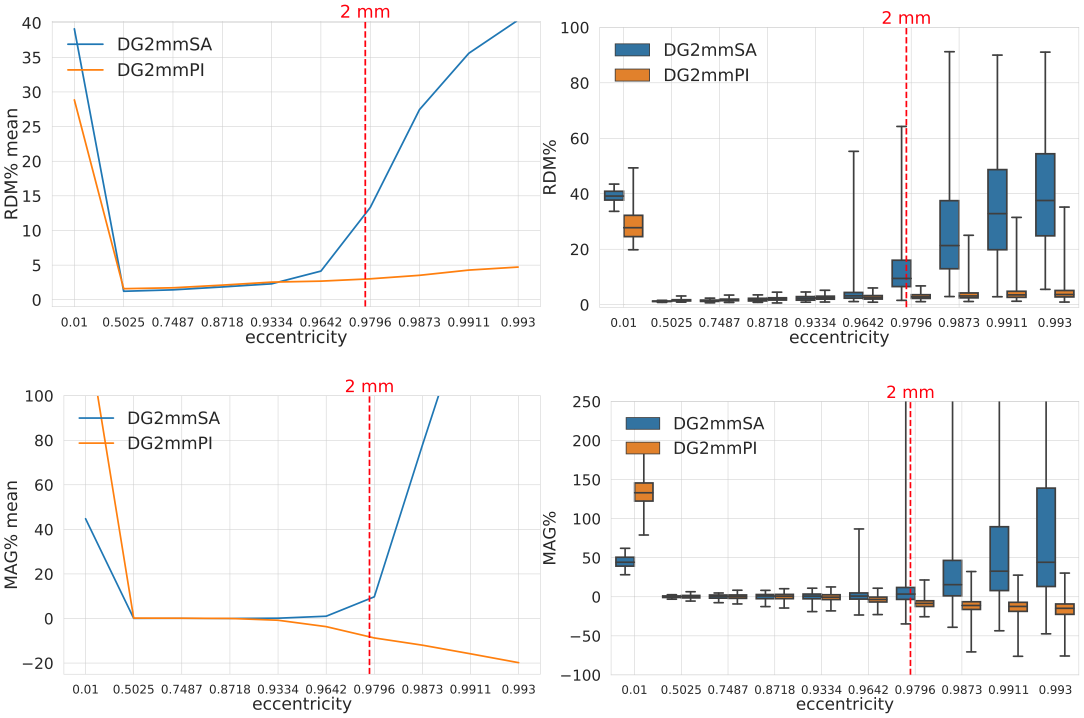

Figure 3.10.: Accuracy comparison for solving the MEG forward problem, i.e., the full B-field **B** (1.12) of DG-FEM when the subtraction (blue) and the partial integration (yellow) approaches are used in a 2 mm hexahedral sphere model: visualized are the means (left column) and the boxplots (right column) of the RDM% (top row) and MAG% (bottom row), for tangentially oriented sources at logarithmically-scaled eccentricities. The red dashed line represents the eccentricity of 2 mm distance to the brain-CSF boundary. Note the different scaling of the y-axes.

RDM% values, the PI slightly outperforms SA with a difference of 0.2 and it goes up to 17 pp for the most eccentric dipoles. The mean MAG% difference for the most relevant eccentricity is 0.06 pp where PI slightly outperforms SA. The maximum mean MAG% difference is achieved for the most eccentric dipoles, and it is around 56 pp, where again PI is more accurate than SA. If we look at the boxplots in Figure 3.11 (right column), we can see difference RDM% median, IQR and TR of 0.01 pp, 0.15 pp and 15 pp, respectively, showing the slightly better performing PI. The difference MAG% median, IQR and TR are 0.02 pp, 0.3 pp and 20 pp, respectively, where again PI is slightly outperforming SA. When studying the comparison between SA and PI for the full B-field computed in a 1 mm resolution mesh, we notice that the difference between the methods

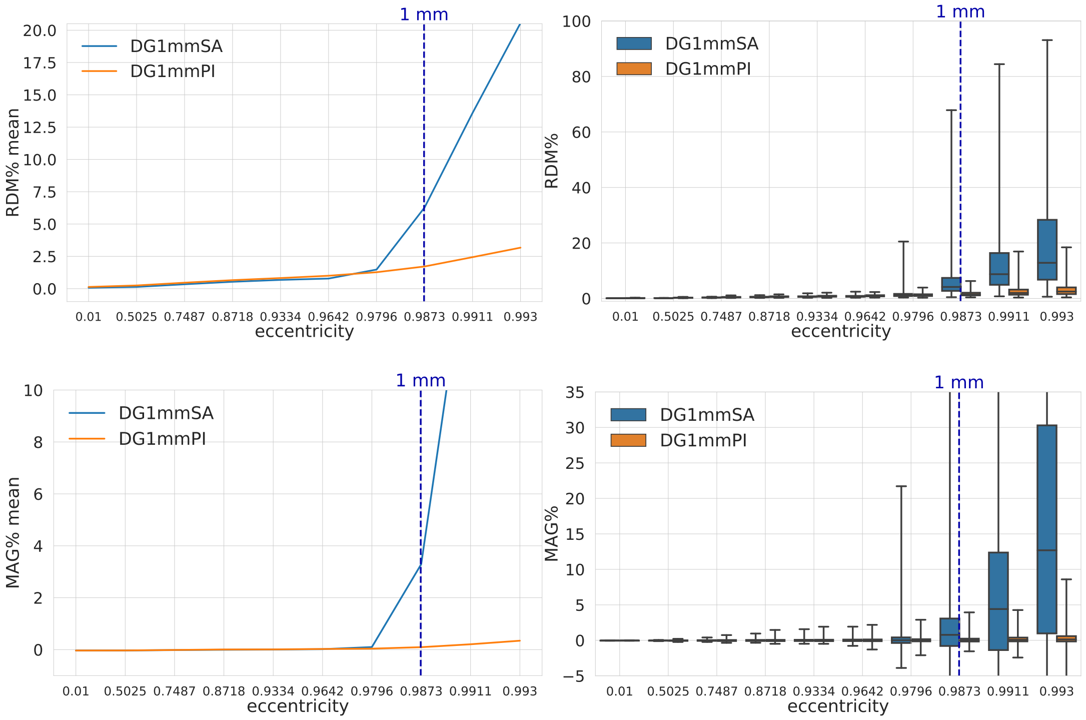

Figure 3.11.: Accuracy comparison of the secondary B-field $\mathbf{B}^s$ computation (1.13) of DG-FEM when the subtraction (blue) and the partial integration (yellow) approaches are used in a 1 mm hexahedral sphere model: visualized are the means (left column) and the box-plots (right column) of the RDM% (top row) and MAG% (bottom row), for tangentially oriented sources at logarithmically-scaled eccentricities. The blue dashed line represents the eccentricity of 1 mm distance to the brain-CSF boundary. Note the different scaling of the y-axes.

for the most relevant eccentricity is negligible: at such high resolution the two methods achieve extremely accurate results, as already stated in Study 2 and 3.

Finally, in Figures 3.13 and 3.14, the cumulative relative frequencies for RDM% and MAG%, for both SA and PI and for all of the mesh resolutions are presented for the secondary and the full B-field, respectively. From Figures 3.13, we notice that PI 1 mm (in coral) delivers the best results in terms of both RDM% and MAG%. More specifically, 95% of the sources has an RDM% below 3.7% and a MAG% below ≈ 0.75%. With regard to the RDM%, SA 1 mm (light blue) 65% of dipoles has an RDM% below 1% and both for SA 1 mm and DG 2 mm (in blue) 80% of the dipoles has an RDM% below 5%. We observe that the curve corresponding to SA is very steep for very low RDM% values and then it grows

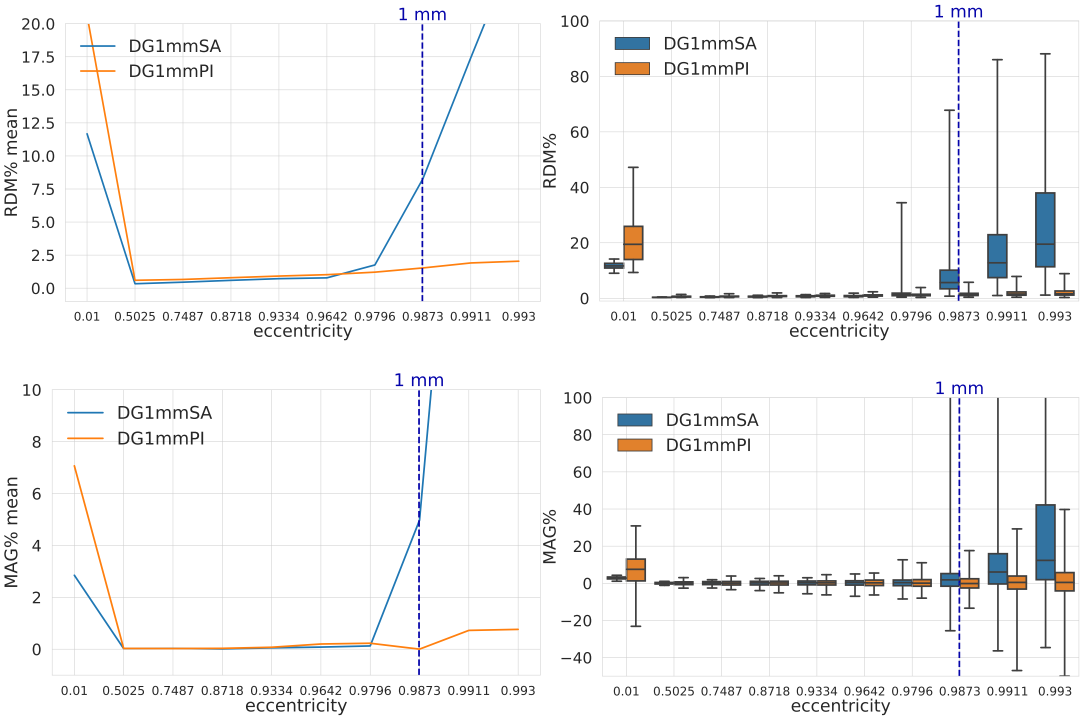

Figure 3.12.: Accuracy comparison for solving the MEG forward problem, i.e., the full B-field **B** (1.12) of DG-FEM when the subtraction (blue) and the partial integration (yellow) approaches are used in a 1 mm hexahedral sphere model: visualized are the means (left column) and the boxplots (right column) of the RDM% (top row) and MAG% (bottom row), for tangentially oriented sources at logarithmically-scaled eccentricities. The blue dashed line represents the eccentricity of 1 mm distance to the brain-CSF boundary. Note the different scaling of the y-axes.

slowly. On the other side, PI curves have a less steep behavior for the smallest RDM% values, but they reach higher values faster for higher RDM% values. This behavior is less visible in the MAG% curves, where the PI 1 mm (in coral) delivers the best results, followed by PI 2 mm (in red) and SA 1 mm (in light blue). The same general behavior is observed for the full B-field and omitted in this section.

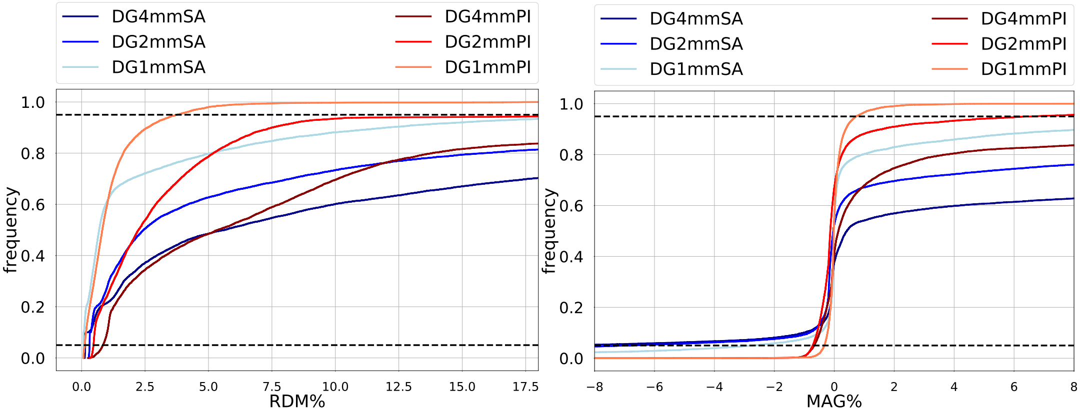

Figure 3.13.: Cumulative relative frequencies of RDM% (on the left) and MAG% (on the right) of the secondary B-field $\mathbf{B}^s$ (1.13) computed with DG-FEM for tangentially oriented sources at logarithmically-scaled eccentricities for two different source models, i.e., subtraction approach (SA) (in blue) and the partial integration approach (PI) (in green), and three different mesh resolutions, i.e., 4 mm, 2 mm and 1 mm. The dashed horizontal lines depict the frequencies of 5% a and 95%.

3.7. Proof of Concept in a Realistic Head Model

As a proof of concept, we computed one MEG forward solution using the DG-FEM approach in a more realistic scenario. Based on MRI recordings of a human head, a segmentation considering six tissue compartments (white matter, gray matter, cerebrospinal fluid, skull compacta, skull spongiosa, and skin) that includes realistic skull openings such as the foramen magnum and the optic nerve canal was generated. Based on this segmentation, a six-compartment realistically shaped head model was built, a hexahedral mesh of 2 mm resolution resulting in 508,412 vertices and 484,532 elements (Figure 3.15). More details about the model and its generation process can be found in [31]. Locations and orientations of the sensors were chosen accordingly to the CTF machine (OMEGA2005, CTF, VSM MedTech Ltd., Canada), see Figure 3.15. We simulated an auditory N1 MEG signal using the new DG-FEM method with conservative flux (3.19) in the 6 compartment realistically-shaped head volume conductor model. Following experimental evidence [67], the N1 current dipole was positioned in the secondary auditory cortex and oriented inwards-pointing and normally to the grey matter

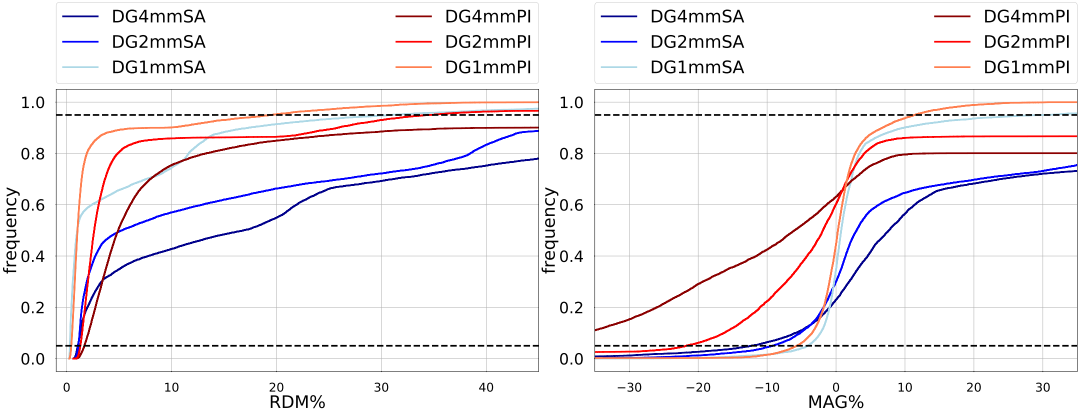

Figure 3.14.: Cumulative relative frequencies of RDM% (on the left) and MAG% (on the right) of the MEG forward problem solution, i.e., the full B-field **B** (1.12), computed with DG-FEM for tangentially oriented sources at logarithmically-scaled eccentricities for two different source models, i.e., subtraction approach (SA) (in blue) and the partial integration approach (PI) (in green), and three different mesh resolutions, i.e., 4 mm, 2 mm and 1 mm. The dashed horizontal lines depict the frequencies of 5% a and 95%.

surface. The result is shown in Figure 3.15. The subfigure on the left represents a sagittal slice through the head model, color-coding the 6 tissue compartments with different conductivities. In the middle and right subfigures, the results for EEG and MEG forward problem are presented. More precisely, the dipolar electrical potential map with frontal negativity and right occipital positivity is visualized on a cropped volume of the hexahedral mesh together with the underlying source (black arrow). The normally-oriented B-field MEG results at the 275 magnetometers was interpolated and visualized, showing a dipolar pattern that is 90 degrees rotated to the EEG one and, following the right-hand rule, the negativity (blue) is over central and the positivity (red) over temporal areas, in line with the experimental results [67, 41].

3.8. Conclusions

This chapter is about how we developed, implemented and evaluated the two new DG-FEM for solving the MEG forward problem, a conservative and a

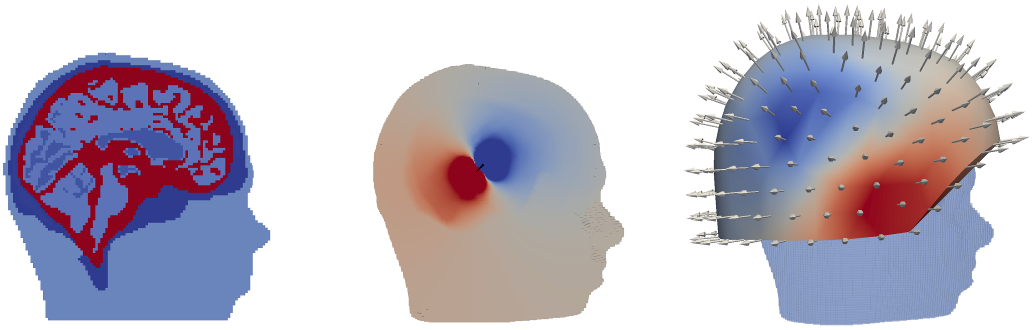

Figure 3.15.: Exemplary EEG and MEG forward computation for an auditory source computed using DG-FEM in a realistically shaped head model. Hexahedral mesh with 2 mm resolution, 6 compartments, sagittal slice (left); electric potential distribution visualized on the clipped volume conductor model in the sagittal plane where the auditory dipole (black cone) lies (middle); MEG solution interpolated on the radial magnetometers including a volume rendering of the head model (right).

non-conservative one.

First, we introduced and summarized the main mathematical theory of the DG-FEM. Second, we introduced the DG-FEM discretization of the weak EEG forward problem formulation in its general case together with a general formulation of the discrete conservation of charge property. Third, we described two possible ways to deal with the dipolar representation of the source, namely the subtraction approach and the partial integration approach. For each approach we made explicit the discrete conservative flux which has to be integrated into Biot-Savart's law, for the computation of the secondary B-field. Fourth, we deduced the MEG DG discrete representation of the general case together with each source discretization approach and we discussed some implementation aspects, such as the transfer matrix approach. Fifth, the DG-FEM for solving the MEG forward problem was evaluated in sphere models and results gathered and visualized in mean curves, boxplots and cumulative relative frequency curves. Sixth, we simulated an auditory N1 MEG signal using the new DG-FEM method with conservative flux (3.19) in the 6 compartment realistically-shaped head volume conductor model.

In a first analysis, we studied how large is the influence of a conservative representation of the electrical flux in the computation of the secondary B-field by adopting the DG-FEM. By comparing the DG-FEM with a conservative (3.19) and non-conservative (3.18) flux in a 4 mm multi-layer homogeneous sphere model, the high importance of DG-FEM with conservative flux could be worked out, outperforming the non-conservative DG-FEM scheme in all cases. In light of these results, the conservative flux DG-FEM was then used in all consecutive studies.

Results of the following two studies show the convergence of the DG-FEM when either the subtraction approach or the partial integration approach is adopted and the mesh resolution is increased, namely from 4 mm over 2 mm until 1 mm. In the same scenarios, the propagation of those errors to the computation of the full B-field are conducted and presented. In the fourth analysis we compared SA and PI for each mesh resolution. From this analysis, some considerations can be extracted and the general behavior of results can be summarized throughout the following points:

- DG-FEM for solving the MEG forward problem converges: when increasing the mesh resolution, the results get better;

- errors increase for increasing eccentricity. The convergence of the DG-FEM when the SA is used depends on the vicinity of the dipole to the brain-CSF boundary, as studied in details in [96]. We could assume that similar considerations apply for PI;

- with regard to the secondary B-field, there is a strong increase of RDM% and MAG% values when the considered dipoles belong to the boundary layer of elements between brain and CSF;

- the full B-field has high errors for dipoles with a low eccentricity. The more the dipoles approach the center of the sphere, the more their orientations become radial. It is well known (see Remark 1) that the full B-field is silent for radial dipoles, therefore there are divisions by zero in the error measures, which lead to high RDM% and MAG% values;

- for the most relevant sources, i.e., dipoles with eccentricity of 0.9796, and the mesh with highest resolution (1 mm), the minimum mean RDM%

value of 1.2 is reached when the PI is adopted, while the minimum mean MAG% value of 0.12 is reached when the SA is adopted;

- a spherical model with 4 mm resolution is too coarse and the results delivered are not accurate, i.e., median and mean RDM% and MAG% are way above 5%;

- a spherical model with 2 and 1 mm resolution is such that the delivered results are accurate, i.e., median and mean RDM% and MAG% are always below approximately 5%;

- SA performs topographically better than PI for eccentricities lower than the boundary-eccentricity, i.e., the eccentricities of the distances to the brain-CSF boundary, for each mesh resolution;

- PI performs better than SA for eccentricities higher than the boundary-eccentricity.

To conclude, DG-FEM with conservative flux implementation, i.e., a main feature of a DG-FEM discretization, turned out to be superior to the non-conservative flux variant. The new DG-FEM method showed proper convergence behavior with increasing mesh resolution, both when SA or PI is adopted. The comparison between SA and PI revealed that SA performs topographically better for eccentricities lower than the boundary-eccentricity, vice versa, PI performs better for eccentricities higher than the boundary-eccentricity. Finally, the DG-FEM MEG forward simulation in a realistic head model for an auditory source resulted in EEG and MEG topographies that are in line with practical findings in the field of auditory evoked responses. Therefore, for EEG or combined MEG/EEG source analysis scenarios, DG-FEM offers an interesting new alternative to CG-FEM, considering the importance of a high accuracy of the forward problem solution in MEG/EEG source reconstruction. We believe that this is the first time that a DG-FEM was adopted to solve the MEG forward problem. Some studies have been conducted when a CG-FEM approach was used instead and the discussion about the CG-FEM results and about the comparison between CG- and DG-FEM can be found in Chapter 2 and 4, respectively.

In this chapter, we did not evaluate the computational costs of the DG-FEM schemes for the computation of the MEG forward solution. Because of the higher number of degrees of freedom, DG-FEM is computationally more expensive than CG-FEM. However, the FEM transfer matrix approach (Appendix A.4) considerably reduces the computational costs of both approaches, so that this aspect gets less relevant for practical applications.

4. Comparison between CG- and DG-FEM

In this chapter we compare CG- and DG-FEM performances both in sphere models and in realistically shaped head models. Furthermore, we investigate the influence of the so-called *skull leakages* in the MEG forward computations.

4.1. Spherical Head Model Studies

In this section, the comparison between CG- and DG-FEM in sphere models is carried out. In the following, details about the CG- and DG-FEM simulations are described, and the results are visualized via mean curves, boxplots and cumulative relative frequency curves.

4.1.1. Materials and Methods

In this section, we describe the methods and the input data we used to compare our CG- and the new DG-FEM approaches described in the Chapters 2 and 3, respectively.

First of all, the new methods were implemented in *duneuro*. In particular, the MEG forward solutions were computed via *duneuro-python*. The input data we used for our simulations are the same as the ones used in the CG- and DG-FEM validations, in Chapters 2 and 3, respectively. More specifically, the volume conductor models with which we compared CG- and the two new DG-FEM implementations are 4-layer homogeneous sphere models represented via hexahedral meshes with three different resolutions, namely 4 mm, 2 mm and 1 mm. Details on the models and meshes are in Tables A.1 and A.2, respectively. We considered 10,000 tangentially oriented dipoles, distributed in 10 logarithmically scaled eccentricities (see Table A.3), and we evaluated the secondary and the full B-field in 256 point-magnetometers outside the sphere model at a fixed radius of 110 mm (see Figure A.1). The errors were assessed via the $RDM\%$ and $MAG\%$, defined in A.1 and A.2, respectively. More details about the input data and error measures can be found in Appendix A. Statistical results of numerical accuracies are visualized with mean curves, boxplots and cumulative relative frequency curves.

In addition to the previous Chapters 2 and 3, in this chapter we analyzed the effect of the so-called skull leakages. We have indeed already seen in Chapter 3 that in more realistic simulations, an aspect that should be more carefully studied is the fulfilling of the conservation of charge law and its implications on the application at hand. For the EEG, this has been studied in [31], where it was shown that the phenomenon of *skull leakages*, which occur as a consequence of not accurately fulfilling the conservation of charge law, can be overcome by using a DG-FEM instead of a classical CG-FEM. Leakage effects occur when a low conductive compartment of the head, i.e., the skull, is modeled too coarsely. This leads to scalp and cerebrospinal fluid elements being erroneously connected via single skull vertices or edges, a frequent case when segmenting, for example, children heads with thin skull compartments. Note that such skull leakage effects can also compromise the accuracy of transcranial electrical stimulation simulations [94, 57, 26, 90], in a reciprocal sense [89]. The study of [31] showed for EEG forward scenarios that DG-FEM can considerably outperform CG-FEM in skull leakage models, where the sphere model is discretized with a hexahedral mesh of 2 mm resolution and where at the same time the thickness of the skull compartment is deliberately reduced down to 2 mm ($seg\_2\_res\_2\_r82$), so that it contains many *leaky points*, i.e., vertices belonging to both an element labeled as skin and an element labeled as CSF or brain. See Table 4.1 and Figure 4.1 for details. Note that real skull holes are not investigated in this study.

The sources are the same as previously described. Even when not expecting similarly substantial error reductions on the MEG side, we used here the same leakage models as in [31] to investigate the influence of skull leakages on the presented CG- and DG-FEM MEG approaches.

	Segm. Res. (mm)	Mesh width h (mm)	Outer Skull Radius(mm)	#leaky points
seg_2_res_2	2	2	86	0
seg_2_res_2_r82	2	2	82	10,080

Table 4.1.: Parameters (from left to right) of the regular hexahedral meshes of the 4-layer sphere models used to investigate the influence of skull leakages on the presented CG- and DG-FEM MEG approaches: segmentation resolution (Segm. Res.), mesh width (h), outer radius of the skull (mm) and number of leaky points.

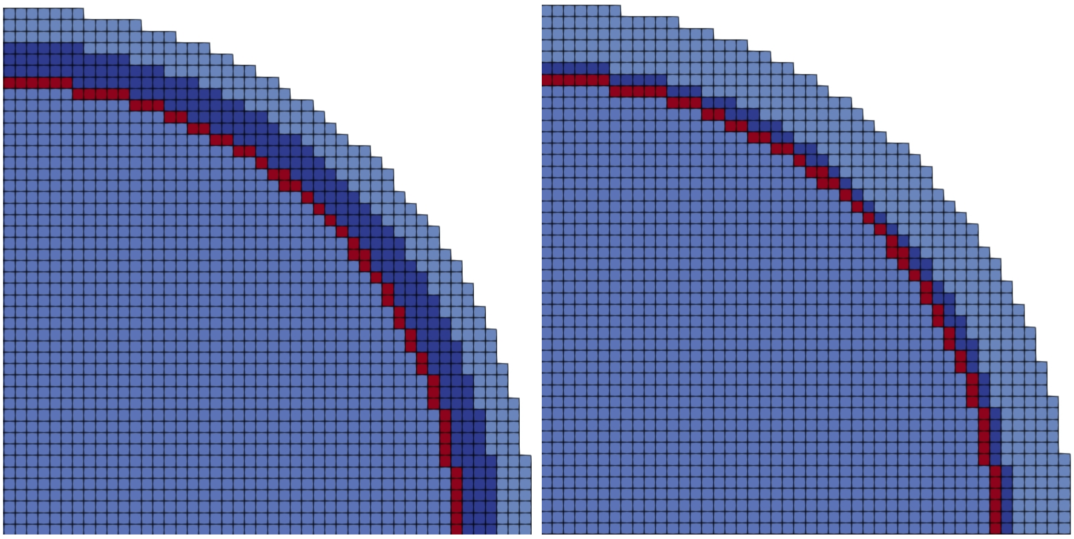

Figure 4.1.: Detail of the mesh with 2 mm resolution used in the computation (*seg_2_res_2*) on the left; detail of the mesh with 2 mm resolution and a thin skull layer used in the computation (*seg_2_res_2_r82*) on the right.

4.1.2. Results

In this section, we present results regarding CG-/DG-FEM comparisons when the subtraction or partial integration approach are adopted in three sphere models with increasing resolution (Study 1) and in a leakage model (Study 2). In the following discussion about results, we focus on the comparison between the two methods, rather than the performance of each method alone, which has been done for CG- and DG-FEM in Chapters 2 and 3, respectively.

Study 1: CG-/DG-FEM Comparison in Three Sphere Models

As a first CG-/DG-FEM comparison, we considered the spherical models described in Tables A.1 and A.2 and the results for both the subtraction and the partial integration approaches.

RDM% and MAG%s were evaluated both for the secondary B-field $\mathbf{B}^s$ (Figures 4.2, 4.4, 4.6) and the full B-field $\mathbf{B}$ (Figure 4.3, 4.5, 4.7), following equations (1.13) and (1.12), respectively.

With regard to the secondary B-field $\mathbf{B}^s$ results, we first analyzed the mean RDM% curve (Figure 4.2, top left) when the subtraction approach was adopted. In this plot we can distinguish the three different couples of curves: CG- and DG-FEM for 1 mm (*seg_1_res_1*), 2 mm (*seg_2_res_2*) and 4 mm (*seg_4_res_4*). If we focus on the 1 mm analysis, we notice a high accuracy (up to around 1.5%) for eccentricities smaller or equal to 0.9796 (i.e., 1.59 mm from the CSF compartment).

Even if in our current implementation, CG-FEM achieves slightly better results, the differences to DG-FEM are below 0.6 pp, so that in summary, DG-FEM constitutes an interesting alternative to the CG-FEM approach. Also for lower mesh resolutions of 2 and 4 mm, the performance of CG- and DG-FEM are very comparable for the realistic eccentricities up to 0.9796.

A similar observation can be made for the mean MAG% curve, as the general trend for the three couples of curves (i.e., CG-DG 1 mm, CG-DG 2 mm, CG-DG 4 mm) is the same as for the RDM% case. When focusing on sources with eccentricity value of 0.9796, the mean MAG% difference between CG- and DG-FEM remains below 0.09 pp. As for the boxplots for 1 mm mesh resolution (*seg_1_res_1*) and source eccentricity of 0.9796, the median RDM% difference is ≈ 0.4 pp (≈ 0.8% and ≈ 1.2% for CG- and DG-FEM, respectively); the IQR difference is around 0.2 pp (≈ 0.6% and ≈ 0.8% for CG- and DG-FEM, respectively) and the TR difference reaches almost 20 pp (Figure 4.2, top right).

In the same scenario, the MAG% medians are identically extremely low, i.e., $\approx$ 0.015%. The IQRs also do not differ, while, again the TR difference is around 20 pp (Figure 4.2, bottom right).

The results when focusing on the full B-field **B** in Figure 4.3 are similar to the ones in Figure 4.2. Even for the full B-field, both the CG- and DG-FEM show an overall very high accuracy and a negligible difference, especially when focusing on the 1 mm study and source eccentricity of 0.9796. The mean RDM% (Figure 4.3, top left) is $\approx$ 1% for CG-FEM and $\approx$ 1.7% for DG-FEM; the mean MAG% is $\approx$ -0.01% for CG-FEM and $\approx$ 0.1% for DG-FEM (Figure 4.3, bottom right). With regard to the RDM% boxplot (Figure 4.3, top right), the medians are $\approx$ 0.8% and $\approx$ 1.15% for CG- and DG-FEM, respectively; the IQRs are $\approx$ 1% and $\approx$ 1.2% for CG- and DG-FEM, respectively, and the TRs are $\approx$ 3% and $\approx$ 20% for CG- and DG-FEM. In the MAG% boxplot (Figure 4.3, bottom right), we observe identical and extremely low values for the median ($\approx$ 0.01%) and for the IQRs ($\approx$ 0.8%). The difference of TRs is again bigger ($\approx$ 20 pp) because of a few outliers. Note that in Figure 4.3, we have extremely high errors for the lowest eccentricity of 0.01 because radial sources do not produce any magnetic field, as already discussed in Chapters 2 and 3.

In the following, we compared results for CG- and DG-FEM when the mesh resolution is increasing and the source was discretized with the partial integration approach. In Figures 4.4 and 4.5, results for secondary and full B-field are visualized, respectively.

At first we analyze results for the secondary B-field, in Figure 4.4.

If we consider the most relevant dipole eccentricity, i.e., 0.9796, and the mesh with highest resolution, i.e., $seg\_1\_res\_1$, the mean RDM% and MAG% difference is less than 0.5 pp and $\approx$ 0.001 pp, respectively, where CG is slightly outperforming DG. If we look at the highest eccentricity DG is performing slightly better than CG, with a mean RDM% and MAG% difference of $\approx$ 1 pp and 0.2 pp, respectively. With regard to the boxplots, Figure 4.4, right column, RDM% TRs and IQRs are approximately the same between CG and DG, and there is a slight difference (of 0.4 pp) in the medians, where CG is delivering moderately more accurate results.

In general, the performances are very high for both CG and DG, and the differences are negligible. With regard to MAG% boxplots, TRs are almost identical, IQRs and medians are lower for DG, but again the difference is very small, i.e.,

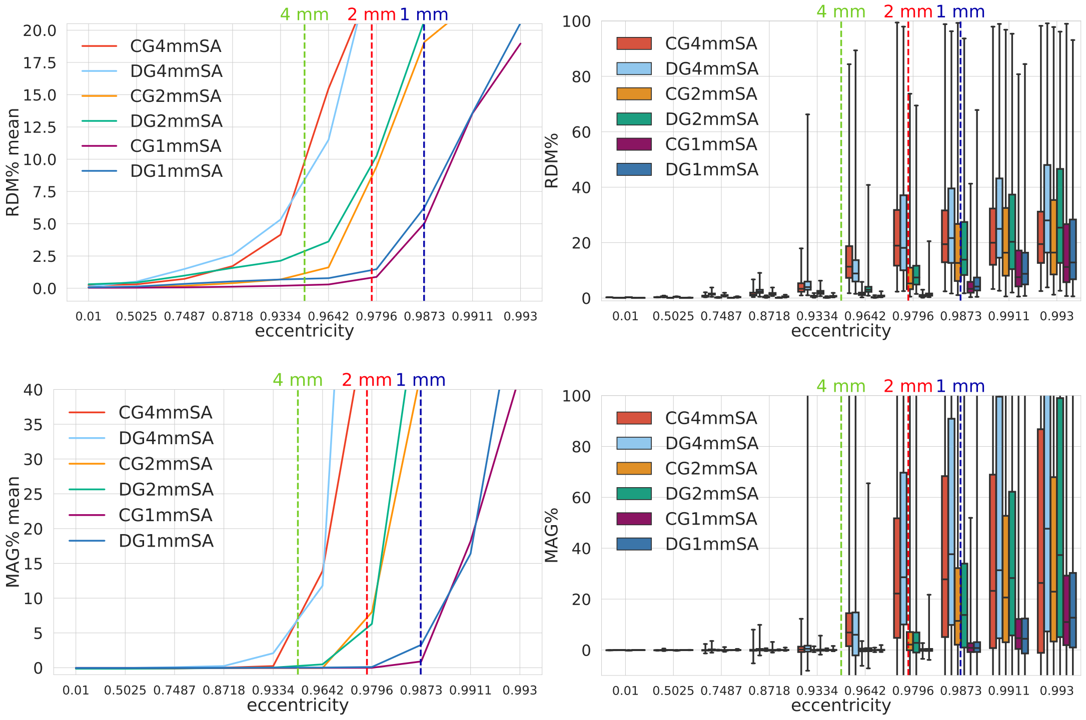

Figure 4.2.: Accuracy comparison for secondary B-field $\mathbf{B}^s$ computation (1.13) between CG-FEM (in warm colors) and DG-FEM with the conservative flux (in cold colors), for different mesh resolutions and when the *subtraction approach* (SA) is adopted. Visualized are the means (left column) and the boxplots (right column) of the RDM% (top row) and MAG% (bottom row), for tangentially oriented sources at logarithmically-scaled eccentricities. Dashed lines represent the eccentricities of 4 mm (green), 2 mm (red) and 1 mm (blue) distances to the brain-CSF boundary. Note the different scaling of the y-axes.

0.1 pp and 0.04 pp, respectively.

When considering the full B-field, the general behavior of the comparison is almost the same as the secondary B-field case. Results can be visualized in Figure 4.5. The difference RDM% and MAG% mean values are 0.4 pp and 0.15 pp, respectively, in favor of CG, for the eccentricity of 0.9796. For the highest eccentricity, the difference RDM% mean is 1.2 pp where DG outperforms CG and the difference MAG% mean is 0.2 pp, where CG delivers more accurate results. In the boxplots of Figure 4.5, for the most relevant eccentricity, the differences between CG and DG in terms of medians, IQR and TR are below 1 pp and therefore negligible. Furthermore, we observe some oscillations for higher eccentricities.

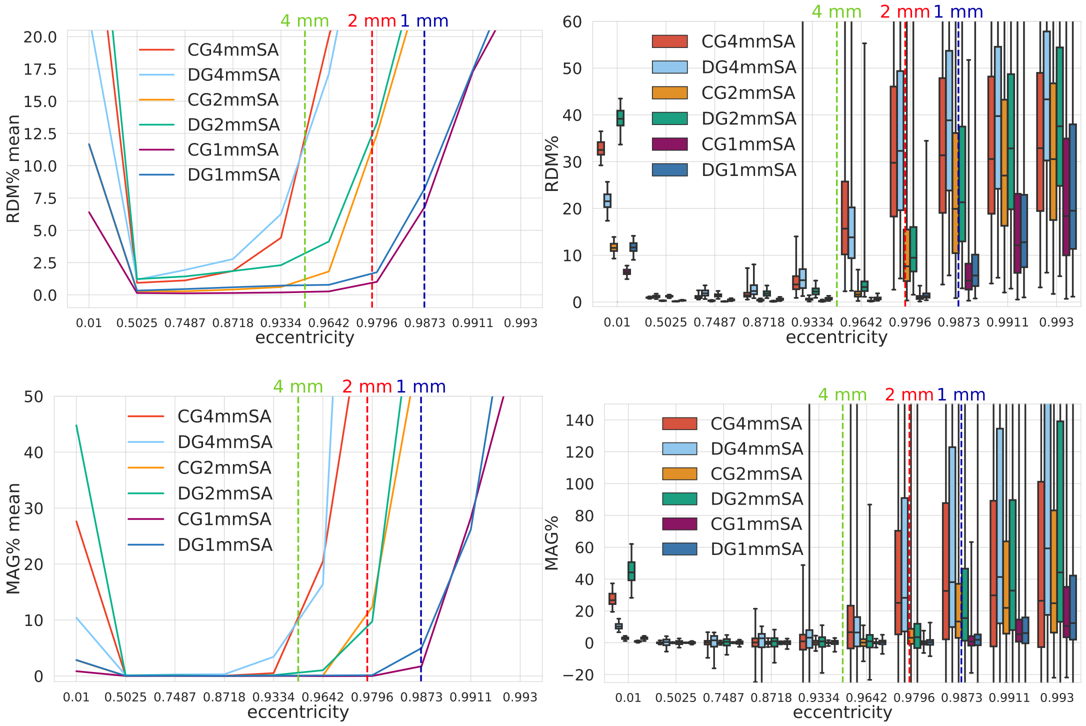

Figure 4.3.: Accuracy comparison for full B-field **B** computation (1.12) between CG-FEM (in warm colors) and DG-FEM with the conservative flux (in cold colors), for different mesh resolutions and when the *subtraction approach* (SA) is adopted. Visualized are the means (left column) and the boxplots (right column) of the RDM% (top row) and MAG% (bottom row), for tangentially oriented sources at logarithmically-scaled eccentricities. Dashed lines represent the eccentricities of 4 mm (green), 2 mm (red) and 1 mm (blue) distances to the brain-CSF boundary. Note the different scaling of the y-axes.

In the last part of this section we gathered CG and DG errors, for varying mesh resolution, i.e., 4 mm, 2 mm and 1 mm, and for varying source model, i.e., the subtraction approach (SA) and the partial integration (PI) approach. To improve readability, we will refer to CG-/DG-FEM and mesh resolution of 4 mm, 2 mm and 1 mm as *CG4*, *DG4*, *CG2*, *DG2*, *CG1* and *DG1*, respectively. In Figure 4.6 there is a comprehensive description of errors for the secondary B-field.

The best RDM% values are delivered when DG-FEM is applied in a 1 mm resolution head model and PI is adopted as discretization of the right-hand side, i.e., by DG1 PI. In fact, 95% of the dipoles have an RDM% around 4%.

Second to DG1 PI there is CG1 PI, for which the 95% of the dipoles have an

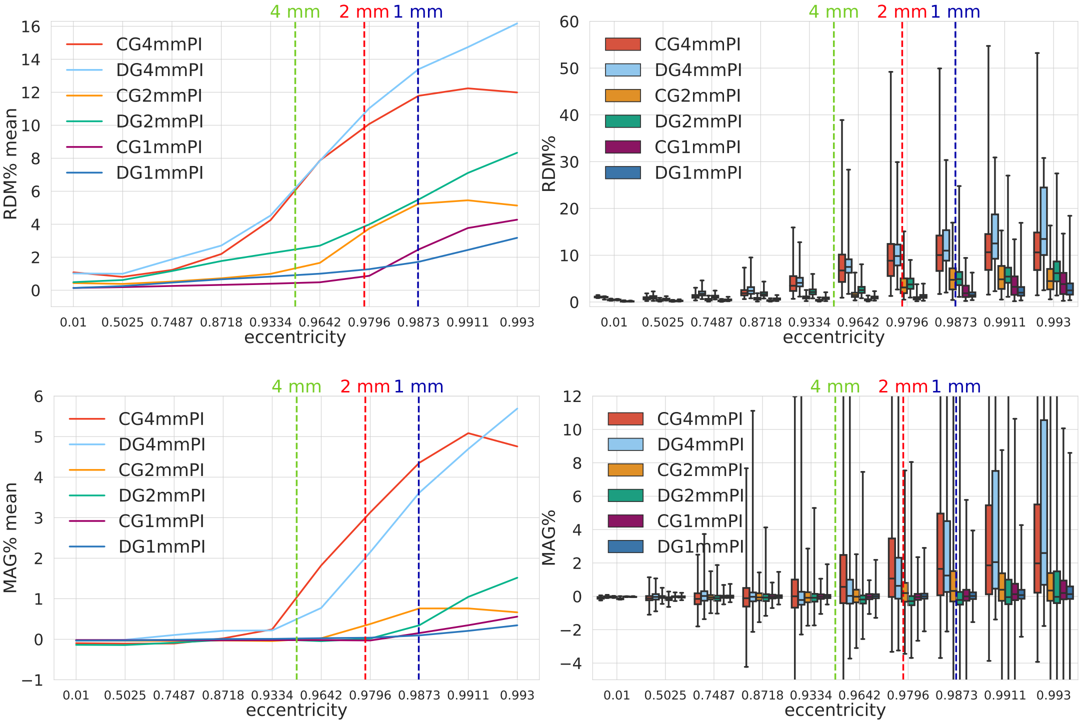

Figure 4.4.: Accuracy comparison for secondary B-field $\mathbf{B}^s$ computation (1.13) between CG-FEM (in warm colors) and DG-FEM with the conservative flux (in cold colors), for different mesh resolutions and when the *partial integration* approach (PI) is adopted. Visualized are the means (left column) and the boxplots (right column) of the RDM% (top row) and MAG% (bottom row), for tangentially oriented sources at logarithmically-scaled eccentricities. Dashed lines represent the eccentricities of 4 mm (green), 2 mm (red) and 1 mm (blue) distances to the brain-CSF boundary. Note the different scaling of the y-axes.

RDM% of approx 6%. Furthermore, we observe that for low RDM% values CG2 SA and DG2 SA are delivering better RDM% values than CG2 PI and DG2 PI, while for higher RDM% values the opposite occurs. Notice that CG2 SA and CG4 PI outperforms DG2 SA and DG4 PI, while DG4 delivers more accurate results than CG4.

The analysis of the MAG% cumulative relative frequency, expressed in percentage, (CRF%) curves is easier since the trends are clearer. DG1 PI outperforms all other modalities, followed by CG1 PI, DG2 PI and CG2 PI. With regard to DG2 PI, the CRF% curve is steeper than the one of CG2 PI for low MAG% values, while it becomes less and less steep for higher MAG% values. In both

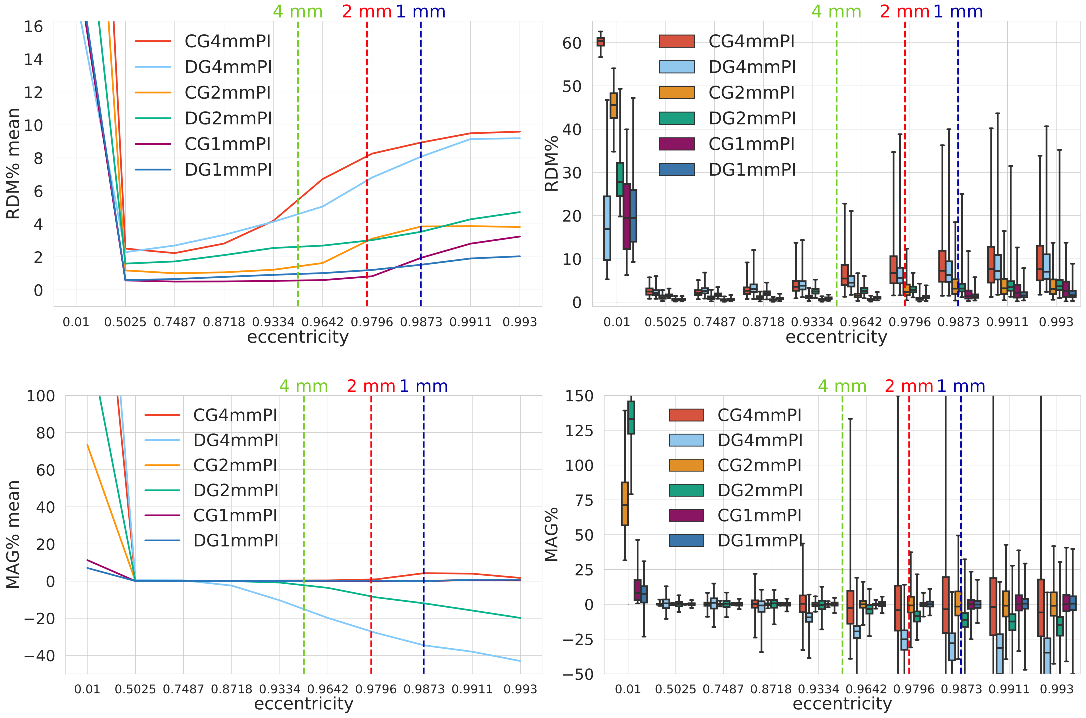

Figure 4.5.: Accuracy comparison for full B-field **B** computation (1.12) between CG-FEM (in warm colors) and DG-FEM with the conservative flux (in cold colors), for different mesh resolutions and when the *partial integration* approach (PI) is adopted. Visualized are the means (left column) and the boxplots (right column) of the RDM% (top row) and MAG% (bottom row), for tangentially oriented sources at logarithmically-scaled eccentricities. Dashed lines represent the eccentricities of 4 mm (green), 2 mm (red) and 1 mm (blue) distances to the brain-CSF boundary. Note the different scaling of the y-axes.

cases, i.e., PI CG2 and DG2, 85% of the dipoles have a MAG% of ≈ 2%. For CG2 and DG2 PI the 95% of sources have a MAG% of around 4% and 6%, respectively.

With regard to the other methods, results for DG1 SA are approximately the same as the ones of CG1 SA. DG4 PI and CG4 PI clearly perform worse but their relative behavior is similar to the one between DG2 PI and CG2 PI. In both cases, 80% of the sources have an RDM% of 5%.

This result is in line with the previously discussed results in Chapters 2 and 3. The behavior of the full B-field, visualized in Figure 4.7, is very similar to the one of the secondary B-field in Figure 4.6 and the description is omitted here.

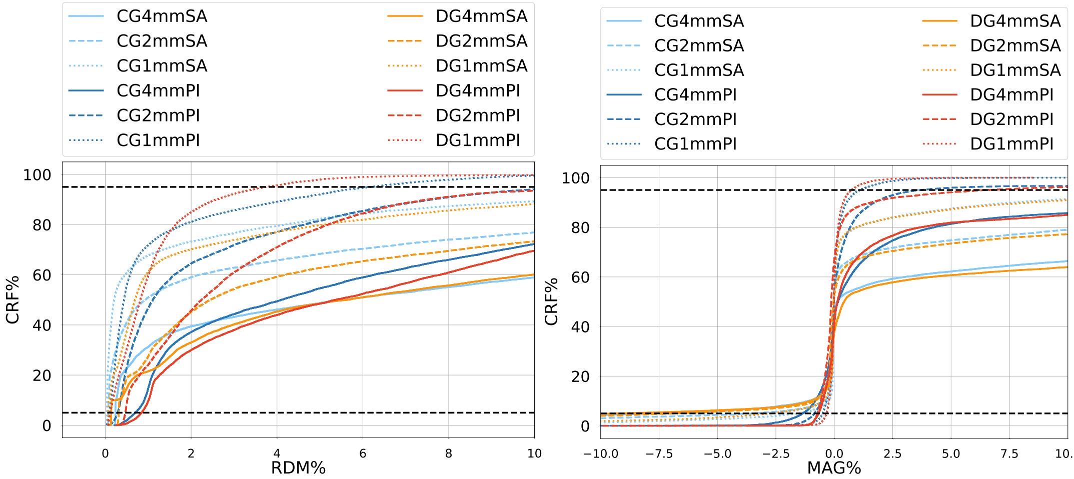

Figure 4.6.: Cumulative relative frequencies of RDM% (on the left) and MAG% (on the right) of the secondary B-field $\mathbf{B}^s$ (1.13) computed with CG- and DG-FEM in three sphere models with different mesh resolutions, i.e., 4 mm, 2 mm and 1 mm, for CG SA (in light blue), CG PI (in dark blue), DG SA (in light orange), and DG PI (in dark orange). The dashed horizontal lines depict the frequencies of 5% and 95%.

Study 2: CDG-FEM Comparison in a Leaky Sphere Model

Motivated by the EEG results of [31], where DG-FEM could clearly outperform CG-FEM in skull leakage scenarios, this section is concerned with the comparison of CG- and DG-FEM for the same skull leakage scenario, but for the MEG case. Therefore, a *leaky sphere model* ($seg\_2\_res\_2\_r82$) was constructed using an outer skull radius of 82 mm (instead of 86 mm as in the previous sections), resulting in an only 2 mm thick spherical skull compartment. Then, a 2 mm resolution hexahedral model was constructed, resulting in 10,080 skull leakages, see Figure 4.1. Also in this study, only tangentially-oriented dipoles were examined (see Appendix A). Similarly to [31], we limited our comparison only to the scenario when the SA was adopted.

In Figure 4.8, we computed RDM% and MAG% mean curves (left column) and boxplots (right column) for the leaky skull spherical model scenario ($seg\_2\_res\_2\_r82$) compared to the *non-leaky* skull spherical model scenario ($seg\_2\_res\_2$).

We observe that, in contrast to the improvement that DG-FEM could achieve in the EEG case [31], the skull leakages do not visibly influence the numerical simulation of the secondary B-field $\mathbf{B}^s$ and, since the primary B-field $\mathbf{B}^p$ is also

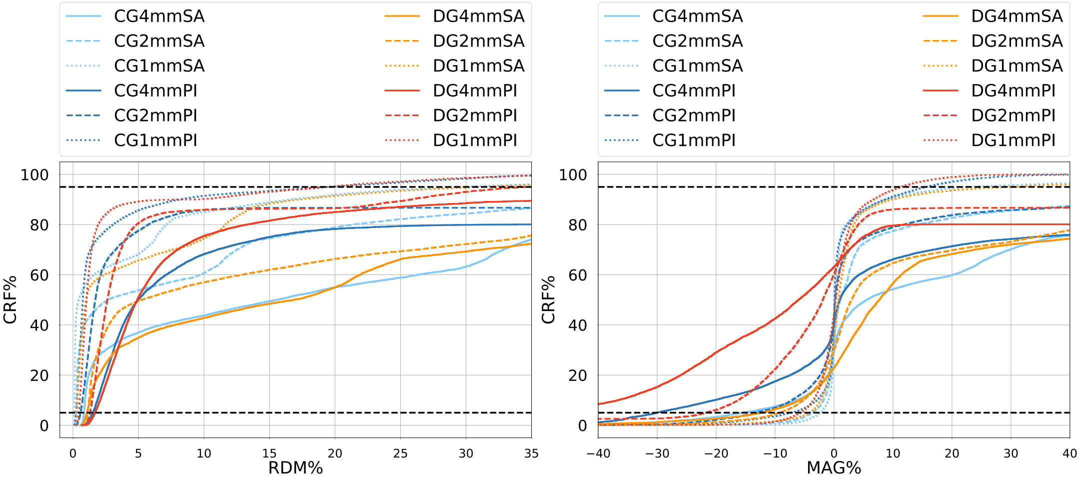

Figure 4.7.: Cumulative relative frequencies of RDM% (on the left) and MAG% (on the right) of the full B-field B (1.12) computed with CG- and DG-FEM in three sphere models with different mesh resolutions, i.e., 4 mm, 2 mm and 1 mm, for CG SA (in light blue), CG PI (in dark blue), DG SA (in light orange), and DG PI (in dark orange). The dashed horizontal lines depict the frequencies of 5% and 95%.

not influenced, thereby also the full B-field and thus the MEG forward problem. If we observe the plots in the left columns, we indeed notice that the curves of the leaky scenarios are completely overlaying the curves of the non-leaky scenarios, both for CG- and DG-FEM and both for RDM% and MAG% mean curves. Also in the boxplots we cannot distinguish the behavior of the RDM% and MAG% in the leaky or non-leaky scenarios.

4.2. Realistically Shaped Head Model Studies

To have a wider overview of the CDG-FEM performances, in this section we compute and compare the CG- and DG-FEM MEG forward solutions in a more realistic scenario. In the following, details about the realistically shaped head models, the sensor configurations and the source space are described and results are reported and visualized via CRF% curves.

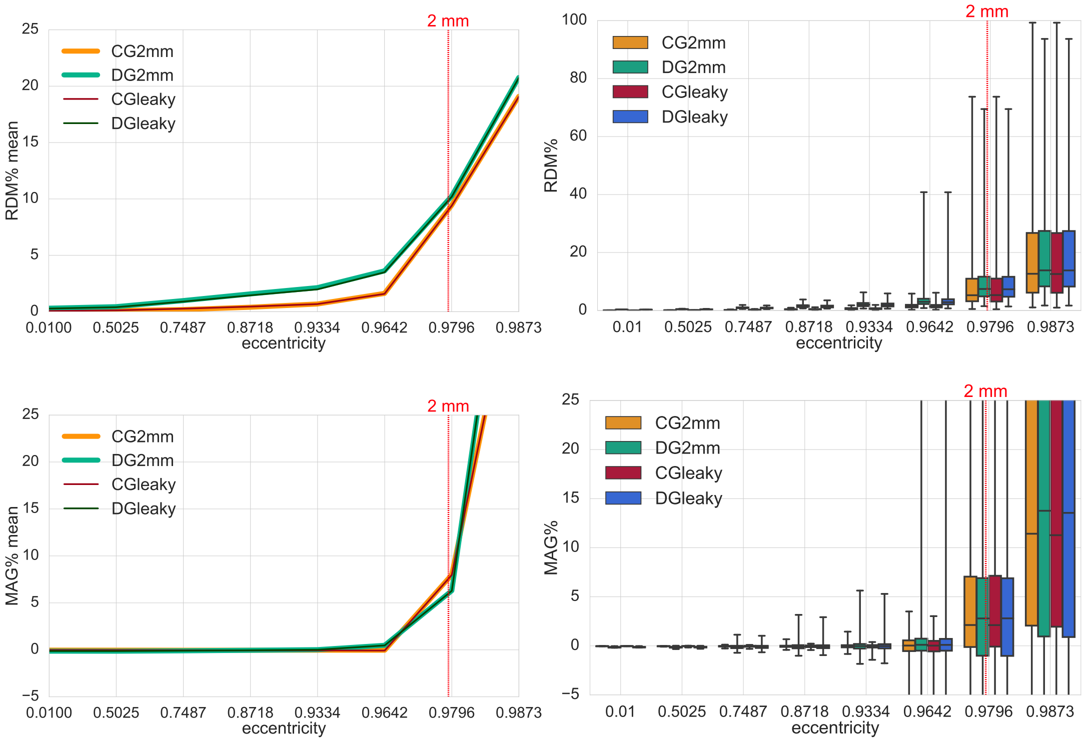

Figure 4.8.: Accuracy comparison for secondary B-field $\mathbf{B}^s$ computation (1.13) between CG-FEM (in warm colors) and DG-FEM with the conservative flux (in cold colors), in two different 2 mm hexahedral sphere models: *seg_2_res_2* and *seg_2_res_2_r82*, described in Table 4.1. Visualized are the means (left column) and the boxplots (right column) of the RDM% (top row) and MAG% (bottom row), for tangentially oriented sources at logarithmically-scaled eccentricities. The dashed red line represents the eccentricity of 2 mm distance to the brain-CSF boundary. Note the different scaling of the y-axes (top row).

4.2.1. Materials and Methods

In order to evaluate the performances of CG-FEM and DG-FEM in a realistic scenario, we considered three realistically shaped head models.

Based on MRI recordings, a segmentation considering six tissue compartments (white matter, gray matter, cerebrospinal fluid, skull compacta, skull spongiosa, and skin) that includes realistic skull openings such as the foramen magnum and the optic nerve canal was generated. Based on this segmentation, three realistic head models were generated. Two hexahedral head models with mesh resolutions of 1 mm and 2 mm were generated, resulting in 3,965,968 vertices and 3,871,029 elements, and 508,412 vertices and 484,532 elements, respectively, see Figure 4.9. As the model with a mesh width of 2 mm was not corrected for leakages, 1,164 vertices belonging to both CSF and skin elements were found. These leakages were mainly located at the temporal bone.

Figure 4.9.: Sagittal slices of three realistically shaped head models with different resolutions, and 6 compartments: skin (in light blue), skull spongiosa (in dark orange), skull compacta (in yellow), CSF (in dark blue), grey matter (in green) and white matter (in light orange). Hexahedral mesh with 2 mm and 1 mm resolution (left and center), reference high-resolution tetrahedral mesh (right).

To calculate reference solutions, a high-resolution tetrahedral head model with 2,242,186 vertices and 14,223,508 elements was generated. For further details of this model and of the used segmentation, we refer to [31].

The conductivities were chosen according to [31].

18,893 source positions were placed in the gray matter with a normal constraint. Locations and orientations of the sensors were chosen accordingly to the CTF machine (OMEGA2005, CTF, VSM MedTech Ltd., Canada), see Figure 3.15.

For both the CG- and DG-FEM, solutions in the 1 mm and 2 mm hexahedral head model were computed and the RDM% and MAG% are evaluated in comparison to the solution of the CG-FEM calculated using the tetrahedral head model.

4.2.2. Results

For the realistic head models, the RDM% and MAG% in reference to the high-resolution tetrahedral model were computed.

The cumulative relative frequency curves of the RDM% and MAG% are shown in Figure 4.10 and 4.11, for the secondary and full B -field, respectively.

For both the secondary and the full B-field, RDM% and MAG% values are overall higher than the ones in sphere model simulations. This is due to the geometrical error between a tetrahedral mesh and hexahedral meshes.

In both scenarios, DG-FEM results are overall more accurate than CG-FEM results, nevertheless, the difference between RDM% and MAG% values for DG and CG are moderate.

In particular, with regard to the secondary B-field, in Figure 4.10, 95% of the dipoles have RDM% and MAG% values less than 30% and 40% for both DG1 and DG2, and CG1 and CG2, respectively. The percentage of dipoles which have an RDM% of 5% is in general very low: only 30% for DG1, 20% for DG2 and CG1 and 10% for CG2. On the other hand, approx 80% of the dipoles have a MAG% of 5%, with small differences between methods, i.e., $\approx$ 2 pp.

With regard to RDM% values, in Figure 4.10 on the left, we can see that the DG1 curve is the steepest, but it is overlapping with the DG2 curve from RDM% values of 20% on. Furthermore, DG2 and CG1 curves are overlapping for RDM% values comprises between 0 and $\approx$ 7%. The CG2 curve is clearly less steep than all the others.

When observing the MAG% curves, in Figure 4.10 on the right, we see that the curves relative to DG1 and DG2 are the steepest and almost overlapping for all MAG% values, while the difference between CG1 and CG2 is more visible. In general, the curves of DG1 and DG2 are steeper than the ones of CG1 and CG2, indicating a higher numerical accuracy.

With regard to the full B-field results, visualized in Figure 4.11, we can notice that the steepest curves are the ones relative to DG1 for both RDM% and MAG%, nevertheless, the difference in steepness with the CG1 curve is negligible.

95% of dipoles have an RDM% value of $\approx$ 20% when adopting DG1, DG2 and CG1, while 95% of dipoles have an RDM% value of more than 25% when adopting CG2.

With regard to the MAG% error values, there is a clear but moderate distinction between DG1-2 and CG1-2, namely, 95% of dipoles have a MAG% of 30% when DG-FE; is adopted and a MAG% of 50% in a CG-FEM scheme.

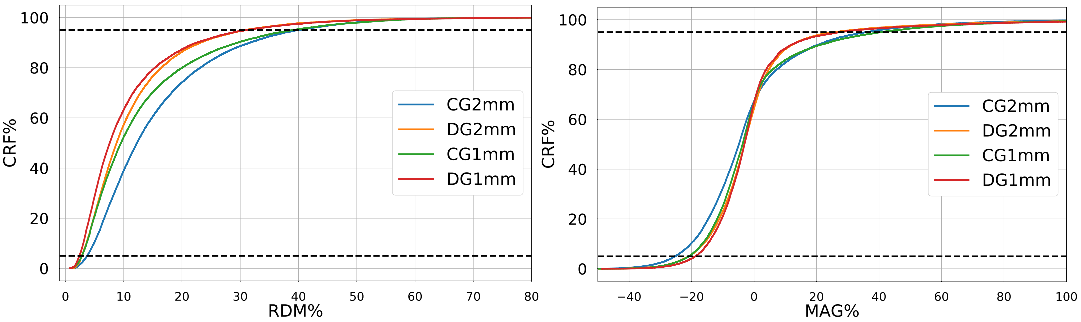

Figure 4.10.: Cumulative relative frequencies of RDM% (on the left) and MAG% (on the right) of the secondary B-field $\mathbf{B}^s$ (1.13) computed with CG- (in cold colors) and DG-FEM (in warm colors) in two realistically shaped head models with two different mesh resolutions, i.e.,2 mm and 1 mm, in reference to the high-resolution tetrahedral mesh. The dashed horizontal lines depict the frequencies of 5% and 95%.

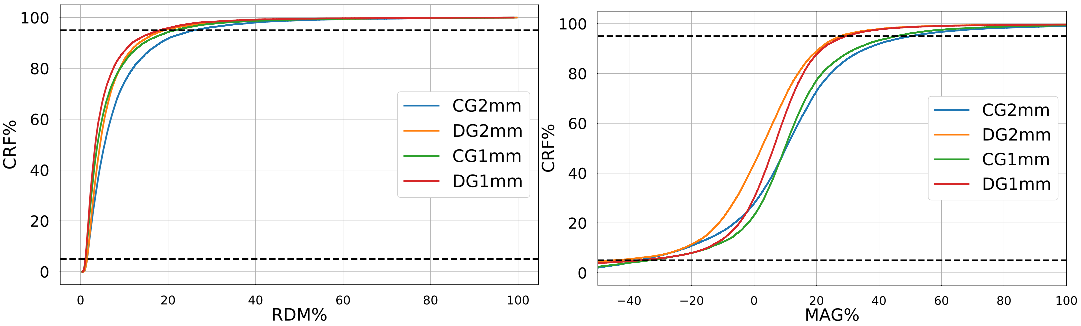

Figure 4.11.: Cumulative relative frequencies of RDM% (on the left) and MAG% (on the right) of the full B-field $\mathbf{B}$ (1.12) computed with CG- (in cold colors) and DG-FEM (in warm colors) in two realistically shaped head models with two different mesh resolutions, i.e.,2 mm and 1 mm, in reference to the high-resolution tetrahedral mesh. The dashed horizontal lines depict the frequencies of 5% and 95%.

4.3. Conclusions

This chapter is dedicated to the comparison between CG- and DG-FEM performances.

In the first section, the CDG-FEM comparison is conducted in sphere models. A first study is about the analysis of the behavior of CG- and DG-FEM in three spherical head models with increasing mesh resolution, i.e., 4 mm, 2 mm and 1 mm, when both the subtraction approach and the partial integration approach are adopted. A second study is about the investigation of the effects of skull leakages in the accuracy of the MEG forward solution: CG- and DG-FEM is used to compute MEG forward solutions in a hexahedral 2 mm resolution mesh where the skull compartment has been thinned on purpose and compared with MEG forward solutions in a hexahedral 2 mm with a thicker skull compartment.

In the last section of this chapter, the CG-/DG- comparison is conducted in three realistically shaped head models.

From Figure 4.6 and 4.7, where a comprehensive comparison between the methods is reported for both the secondary and the full B-field, respectively, we conclude that PI outperforms SA both in terms of topographical error and error in magnitude, and independently of the FE method used.

In particular, it can be noticed from Figure 4.6 and 4.7 that even the results related to CG2 and DG2 PI are notably more accurate than the ones related to CG1 and DG1 SA. Furthermore, for both the secondary and the full B-field, results related to DG1 PI are higher than results obtained in all the other setups. In particular, 95% of the dipoles have an RDM% of 4% and 18%, and MAG% of 1% and 10% , for the secondary and full B-field, respectively. The difference between DG1 PI and CG1 PI is nevertheless negligible.

The second study was about the influence of leaky points on the computation of the secondary B-field when DG-FEM is adopted (Figure 4.8). In this analysis we considered two different multi-layer homogeneous sphere models, namely *seg_2_res_2* and *seg_2_res_2_r82*. The difference between the two models is that in *seg_2_res_2_r82* the thickness of the skull compartment is deliberately reduced so that 10,080 leaky points are present. When comparing CG- and DG-FEM in the leaky model (i.e., *seg_2_res_2_r82*) and in the non-leaky model (i.e., *seg_2_res_2*), we observed that the results of the computation of the secondary B-fields are almost identical. This means that the skull leakages neither cause additional MEG forward modeling errors for DG-FEM, nor for CG-FEM. The situation is thus different from the EEG case, where remarkable errors for CG-FEM forward modeling were shown, while DG-FEM could strongly alleviate these additional leakage errors [31]. For MEG, in case of tangential sources, the return currents mainly flow parallel to the inner skull surface in the close environment of the source, so that the leakages do not affect the overall MEG forward solution. Furthermore, in the EEG case the largest effects of skull leakages were found for radially oriented dipoles, which are silent for the MEG.

We have to underline the fact that the results obtained in leaky scenarios are not to be confused with those where real holes of a certain diameter, e.g., from trepanation, are present in the skull compartment. The skull leakages investigated in [31] and, consequently, in this work are due to erroneous or, in general, poor representation of the skull compartment and not to real holes in the skull compartment.

[51] found that MEG signals are influenced by skull defects such as post-surgical skull openings. They examined the influence of skull holes in MEG signals via *in vivo* rabbit brain experiments, finding that the MEG signal amplitude reduced by as much as 20%, especially if the source is central under the skull defect. Their conclusion is that MEG source modeling requires realistic volume conductor head models that incorporate skull defects.

Furthermore, [52] showed that also MEG source analysis results are affected by skull defects. In particular, ignoring skull defects in the head model during reconstruction displaced and reoriented sources under a skull defect, and when skull defects were incorporated in the head model with their physical conductivity, the location and orientation errors were mostly eliminated.

The results obtained for realistically shaped head models show an overall higher accuracy gained by DG-FEM. Nonetheless, the difference between DG and CG errors in topography and in magnitude is moderate. These results reflect the behavior observed in sphere head model simulations.

A further important aspect to discuss is that, if a combined EEG and MEG source reconstruction is strived for [9, 34], the same forward model should be used for both EEG and MEG, because of considerable advantages in terms of implementation, accuracy and computational cost efficiency, as the MEG forward model is also based on the electric potential and thus the numerical solution of the EEG forward problem. We therefore employed the same method (CG- or DG-FEM, with conservative or non-conservative flux representation) for both EEG and MEG in our work at hand. Accordingly, in case of EEG or combined MEG/EEG source reconstruction in possibly leaky head models (e.g., in temporal bone areas or, more generally, in children investigations), the usage of DG-FEM is recommended, if only hexahedral models can be built. In fact, DG-FEM clearly improves EEG forward solutions in leaky models [31] and, at the same time, delivers reliable and accurate MEG solutions, as shown in the study at hand.

In conclusion, when compared to the CG-FEM, DG-FEM provided results that are in a comparable range of high accuracy. Furthermore, both methods are able to model realistic head volume conductor models with their tissue inhomogeneities and anisotropies.

In contrast to EEG studies, the so-called skull leakage effects did not play a crucial role for MEG. However, for EEG or combined MEG/EEG source analysis scenarios, DG-FEM offers an interesting new alternative to CG-FEM, considering the importance of a high accuracy of the forward problem solution in MEG/EEG source reconstruction.

5. EEG and MEG Sensitivity Maps based on the Finite Element Method

Even if generated by the same sources, MEG and EEG signals differ and carry complementary information. In a spherical representation of the head volume conductor model, the existing analytical solution for the forward problem is silent for radial sources and therefore it gets weaker for deeper sources. The situation is more complex when a realistically shaped volume conductor head model is adopted, as already stated by [3]. Moreover, there are studies where the sensitivity of both EEG and MEG to more realistic volume conductor head models is shown [47, 43, 38, 6, 49, 45].

Signal-to-noise ratio (SNR) maps offer a good estimate of EEG and MEG sensitivity to the activity of primary current sources in the human brain. SNR maps widen insights about the modulation of source orientations and locations to EEG and MEG signals and therefore lead to a correct interpretation of source reconstruction results, especially when EEG and MEG modalities are combined. Moreover, SNR is an essential measure of the detectability of epileptic spikes in clinical routine, it can guide the design of new sensors, it can help planning experiments. SNR maps are informative tools which allow for a correct interpretation of source reconstruction results and might guide the choice of preprocessing procedures to apply to recorded EEG and MEG signals.

Necessary ingredients to compute SNR maps are forward problem solutions, i.e., simulations of electric potentials and magnetic fields for given sources. As already deeply discussed in the previous chapters of this thesis, there are different ways to solve the forward problem, e.g., analytical formulas, boundary element

methods (BEMs), finite element methods (FEMs).
In [38] EEG and MEG SNR mappings for cortical sources extracted from MRI anatomical information have been computed and visualized, applying BEM in a three compartment isotropic head model.
In our study, we expand and extend the work of [38] by applying CG-FEM (cfr. Chapter 2) in three different head models, with increasing resolution, with the dual goal of investigating the reliability of such sensitivity maps and then to confidently analyze the results given by such mappings.
In order to assess the level of detail needed to achieve more reliable SNR maps, we computed and compared EEG and MEG SNR maps when three different head models were adopted, starting from an isotropic three compartment head model, where scalp, skull and brain are homogenized, to an isotropic four compartment head model, where the CSF compartment is added to the three previous ones, until a six compartment head model, where the skull is further refined into compact and spongy bone and the brain compartment into CSF, gray and anisotropic white matter.
Furthermore, we investigated the modulation of source orientation and depth on EEG and MEG sensitivity maps both for cortical and subcortical sources. The difference between EEG and MEG SNR values are visualized on the cortical surface, and SNR values for both cortical and subcortical sources are represented and compared via boxplots.

5.1. Materials and Methods

In this section, we describe the SNR formula used in this study and the variable it depends on.

5.1.1. Signal-to-Noise Ratio (SNR) mappings

We computed SNR mappings to cortical and subcortical dipolar sources for EEG and MEG and their sensitivity to three different head volume conductor models,

described in the following subchapters.
We adopted the SNR definition used in [38]:

$$SNR^i = 10log_{10}\left(\frac{(a^i)^2}{N}\sum_{k=1}^{N}\frac{(b_k^i)^2}{s_k^2}\right) \tag{5.1}$$

for each dipole i, where a^i is the source amplitude (i.e., 10 nAm, as suggested in [41, 38]), N is the number of sensors (i.e., 271 coils and 71 electrodes), b_k^i is the EEG or MEG forward solution at sensor k, and s_k^2 is the noise variance at sensor k, deduced from signal-free combined EEG/MEG recordings, as in [38].
In the following subchapters, the main variables of formula (5.1) are examined.
Furthermore, we computed the so called differential SNR maps related to cortical sources, following the formula

$$D^i = SNR^i_{MEG} - SNR^i_{EEG}, \tag{5.2}$$

for each dipole i.

5.1.2. Noise estimation

For the computation of s_k^2 in (5.1), we considered EEG and MEG data from an experiment aiming at measuring somatosensory evoked potentials (SEPs) and fields (SEFs) of a healthy 49 year old male volunteer.
The data was acquired with a sampling rate of 1200 Hz and an online lowpass filter of 300 Hz was applied to avoid aliasing. After the acquisition, the baseline of the data was corrected using the interval between -100 ms and -20 ms. In addition, the data was filtered with a notch filter for line voltage frequency (50 Hz and its harmonics) and a 20 to 250 Hz zero phase band pass filter in order to increase the signal to noise ratio as suggested in [19]. The continuous run was divided into trials that span 100 ms before and 200 ms after stimuli. Z-value and Kurtosis measures were used to identify and remove channels and trials with artifacts, both in EEG and MEG data. In total, 3 EEG channels and 3 trials in EEG and MEG data were excluded, ending up with 1195 trials in both measurements. In addition, the EEG data were re-referenced to common average

reference. The whole pre-processing procedure was performed via routines implemented in the Fieldtrip Toolbox [68].

Many techniques can be used to estimate the noise, we analyzed three methods. In the first method (m1), the signal was averaged over trials, and then the variance of the averaged trials was computed in the interval between -100 and -20 ms. Figure 5.1 presents the EEG and MEG signals averaged over trials, together with the considered prestimulus signals highlighted in yellow. The prestimulus is followed by the electric wrist stimulation artifact and the somatosensory signal components, which are not considered any further in this study.

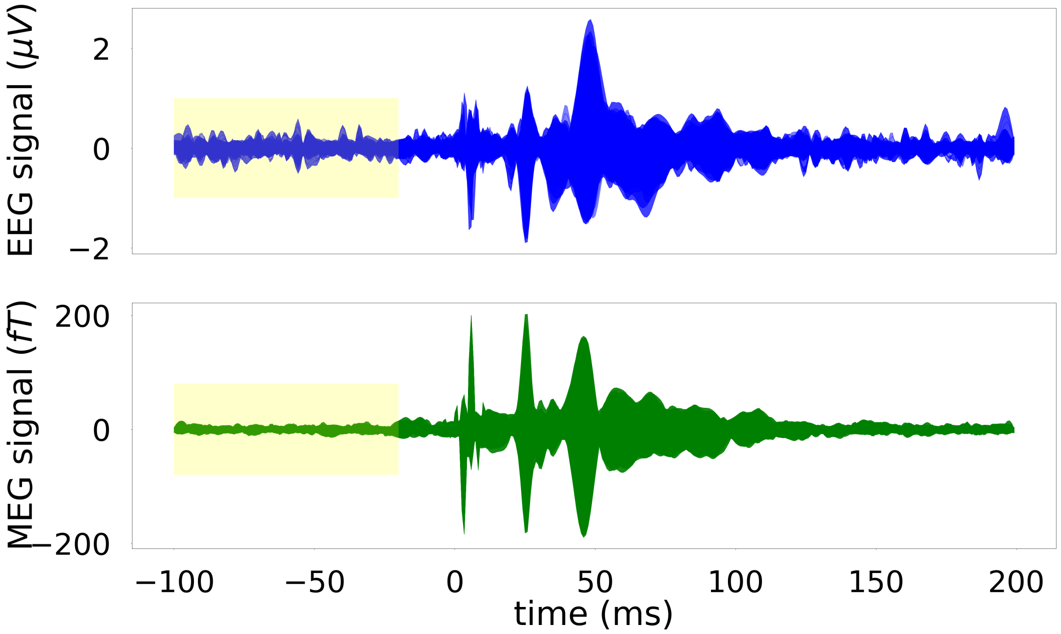

Figure 5.1.: EEG (upper subfigure) and MEG (lower subfigure) pre-processed signals averaged over 1195 trials. The prestimulus time interval considered for the computation of the variance for method (m1) is highlighted by the yellow box.

We additionally modify the number of trials involved in the averaging, namely 5, 50, 100 and all 1195 trials, in order to observe the behavior of the corresponding noise estimations. The results are gathered in Figure 5.2, upper row, where we can notice that the noise estimation decreases when increasing the number of trials considered in the average. We therefore clearly notice an intrinsic dependency on the number of trials when the noise is estimated with (m1).

In order to have a measure of the noise independent from the number of trials, in the second method (m2), we estimated the noise as the median over trials of the variances in the prestimulus interval of each trial. When varying the number of trials included in the median, the estimation of the noise remains more stable, therefore the measure can be considered as number-of-trials independent. See Figure 5.2, lower row.

As a third method (m3), we computed the variance of the whole signal in each prestimulus interval and assigned it as the noise estimation.

We compared the effects of using the three ways of computing the noise estimate in Figure 5.2, while in Figure 5.3 we depicted the relative difference between the noise estimations computed via (m1), (m2), (m3) and the variance of the whole signal as a mean of comparison.

From Figure 5.2, we observe that there is a clear difference (around three orders of magnitude in both the EEG and MEG cases) between the noise estimated with (m1) and the noise estimations given by (m2) and (m3). In contrast, the last two estimations ((m2) and (m3)) have negligible differences even when compared with the noise over the whole signal, in Figure 5.3.

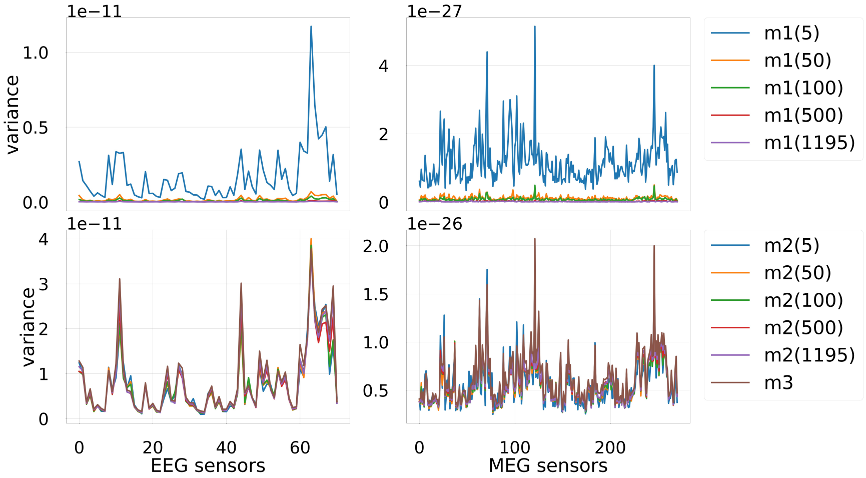

Figure 5.2.: EEG (left) and MEG (right) noise estimation following three different methods: (m1) variance over the prestimulus of the data averaged over trials, considering 5, 50, 100, 550 and 1195 trials (upper row); (m2) median over 5, 50, 100, 500 and 1195 trials of the variances over the prestimulus of each trial compared with (m3) the variance of the signal over each prestimulus intervals and the variance of the signal over the whole time interval (lower row). EEG and MEG variances are expressed in V^2 and T^2, respectively.

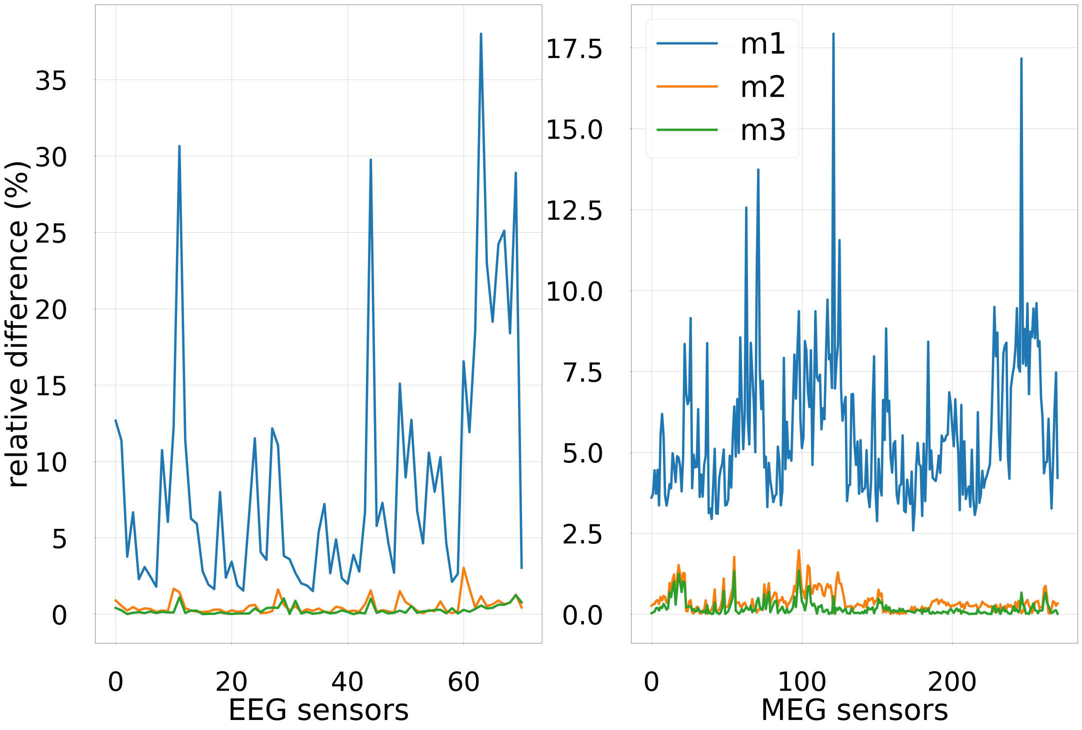

Figure 5.3.: EEG (left) and MEG (right) relative difference between the variance of the signal over the whole time interval and the estimated noise following the methods (m1), (m2) and (m3) considering all the trials.

In general, averaging over trials (cfr. (m1)) is often used to reduce the noise and therefore to increase the SNR of a signal. Nevertheless, the components of interest contained in a signal (P20-N20 component in our case) can also be clearly seen in the single trials [42]. We therefore further investigated the EEG and MEG signals utilized in this chapter to highlight this fact.

In Figure 5.4a and 5.4b we see, on the left, the signal corresponding to five trials for EEG and MEG corresponding to the *CP3* and *MLP33* sensors, respectively. On the top right the activity from all trials of the recording session time-locked to stimulus presentation at time zero is shown. Among others, the P20-N20 component time-locked to the stimulus is clearly visible. The plots at the bottom right of Figure 5.4 show the the averaged activity over trials, with clear relative evoked responses.

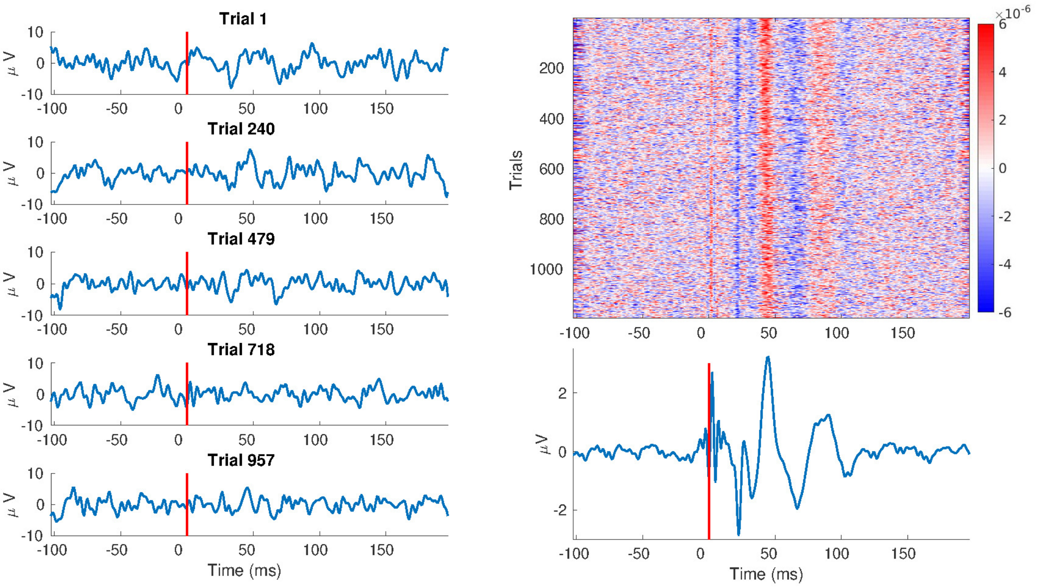

(a)

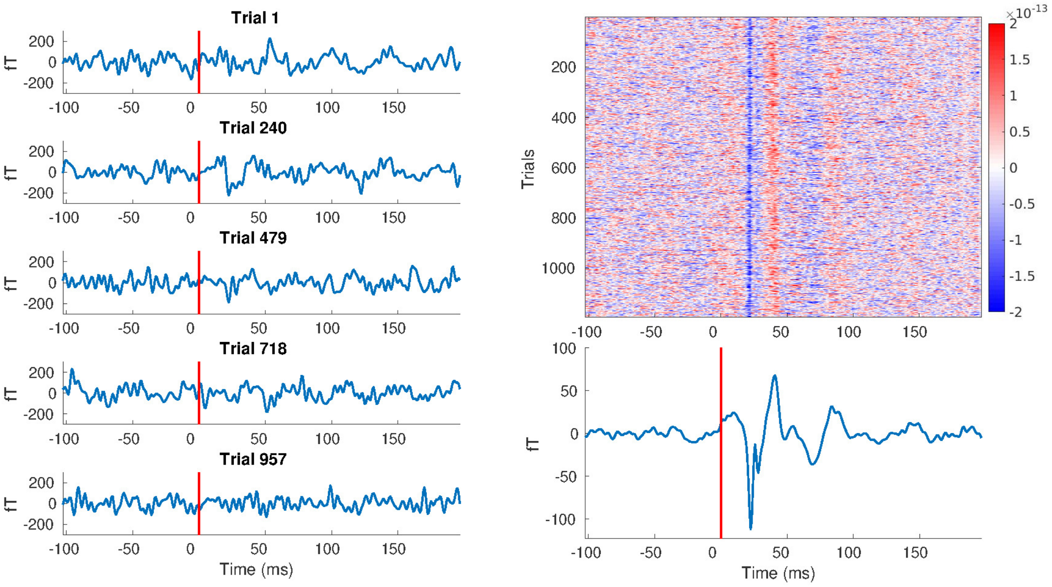

(b)

Figure 5.4.: On the left, EEG (a) and MEG (b) signals of five trials, corresponding to sensors CP3 (EEG) and MLP33 (MEG). On the top right, EEG (a) and MEG (b) activity of all trials along time, the color-coding indicates microvolts (a) and femtotesla (b). On the bottom right, EEG (a) and MEG (b) signal averaged over trials. The stimulus presented at time zero is marked with a vertical red line.

This investigation strengthen further our decision of adopting (m2) and all the trials for computing the noise level.

5.1.3. Finite element approach

The EEG and MEG forward problems were solved using the code implemented in the duneuro software [64] and validated in [65, 31, 71]. A lagrangian finite element method was applied for both the EEG and the MEG forward problem using the partial integration source modeling approach [53, 91, 97], described in Section 2.4. The transfer matrix approach was used to reduce computational costs [35, 95]. Results of these simulations represent b_k^i in formula (5.1).

5.1.4. Head models

As we have already seen, e.g., in Chapter 2 and 2, FEMs rely on a volumetric representation of the conductor head model. Three head models were constructed and utilized in this study: a simple 3 compartment isotropic head model (3CI), where skin, skull and brain are included, a 4 compartment isotropic head model (4CI) where the cerebro-spinal fluid (CSF) is added into the model, and a more detailed volume conductor head model with 6 compartments (6CA), i.e., skin, skull compacta, skull spongiosa, CSF, gray matter and anisotropic white matter. Specific features of the three models are gathered in Table 5.1.

A 3T scanner (MAGNETOM Prisma 3.0 T, Release D13 [Siemens Medical Solutions, Erlangen, Germany]) was used for the acquisition of MRI datasets. We measured a 3D-T1-weighted (T1w) fast gradient-echo pulse sequence (TFE) using water selective excitation to avoid fat shift (TR/TE/FW = 2300/3.51 ms/8o, inversion prepulse with TI= 1.1 s, cubic voxels of 1 mm edge length); 3D-T2-weighted (T2w) turbo spin echo pulse sequence (TR/TE/FA = 3200/408 ms/90o, cubic voxels, 1 mm edge length) and DTI using an echo planar imaging sequence (TR/TE/FA = 9500/79 ms/90o, cubic voxels, 1.89 mm edge length), with one volume with diffusion sensitivity b = 0 s/mm^2 (i.e., flat diffusion gradient) and 20 volumes with b = 1000 s/mm^2 in different directions, equally

Tissue	6CA (S/m)	4CI (S/m)	3CI (S/m)	
white matter	0.14	-	-	[75]
gray matter	0.33	-	-	[75]
brain	:	0.33	0.33	[75]
CSF	1.79	1.79	-	[16]
skull compacta	0.008	-	-	[25]
skull spongiosa	0.025	-	-	[25]
skull	:	0.01	0.01	[25]
skin	0.43	0.43	0.43	[25],[75]

Table 5.1.: Conductivity values (in S/m) of the three models created and used for the sensitivity study: *6CA*, 6 compartment head model with anisotropic white matter; *4CI*, 4 compartment isotropic head model and *3CI*, 3 compartment isotropic head model. The column indicates when the compartment has been split, e.g., skull compartment divided between skull compacta and skull spongiosa; while the dash indicates that the relative compartment has been neglected in the head model.

distributed on a sphere. Another volume with flat diffusion gradient, but with reversed spatial encoding gradients was acquired and used for susceptibility artifact correction [77]. During T1w-MRI measurement, gadolinium markers were placed at the same three positions nasion, left/right preauricular points as in EEG/MEG for landmark-based registration of MEG/EEG to MRI. All EEG/MEG and MRI measurements were done in supine position to reduce head movements, to stabilize the baseline of the brain activity stable [81] and to prevent erroneous cerebrospinal fluid (CSF) effects due to a brain shift when combining EEG/MEG and MRI [76]. The three images were co-registered and translated in the space defined by the CTF coordinate system, native space of EEG and MEG sensor positions. Afterwards, the images were resampled so that the voxels of the anatomical data are homogeneous, i.e., the voxel size is constant and the same along the three dimensions. This step facilitates the segmentation procedure. Furthermore, the images were cut above the lower lip of the participant, following the suggestions in [50]. Subsequently, the segmentation of the T1w and T2w was performed in order to separate 6 volumetric masks representing the 6 compartments we decided to include in the most realistic model, i.e., (6CA), following, e.g., [87]. The anisotropic conductivity tensor was deduced by the DTI, following the procedure described, e.g., in [10] and

[87]. The brain compartment was segmented via the FreeSurfer software[1] and the remaining pre-processing and creation of the volumetric masks was entirely performed via routines available in FieldTrip [68], in particular, the scalp and skull segmentation was done via the *spm12* software [70], embedded in FieldTrip. The Seg3d software was utilized for an easier visualization of both sliced volumetric masks and automatically generated surfaces, for quickly checking the output of the segmentation.

Once the masks were assembled, a volumetric tetrahedral mesh was created using the CGAL software [2] embedded in iso2mesh [32], resulting in 885,214 nodes and 5,335,615 tetrahedrons. In the case of the (3CI) and (4CI) head models, only the labels were modified accordingly, while the mesh remains the same as the one for the (6CA) head model, since the geometrical error was not studied in this work. In Figure 5.5 and 5.6, the three models and EEG/MEG sensors are visualized, respectively.

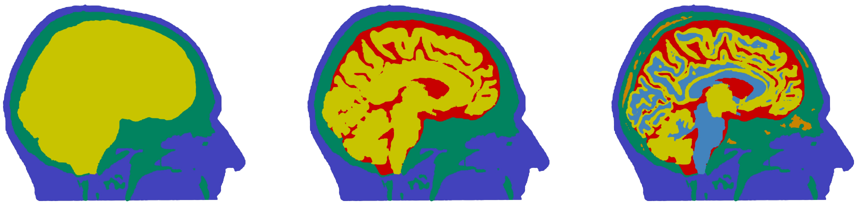
(a) (b) (c)

Figure 5.5.: Three head models used in the computation of the forward model solutions. In the (3CI) head model, in (a), the skin is depicted in blue, the skull in green and the brain in yellow; in the (4CI) head model, in (b), the additional CSF compartment is colored in red; in the (6CA) head model, in (c), the skull spongiosa is depicted in orange and the white matter in light blue.

---

[1] `http://surfer.nmr.mgh.harvard.edu`

[2] `https://doc.cgal.org/Manual/3.5/doc_html/cgal_manual/Mesh_3/Chapter_main.html`

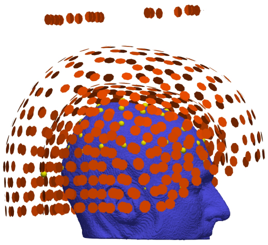

Figure 5.6.: EEG and MEG sensor configurations: 83 electrodes (in yellow) and 275 gradiometers (in red) with reference coils for noise cancellation.

5.1.5. Source spaces

In this study, two different source spaces were considered: a cortical surface and a subcortical volume. With regard to the former, the surface representation of the white matter given by Freesurfer was considered. Nodes lying on the white mantel were projected into the centroids of the correspondent closest elements belonging to the gray matter (Euclidean norm was used to compute the closest elements), and considered as dipole positions. The dipole orientations were chosen as the normals of the white matter nodes to the white matter surface (the normals were computed with the MeshLab toolbox[3]). In Figure 5.7, dipole positions and orientations are visualized on the white matter surface.

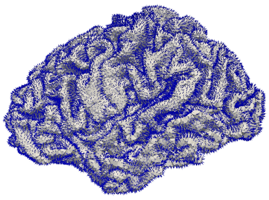

Figure 5.7.: Cortical dipole positions and orientations used in the simulations on the white matter surface.

The volumetric subcortical dipolar space was created extracting a subcortical volumetric mask (erosion of 1 voxel) from the Freesurfer parcellation, which identified 9 subcortical regions: cerebellum, thalamus, caudate, putamen, pallidum, hippocampus, amygdala, accumbens area and ventral diencephalon. Subsequently, a tetrahedral volumetric mesh was constructed with iso2mesh for each

---

[3] `http://www.meshlab.net/`

of the 9 subcortical regions identified by Freesurfer. The nodes of each mesh were considered as dipole positions.

Modeling the orientation of subcortical dipolar sources is not as trivial as modeling cortical dipole orientations. The neural generators of deep structures can be classified in *open* and *closed* field cells, according to the resulting electromagnetic field produced by their dendritic arborization [6]. In the first group there is a preferred orientation of the neural architecture, in the second group there is not. According to this fact, and following [6] and [49], in this study we considered the three Cartesian components for each mesh node as subcortical source orientations.

More details on the subcortical areas and number of dipoles considered for each area can be found in Table 5.2.

In Figure 5.8 the volumetric subcortical masks are visualized.

name	#dipoles
cerebellum	73,509
thalamus	10,815
caudate	3,846
putamen	5,592
pallidum	3,042
hippocampus	5,805
amygdala	2,451
accumbens area	1,065
ventral diencephalon	5,778

Table 5.2.: Subcortical areas included in the study with relative number of dipoles employed as subcortical source space.

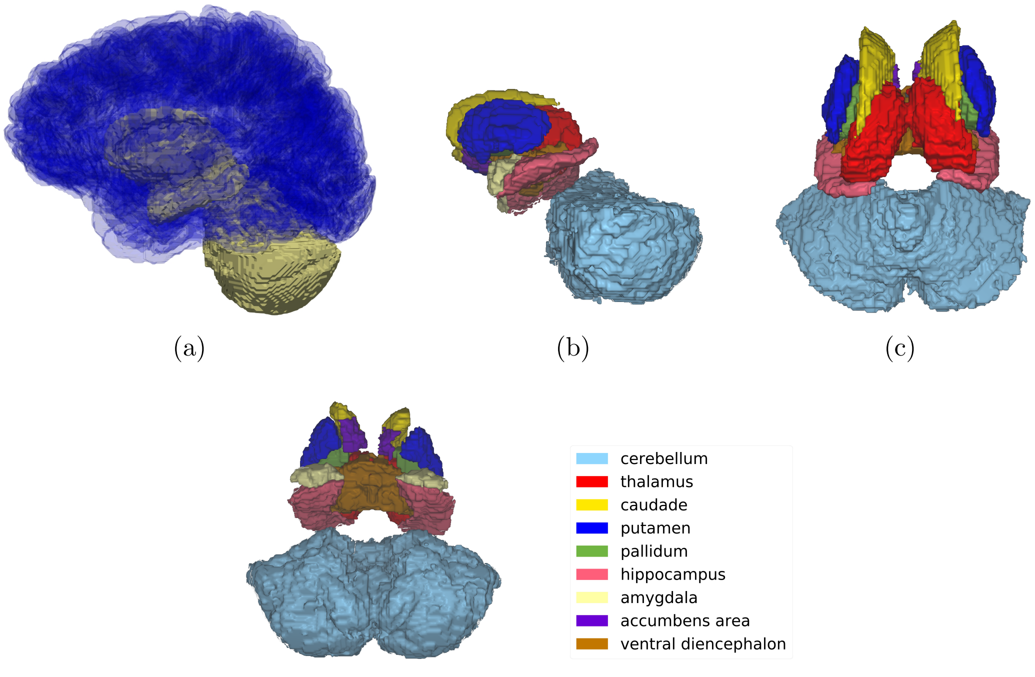

(a) (b) (c)

(d)

Figure 5.8.: (a) Visualization of cortical (in blue) and subcortical (in yellow) volumetric masks. (b) Visualization of nine subcortical structure masks segmented via Freesurfer and visualized in Seg3d [22] in sagittal view, (c) in transverse view from above and (d) from below.

A total of 278,621 cortical dipoles with normal orientations and 111,903 subcortical dipoles with Cartesian orientations were utilized for this study.

Depth and orientation estimation of cortical sources

In order to quantify the dipole depth and orientation modulation on the cortical SNR measures, we introduced two metrics, similarly to previous studies, e.g., [47, 87, 43]. More precisely, the depth of each cortical source was determined by the Euclidean norm to the closest node lying on the surface mesh of the inner skull, i.e., the surface mesh separating the CSF and the skull compartment. Furthermore, the angle between the cortical dipole orientation and the normal of the closest node on the inner skull surface was computed. In Figure 5.9 the source depths and source angles are visualized on the cortical source space.

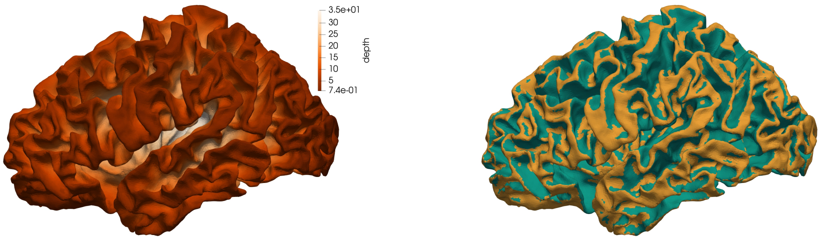

(a) (b)

Figure 5.9.: (a) Source depths and (b) source angles with respect to the closest nodes on the inner skull surface mesh visualized on the cortical source space. In (b), radial dipoles are depicted in orange and tangential dipoles in green.

In addition, we clustered source depths and angles into five bins to also enable a quantitative overview of the cortical SNR results, in addition to the SNR maps. The histogram of source depths and angles can be seen in Figure 5.10a.

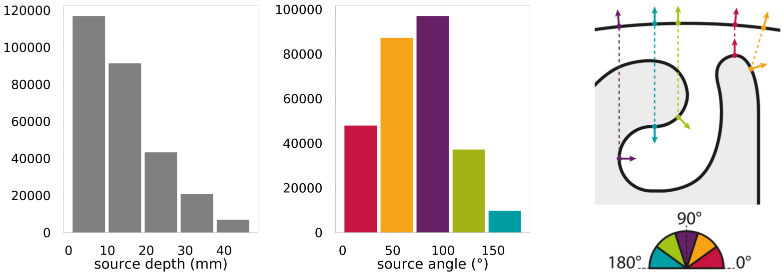

(a) (b)

Figure 5.10.: (a) Histogram of cortical source depth (left) and angle (right) represented in 5 bins. (b) Schematic representation of the cortical and inner skull surfaces (black curves) with examples of one dipole for each bin in the angle histogram (the color-coding guides the association).

We can interpret sources in the first and last bin in the source angle histogram as radial sources, the sources belonging to the central bin as tangential sources, and the remaining sources as sources with mixed orientations. In Figure 5.10b a schematic representation of the cortical and inner skull surfaces, in black, is depicted, together with an example of one dipole for each bin of the angle histogram (Fig.5.10a, on the right).

Singular Value Decomposition of MEG subcortical results

As discussed above, in most of the subcortical regions there is not a preferred orientation of the sources. Furthermore, it is well-known that radial sources do not contribute to the magnetic field measured outside of a spherical volume conductor model [78].
When dealing with realistically shaped head models, this is still mainly correct, however, in a weakened form such as the singular value for radial direction sources are a good factor weaker than for the two tangential directions.
For this reason, e.g., in [46], a singular value decomposition (SVD) of MEG forward solutions was performed to identify radial and tangential components of MEG and EEG solutions. More precisely, for each subcortical source space node i,, the corresponding MEG leadfield L has the dimension $n \times 3$ with n the number of MEG channels and the 3 Cartesian source directions. When applying a singular value decomposition, i.e., $L = USV^t$, the third column of V are the eigenvector corresponding to the smallest singular value (third diagonal entry in S). The latter represents well the weak contribution of a radially oriented source at source space node i to the MEG field, while the first two singular values in S indicate the much larger contribution of two dipoles in the tangential plane to the MEG. The MEG and, consequently, the EEG leadfield are then projected accordingly and the radial and two tangential components of the solutions are assigned.
Note that for sources belonging to a subcortical volume, the definition of orientation and depth used for cortical sources is more ambiguous, in particular, the projection of deep sources onto a reference surface mesh is difficult to justify. We therefore opted for the SVD analysis. To make an example, in a simplified spherical head volume conductor model, no source positioned at the midpoint contributes to the MEG, i.e., all directions are radial at the midpoint.

5.1.6. Visualization of the results

Inflated surfaces were produced in MeshLab starting from the white mantle and used to visualize (via ParaView[4]) the differential SNR maps (5.2) related to cortical sources when the (3CI), (4CI) or (6CA) head model was used. We used boxplots and heat maps to visualize the remainder of the results.

5.2. Results

The presentation of results is split between cortical and subcortical sources. For cortical sources, we computed the differential SNR presented in formula (5.2) for each of the three models, i.e., (3c), (4CI) and (6CA), on both the original cortical source space and the inflated cortical source space. Results can be observed in Figure 5.11.

The areas depicted in red are the areas where the SNR of the MEG is larger than the SNR of the EEG and the areas depicted in blue are the areas where the SNR of the EEG is larger than the SNR of the MEG. The same scaling from -10 dB to +10 dB is used for all head models to enable an easier comparison.

---

[4] https://www.paraview.org/

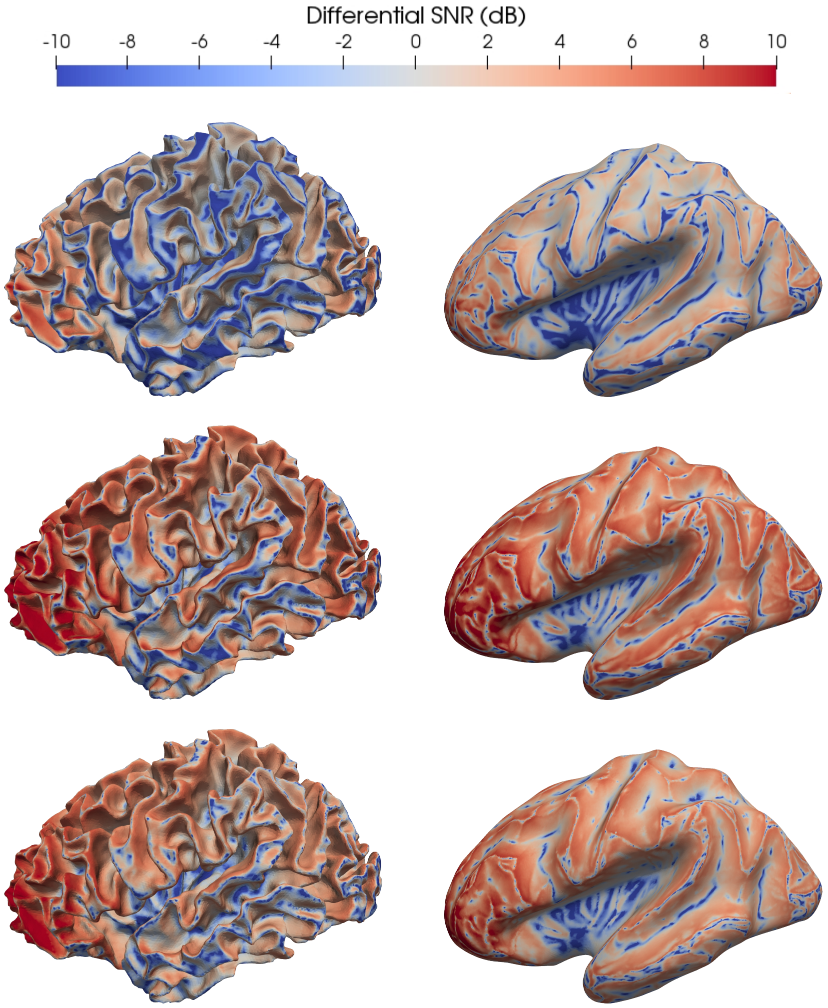

Figure 5.11.: Differential SNR when using head model 3CI (first row), 4CI (second row) and 6CA (third row) visualized on the cortical source space (left column) and on the inflated cortical source space (right column). The values are expressed in decibels. Areas where the SNR of MEG is larger than the one of EEG are depicted in red and areas where the SNR of the EEG modality is larger than the one of the MEG are depicted in blue. The same scaling from -10 dB to +10 dB is used for all head models to enable an easier comparison.

In all three models, we can observe that the SNR of EEG is larger at the gyri crowns and sulcal valleys, where the orientations of the sources are rather radial. In a complementary way, the SNR of MEG is larger at the sulcal walls, where the orientation of the sources is mainly tangential.

When comparing the maps throughout the models, we can observe that the areas where the SNR of EEG is larger is decreasing when increasing the number of compartments included in the model, especially when including the CSF compartment. Furthermore, the areas where the SNR of MEG are larger are not only growing in size (more red in middle and lower rows), but also the difference between the SNR's of both modalities is increasing (darker red in middle and lower rows). The CSF is thus weakening the sensitivity profile of EEG when compared to the one of MEG.

The distribution of the differential SNR between both modalities with respect to the distinction between gyri and sulci is highlighted by the inflation of the cortical source space (Figure 5.11, on the right column). MEG SNR values are particularly high in frontal areas, and this can be due to the better coverage of frontal areas by the MEG.

As a further study, we investigated the modulation of source depth and source orientation to SNR cortical values. In Figure 5.12, boxplots of SNR values sorted by increasing source depth (left subfigure, x-axis) and angle (right subfigure, x-axis) are reported.

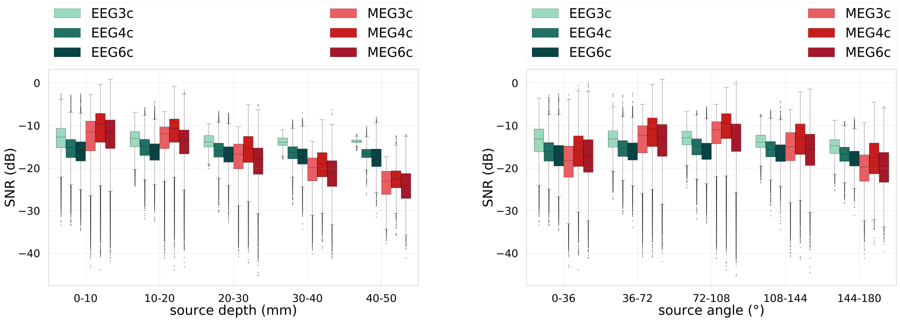

(a) (b)

Figure 5.12.: SNR values for cortical dipoles for EEG (in green shades) and MEG (in red shades) sorted by (a) source depth and (b) source angle for the 3 compartment isotropic (3CI), four compartment (+CSF) isotropic (4CI) and 6 compartment anisotropic (6CA) head models.

From Figure 5.12 we notice that EEG SNR values are only weakly modulated by the varying source depth and angle. This is not the case in the MEG case. In Figure 5.12a it is indeed noticeable that the more superficial sources are, the more MEG SNR values are higher than EEG SNR values. This trend gradually reverses when increasing the depth of the sources, until the case of the last bin, i.e., depth of 40-50 mm, where the scenario is the opposite: EEG SNR values are higher than MEG SNR values. From Figure 5.12b, we observe that MEG

SNR values are higher for more tangential sources, i.e., sources corresponding to the central bin, and lower for more radial sources, i.e., sources in the first and last bin.

In order to further investigate the modulation of source depth and orientation to SNR values, we created heat maps, i.e., bi-dimensional histograms, for EEG and MEG SNR values with respect to source depth and angle. See Figure 5.13.

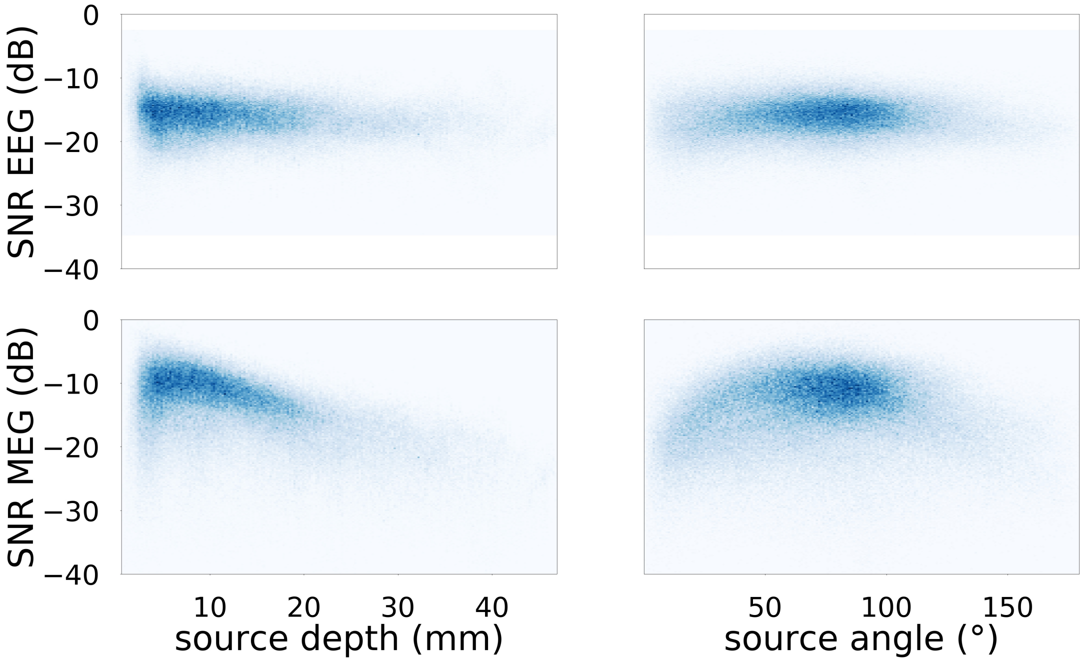

Figure 5.13.: heat maps of EEG (upper row) and MEG (lower row) SNR values in dependency of source depth (left) and source angle (right) from the inner skull surface. Cortical sources analyzed only.

In Figure 5.13 a weak modulation of source depth and orientation for EEG SNR values is confirmed. We notice a slow SNR decrease for increasing depth.

For MEG SNR values the behavior is quite different. In Figure 5.13 (lower left) we observe how SNR values are extremely low for very superficial sources, but there is a fast increase till reaching the maximum within few millimeters. After the peak, SNR values slowly decrease together with the distance between source positions and the surface of the brain compartment. For the visualization of SNR values for subcortical dipoles, we used boxplots, as, in this case, we are dealing with sources lying in a volume and not in a surface.

In Figure 5.14, the SNR values for EEG and MEG, and for all of the three head models, are shown when considering the radial and a tangential components of the EEG and MEG. The behavior of the SNR values of the second tangential orientation, i.e., the one related to the highest singular value in the SVD decomposition, was very similar and therefore omitted here.

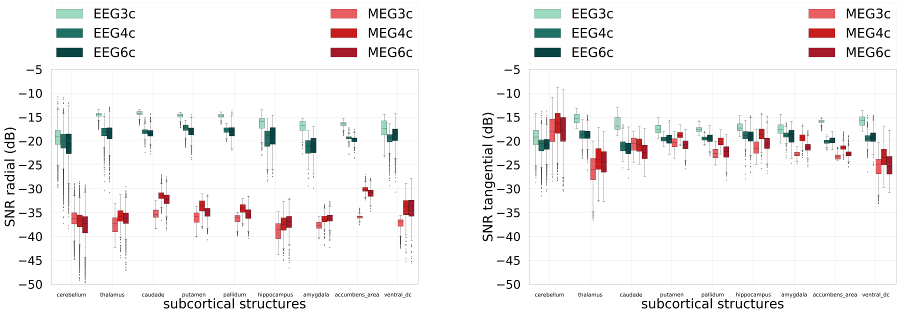

(a) (b)

Figure 5.14.: SNR values for radial, in (a), and the strongest (tangential), in (b), components of EEG and MEG for subcortical dipoles. On the x-axis the 9 subcortical areas considered are listed, on the y-axis, the correspondent SNR values for (3CI), (4CI) and (6CA). Cold colors are used for SNR values of EEG, warm colors for SNR values of MEG.

From Figure 5.14a, we can notice, first of all, that SNR values for EEG are systematically larger than SNR values for MEG. The differences between median values ranges between around 10 dB and 20 dB.

Second, the difference between results related to (4CI) and (6CA) is very low, whereas the difference between (3CI) and (6CA), or (3CI) and (4CI), is larger, for every subcortical areas. Third, the SNR values of EEG and (3CI) are larger than SNR values of EEG when (4CI) or (6CA) is considered. The opposite is shown for SNR values of MEG: the SNR values are lower when (3CI) is adopted in all subcortical areas but the cerebellum, where there seems to be no remarkable difference between the three models.

Finally, for the tangential case, in Figure 5.14b, we do not notice a clear difference between EEG and MEG. It is indeed remarkable that the range of MEG SNR values coincide with the one of the EEG SNR values.

As a further investigation, we reproduced SNR values when (m1) is adopted as noise estimation method. We compared the SNR values when (m1) and (m2) are used and the results are in Figure 5.15. We see that when (m1) is used, the trend is maintained, while the absolute values are remarkably higher than in the (m2) case. This is in line with the fact that the averaging procedure increase the SNR level of the signals. We can therefore conclude that the choice of (m1) and (m2) does not influence the main results.

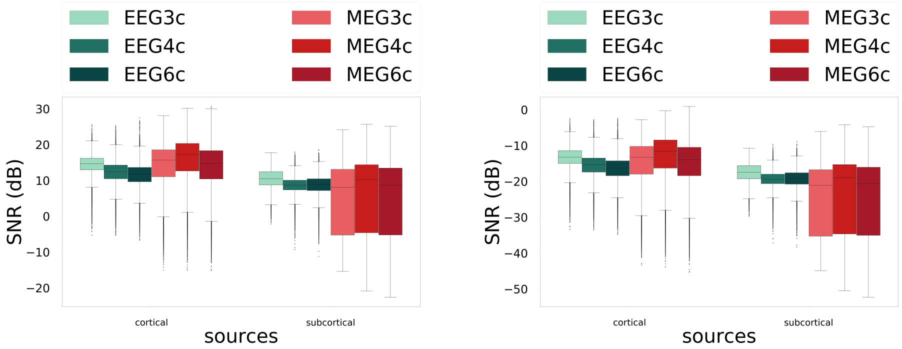

(a) (b)

Figure 5.15.: EEG and MEG SNR values for both cortical and subcortical sources when (m1), on the left, and (m2), on the right, are adopted to compute the noise level.

5.3. Discussion

In this chapter, we compute and compare SNR values when the EEG and MEG forward problems are solved for cortical and subcortical sources in three different volume conductor models: a three compartment isotropic (3CI), a four compartment isotropic (4CI) and a six compartment anisotropic (6CA) realistically shaped head models.

In Material and Methods we introduce the definition of SNR we adopted in the study together with the description of the variable the SNR formulation depends on. We started with the introduction of the EEG and MEG noise estimations and we continued with the EEG/MEG forward model simulations. In particular, the three head models and the two source spaces generation used for CG-FEM are described in details. Moreover, we introduced the definition of source depth and orientation we utilized to investigate their modulation on the SNR values. Finally, we described how we visualized results, i.e., SNR maps on the source space, boxplots and heat maps.

The Results section is divided in two parts. First, results for cortical dipoles are presented. The so-called differential SNR (5.2) is visualized on both the source space and the inflated source space, for each of the three head model forward computations. Furthermore, the modulation of source depth and orientation is investigated and visualized through boxplots and heat maps. With regard to subcortical sources, boxplots showing the behavior of SNR values for EEG/MEG for tangential and radial dipoles, and the different head models are presented.

As a general result, we noticed that EEG SNR values are remarkably sensitive to head modeling. EEG SNR values are higher when a three compartment head model is used and decrease when the number of compartments considered increases. In particular, the main difference is given by the introduction of the CSF layer. When such a conductive material is indeed included in the model, a shunting phenomenon occurs and leads to a decrease of the signal amplitude. This effect is in line with other findings in literature. In [87], for example, a guideline for EEG and MEG forward modeling using lagrangian FEM in realistic head models with a varying number of layers and conductivity profiles is proposed. The inclusion of the CSF compartment had a large impact on the EEG signal magnitude, and the EEG signal magnitude is directly connected to SNR values by definition (see formula (5.1)). In the MEG case, the signal magnitude was not remarkably modified by the CSF inclusion and so are the SNR values reported in our study. This modulation is notable, in our study, both for cortical and subcortical sources. EEG SNR values are overestimated in a three compartment head model therefore a four or six compartment head model delivers a more reliable EEG sensitivity map. It is not the case for the MEG sensitivity map, since the variation between MEG SNR values throughout head models is not evident nor remarkable. On the other side, the effect of source depth and source orientation for cortical sources is extremely large for MEG SNR values and weaker for EEG SNR values. It is indeed visible how MEG SNR values are higher for tangential dipoles and decrease for radially oriented sources. This phenomenon is a clear consequence of the well known blindness of MEG signals to radially oriented dipoles outside of a sphere [78]. Even if in the proposed scenario the geometry is closer to a human head model, the symmetry effects valid outside of a sphere propagate in the realistic scenario. For the same reason, the MEG sensitivity deteriorates when the source depth increases, as the dipoles get more and more radial. In this regard, we observe an almost null modulation of EEG SNR values to both depth and orientation. In [87], the depth effect for cortical dipoles was also estimated and results are in line with the ones presented in this chapter.

Figure 5.12 describes and summarizes clearly the sensitivity of the MEG signal. For the most superficial dipoles (dipoles with a distance of up to 2 mm from the inner skull compartment), MEG SNR values reach the minimum. This behavior is easily justifiable by the fact that the most superficial dipoles corresponds to sources lying on the top of the gyri, where the orientation of the pyramidal cells is radial to the inner skull surface. When considering dipoles with a slightly higher depth (around 3 mm), the MEG SNR values abruptly increase and reach the maximum. The focus has been indeed shifted to dipoles lying on the sulci walls, where the orientation is tangential. Dipoles on the upper part of sulci walls represent the most visible sources for MEG and give the absolute maximum SNR values for both MEG and EEG. From approximately 8 mm distance to the inner skull compartment, we consequently see a linear decay of MEG SNR values for the increasing source depth.

When analyzing subcortical results, first of all, we observe that subcortical SNR values are lower than cortical SNR values, especially in the MEG case. Depth modulation is indeed more evident for subcortical sources for both EEG and MEG SNR values. This result is in line with what already discussed about the modulation of depth in EEG and MEG SNR values, i.e., strong in the MEG case and weaker in the EEG case. In this scenario we again observe rather constant values for the EEG case and largely varying values for the MEG case. Here, the dipole orientation was chosen a-posteriori and based on the assumption that the MEG is less sensitive to radial sources. What is clear from Figure 5.14 is that the difference between radial and tangential component is large, i.e., more than 15 dB. On the other side, it is important to observe that, for tangential subcortical dipoles, the range of MEG SNR values is the same as the one of EEG SNR values. Moreover, in the case of the cerebellum, MEG SNR values are even higher than EEG SNR values.

In other studies, the sensitivity of EEG and/or MEG has been analyzed. In [47], which is an extension of the former work in [43], EEG and MEG sensitivity to epileptic spike activity as function of source orientation and depth is studied. In this work, the SNR is defined as a quantitative measure of the linear amplitude ratio between the background activity and the spike peak, and it is based on the best channel for each source, therefore the values are not directly comparable with the SNR values presented in our work. However, the general results are in line with the ones presented in this chapter, namely, for more superficial sources, EEG SNR values are higher for radial sources and MEG SNR values are higher for tangential sources (as shown, e.g., in [43]). On the other side, for deeper sources, the SNR in the EEG was consistently slightly higher than in the MEG, which is in agreement with [38]. The forward problem was solved in a four layered isotropic head model with BEM and considering only cortical sources. They showed that EEG and MEG have complementary sensitivities to dipolar and patch sources. They conclude that simultaneous EEG and MEG recordings increase the probability to detect epileptic spikes.

In [6], the focus is on subcortical sources. In this review, they present the basic physiology of MEG/EEG data and report the state-of-the-art of deep brain activity reconstruction. There is an explicit MEG sensitivity study for cortical and subcortical sources, while the analogous study for EEG signals is missing. The subcortical source orientations were chosen to be random for thalamus, striatum and amygdala; along the main axis of the surface envelope of nuclei with oriented sources, i.e., reticular perithalamic nucleus, lateral geniculate nucleus and external pallidum; normal to the surface for hippocampus. The forward problem was solved in a sphere model, while the source locations were extracted from a brain template. The average root mean square for all locations in the source space of each structure is chosen as measure of sensitivity, while in our work we used the SNR expressed in formula (5.1), therefore the results are not directly comparable. However, our results are in line with the ones presented in [6]. More specifically, they found that the MEG sensitivity drops off drastically with the distance from sensors between cortical and subcortical dipoles, which is reflected in our Figures 5.13 and 5.14. Furthermore, due to their higher depth within the brain, the thalamus and lateral geniculate nucleus gave the lowest root mean-squared values and this is the case also for our SNR values in Figure 5.14, right column, where thalamus and ventral diencephalon give the lowest values. In our study, unlike [6], we considered dipoles in the whole volume of hippocampus as done in [49], furthermore, we included the study on the cerebellum.

Our results are also in agreement with [45], where the MEG sensitivity was

studied through probability maps of localizing any source on an MRI-extracted cortical surface to within a cubic volume of 1 cm^3. They computed MEG forward solutions in spherical head models and considering cortical dipoles lying on the gray/white matter surface interface. The main message of their work is that gyral sources are not invisible to MEG and that depth is more crucial than orientation to MEG sensitivity, since only 5 % of the cortical dipoles have a predominantly radial orientation. These findings are clearly reproduced in Figure 5.11 and Figure 5.10a, where we see that only thin strips at the troughs of sulci and at the crests of gyri together with deeper sources have lower MEG SNR values, and that overall tangential dipoles represents the majority of the cortical dipoles, respectively.
Finally, in [38] EEG and MEG SNR maps are computed, compared and visualized in inflated cortical surfaces. Although the SNR formula is the one we adopted in our study (see (5.1)), in [38] a BEM computation was performed in a three compartment isotropic head model and only cortical dipoles were considered in the gray/white matter surface interface, with normal orientation. They adopted two different noise estimations, namely, one from realistic EEG and MEG recordings and one from an analytical model. Their final recommendation is to rather estimate noise from actual recordings, which motivated our noise estimation method. Their results confirm complementarity of EEG and MEG techniques, therefore a combined analysis is recommended. EEG is more sensitive to deeper and radial dipoles, while MEG is more sensitive to tangential dipoles. Nevertheless, according to our results, the same EEG SNR overestimation is present in the differential SNR map presented in [38], leading to the conclusion that the strips where MEG is less sensitive than EEG are even thinner than the one presented in [38]. As a final remark, the general trend of the results are not influenced by choosing a noise estimation dependent or independent from the number of trials (see Figure 5.15).

5.4. Conclusions

In this work we computed and analyzed EEG and MEG SNR mappings for three head models, from a simple isotropic three compartment head model, to an isotropic four compartment head model, until a more detailed six compartment head model with anisotropic white matter, and two source spaces, namely a cortical surface and a subcortical volume. The forward model was solved using a state-of-the-art lagrangian finite element method implemented in the *duneuro* software [64]. Aim of this work was dual. First, assess the level of accuracy needed to achieve more reliable sensitivity maps. Second, extract useful insights from accurate EEG and MEG sensitivity maps. Results show that, first, a three compartment head model leads to overestimated EEG SNR values, it is therefore recommended to rely on sensitivity maps which were built on top of a head model where at least the CSF compartment is taken into account. MEG SNR maps resulted to be less sensitive to the head model used. Second, on the cortical level, only MEG SNR values are strongly modulated by source orientation and depth, but the number of deep and radial sources is lower than superficial and tangential sources, therefore overalls MEG SNR values are higher than EEG SNR values when considering cortical sources. With regard to subcortical sources, SNR values are overall lower than cortical SNR values for both EEG and MEG. While EEG SNR values are less sensitive to source orientation also in the context of subcortical sources, MEG SNR values remarkably vary with the orientation. MEG SNR values are indeed more than 10 dB lower when considering radial sources, if compared to MEG SNR values for subcortical tangential dipoles. Therefore, these simulation results show that deep tangential sources can be detected by both the EEG and MEG modalities [69].

Summary and Outlook

Summary After presenting both a physiological and a mathematical background in Chapter 1, where the EEG and MEG forward problems have been derived, CG- and DG-FEM have been presented and extensively tested in Chapter 2 and 3, respectively. Here, we have analyzed the behavior of the MEG solution with regard to different mesh resolutions and representations of the singular source term, such as the subtraction approach, the partial integration and Venant's approach. In Chapter 4, the performances of CG- and DG-FEM for solving the MEG forward problem have been compared both in spherical and realistically shaped head models. We were able to show the convergence of the methods, the overall outperforming performance of both methods when the partial integration approach is adopted in comparison to those when the subtraction approach is chosen as discretization of the source term. Furthermore, in sphere models, DG-FEM provided results that are in a comparable range of high accuracy as to the CG-FEM, whereas in realistically shaped head models, we reported slightly more accurate results when DG-FEM is utilized.

The introduction of DG-FEM was motivated by a previous EEG study [31] where more accurate EEG forward solutions were achieved in presence of skull leakages when DG-FEM was employed. In contrast, the skull leakage effects did not play a crucial role for MEG. However, for EEG or combined MEG/EEG source analysis scenarios, DG-FEM offers an interesting new alternative to CG-FEM, considering the importance of a high accuracy of the forward problem solution in MEG/EEG source reconstruction.

Finally, in Chapter 5, a sensitivity study is presented. In this work we computed and analyzed EEG and MEG SNR mappings for three head models, from a simple isotropic 3 compartment head model, to an isotropic 4 compartment head model, until a more detailed 6 compartment head model with anisotropic white matter, and two source spaces, namely a cortical surface and a subcortical volume. Results show that, first, a three compartment head model leads to overestimated EEG SNR values, it is therefore recommended to rely on sensitivity maps which were built on top of a head model where at least the CSF compartment is taken into account. MEG SNR maps resulted to be less sensitive to the head model used. Second, on the cortical level, only MEG SNR values are strongly modulated by source orientation and depth, but the number of deep and radial sources is lower than superficial and tangential sources, therefore overalls MEG SNR values are higher than EEG SNR values when considering cortical sources. As to subcortical sources, SNR values are overall lower than cortical SNR values for both EEG and MEG. While EEG SNR values are insensitive to source orientation also in the context of subcortical sources, MEG SNR values remarkably vary with the orientation. MEG SNR values are indeed more than 10 dB lower when considering radial sources, if compared to MEG SNR values for subcortical tangential dipoles. Therefore, these simulation results show that deep tangential sources can be detected by both the EEG and MEG modalities.

Outlook We now discuss possibilities for further accuracy increase that it is worth to evaluate in future works. First of all, in every simulation performed in this thesis the sources were just chosen randomly, i.e., the influence of the source position relative to an element of the discretization was not yet investigated. It is well known that, for the subtraction approach, the combination of computing leadfields only for the most accurate sources combined with leadfield inter- and extrapolation techniques for other sources might not only speed up computations, but might also further increase numerical accuracy [98, 85]. In the DG-FEM scheme, indeed, already in the EEG forward computation (see Equation (3.16)), the contribution given by the integral over the internal skeleton can reach high values when the source is relatively close to a quadrature point on the internal skeleton, because of the singularity in ∇u^{∞}. In addition, the degrees of polynomials in V_h^1 can be increased, together with the order of the Raviart-Thomas function space used to extend the conservative flux into the volume of each element. On the other hand, increasing the order of function spaces results in increased computational costs, so this intervention should be treated carefully.

Furthermore, the DG-FEM constitutes the first step for the unfitted discontinuous Galerkin FEM implementation. This method, already tested in an EEG study [65], reduces the geometrical error of the forward simulations in hexahedral models while drastically decreasing the computational cost and thus its application to the MEG forward modeling represents an interesting future goal.

Within the DG-FEM framework, further studies can be conducted with respect to different source term discretization, such as the localized subtraction approach [63], Venant's approach and Whitney approach. More in details, the main idea of the localized subtraction approach is to consider the infinity potential u^{∞} only on a subdomain D^{∞} of Ω which contains the dipole. The idea and first evaluations of the localized subtraction for the EEG forward problem can be found in [63], where it has been shown that the same accuracy as the classical subtraction approach is achieved, with a remarkable reduction of the computational time. As to the MEG forward problem, Biot-Savart's law has to be modified in order to take into account the new shape of $u = u^{corr} + u^{\infty}\chi_{D^{\infty}}$, where $\chi_{D^{\infty}}$ indicates the indicator function in the subdomain B^{∞}. It is to be noted that, despite the boundary-discretization of the classical subtraction approach presented in [30], σ can jump in D^{∞} and that $\Omega^{\infty} \subset D^{\infty}$. Also in this scenario, the numerical integration of the singular ∇u^{∞} has to be carefully treated. The general framework has already been implemented in *duneuro* but more tests and evaluations are necessary.

So far, the discretization of the localized subtraction has been derived in a DG-FEM context, since the indicator function belongs to the test function space. An alternative formalization might be conducted where smooth functions are considered instead of the indicator function and therefore the method can be implemented also in a CG-FEM scenario. Moreover, a boundary representation of Biot-Savart's law can be considered not only on the patch where σ is supposed to be constant (cfr. Section 2.7), but globally over the whole computational domain.

In addition, since we deduced from this thesis that the MEG forward solution is extremely sensitive to the flux representation close to the source position, the assumption made on the source model as a single dipolar source might be too strong. A point dipole does not reflect the physiological behavior of a neural population activity when the observation point approaches the source position. Furthermore, it has already been shown that a dipole model yields depth deviations which are small but systematic if compared to a more realistic and slightly extended source patch with finite amplitude [27]. Therefore, on one side, numerical approaches to discretize the source term which are modeling a more extended source, such as Whitney approach, might lead to remarkable improvements in the accuracy of MEG forward problem solutions. On the other side, reference analytical solutions which include an extended source might be a more realistic description of the physiological behavior of the underneath neural activity.

With regard to the sensitivity study in Chapter 5, some aspects might be further examined. First, the level of noise used in the SNR index used in our study is related to a particular SEP/SEF experiment, while it would be more desirable to have a level of noise which is experiment-independent. Second, this study can be extended in order to create and study sensitivy maps for infants, children or patients with brain lesions, together with different sensor configurations, e.g., intracranial EEG sensors.

Finally, an important aspect that should be considered is the usability of the implemented new methods in *duneuro* [64]. We are planning to let the source code be open-source and educational courses have been already internationally taught at an international conference (`http://www.fieldtriptoolbox.org/workshop/ohbm2018`, where a first attempt of *duneuro*-Fieldtrip integration was performed) and a summer school (`https://www.tu-ilmenau.de/bmti/wissenschaftliche-veranstaltungen/summer-schools/bme-school-2018/`).

A. Appendix

In this Appendix we gathered the description of the input data which are used in Chapter 2, 3 and 4, the definition of the error measures adopted throughout the whole thesis and the transfer matrix approach.

A.1. Volume Conductor Models

For numerical accuracy tests of our CG- and DG-FEM implementations, we generated 4-layer homogeneous sphere models for which an analytical solution for the MEG exists. We used four compartments with different conductivities in order to evaluate if, besides the analytical solution in (1.14), also our numerical implementations show conductivity-independence of MEG in spherical volume conductors and because the four compartment model is closer to a realistic head model as shown in Figure 3.15. The four compartments, whose radii and conductivities are shown in Table A.1 (same parametrization as in [31]), are rough approximations for skin, skull, cerebrospinal fluid (CSF) and brain compartments. The spherical domain is represented via hexahedral meshes with three different resolutions, namely 4 mm, 2 mm and 1 mm.

Tissue	Outer radius	Conductivity	Reference
brain	78 mm	0.33 S/m	[75]
CSF	80 mm	1.79 S/m	[16]
skull	86 mm	0.01 S/m	[25]
skin	92 mm	0.43 S/m	[25],[75]

Table A.1.: Parameters of 4-layer sphere model.

	Segm. Res.	Mesh width (h)	#vertices	#elements
seg_4_res_4	4 mm	4 mm	56,235	51,104
seg_2_res_2	2 mm	2 mm	428,185	407,907
seg_1_res_1	1 mm	1 mm	3,342,701	3,262,312

Table A.2.: Parameters (from left to right) of the regular hexahedral meshes of the 4-layer sphere models used for validation purposes: segmentation resolution (Segm. Res.), mesh width (h), number of vertices and number of elements.

A.2. Sources and Sensors

As only tangential orientation components produce an MEG signal in a multi-layer sphere model, we generated 10,000 dipoles with purely tangential orientations and unit strengths. The sources were uniformly distributed inside the brain compartment on spherical surfaces with 10 different logarithmically scaled eccentricities reported in Table A.3. A source with eccentricity value of 0 is positioned in the center of the sphere, while a source with eccentricity value of 1 belongs to the surface separating brain and CSF compartments. The logarithmic scaling was chosen, since it is well known that numerical errors increase with decreasing distance of a source to the next conductivity jump [96, 30]. We therefore expect larger numerical errors especially for the sources at the highest eccentricity of 0.9873, which only have a distance of 0.99 mm to the CSF compartment. As the cortex has a thickness of 4 to 2 mm [60, 41] and the sources are located in the center of the gray matter, the sources which are most important to analyze are those with a distance of 2 to 1 mm to the CSF compartment. Therefore we focus on the results of sources whose eccentricities are between 0.9642 (2.79 mm from the CSF compartment) and 0.9873 (0.99 mm from the CSF compartment) and especially on those with the middle value of this range, i.e., 0.9796 (1.59 mm from the CSF compartment). Furthermore, *in praxis*, sources are usually placed so that at least one layer of elements is between the source element and the conductivity jump, which is fulfilled for the considered eccentricities $\leqslant 0.9873$ in the 1 mm model (*seg_1_res_1*) and $\leqslant 0.9642$ in the 2 mm model (*seg_2_res_2*). See Table A.3 for details on the eccentricities and the corresponding distance from the CSF compartment. Furthermore, dipoles not belonging to the brain compartment are excluded from the statistics (990 for the 4 mm mesh and 330 for the 2 mm mesh). With regard to the MEG sensors, we used 256 point-magnetometers outside the sphere model at a fixed radius of 110 mm (see Figure A.1).

Eccentricity	Distance to CSF comp. (mm)
0.1	77.22
0.5025	38.80
0.7487	19.60
0.8718	9.99
0.9334	5.19
0.9642	2.79
0.9796	1.59
0.9873	0.99

Table A.3.: Source eccentricities and corresponding distances to the CSF compartment.

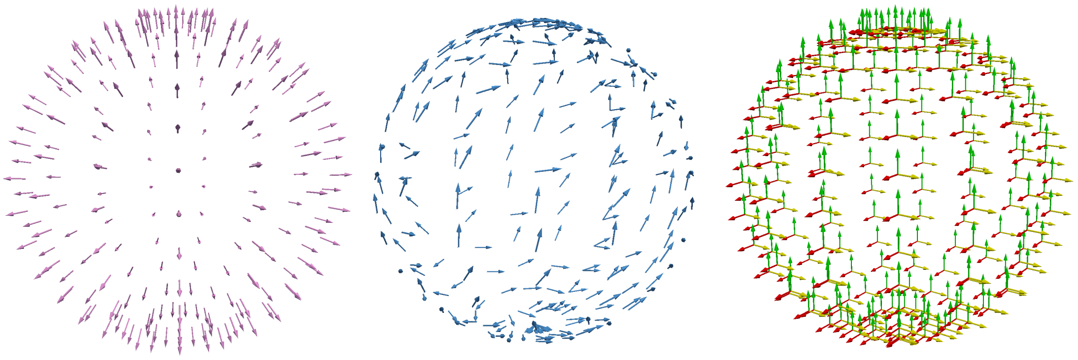

Figure A.1.: Visualization of the 256 point-magnetometers used in the sphere model analysis. Radially (left) and tangentially (middle) oriented point-magnetometers have been employed exclusively in Section 2.7, while in all other studies all the three Cartesian components (right) of the vector fields $\mathbf{B}^p$, $\mathbf{B}^s$ and $\mathbf{B}$ have been considered.

A.3. Error Measures

We used the two error metrics that are commonly used for validating EEG and MEG forward approaches [56, 17, 83, 54, 79, 96], namely, the relative difference measure in percentage (RDM%) for topographical errors:

$$RDM\%(\mathbf{f}_{ana}, \mathbf{f}_{num}) = 50 \left\| \frac{\mathbf{f}_{num}}{\|\mathbf{f}_{num}\|_2} - \frac{\mathbf{f}_{ana}}{\|\mathbf{f}_{ana}\|_2} \right\|_2, \tag{A.1}$$

and the magnitude error in percentage (MAG%):

$$MAG\%(\mathbf{f}_{ana}, \mathbf{f}_{num}) = 100 \left(\frac{\|\mathbf{f}_{num}\|_2}{\|\mathbf{f}_{ana}\|_2} - 1 \right), \tag{A.2}$$

where $\mathbf{f}$ is either the secondary B-field $\mathbf{B}^s$ or the full B-field $\mathbf{B}$. Note that we considered vector-magnetic fields ($\mathbf{B}^p$, $\mathbf{B}^s$, $\mathbf{B}$) without projecting them into radial nor tangential directions, i.e., without distinguishing between radial and tangential point-magnetometers. Statistical results of numerical accuracies are visualized with mean curves, boxplots and cumulative relative frequencies curves. In the boxplots, the analysis includes maximum and minimum, indicated by upper and lower error bars, and thereby the total range (TR). Furthermore, it includes the interval between upper and lower quartile, i.e., the interquartile range (IQR), which is marked by a box with a black dash showing the median. A cumulative relative frequency graph of a quantitative variable is a curve graphically showing the cumulative relative frequency distribution. For example, a point in the cumulative relative frequency curve of the RDM% shows the frequency proportion of dipoles (on y-axis) whose correspondent numerical solution has an RDM% which is less or equal to the level given by the x-axis.

A.4. The Transfer Matrix Approach

In order to speed up the many numerically expensive computations of the secondary B-field $\mathbf{B}^s$ for all of these sources, following [95], we adapted and implemented transfer matrix approaches for all three presented CG- and DG-

FEM-based MEG forward modeling schemes.
If $A\mathbf{u} = \mathbf{l}$ represents the resulting linear system of the EEG forward computation discretization, we can formally write

$$\mathbf{u} = A^{-1}\mathbf{l}. \tag{A.3}$$

If we combine (A.3) and (2.20) or (3.23) in the CG- or DG-FEM case, respectively, we obtain

$$\mathbf{B}_h^s = S\mathbf{u} = S(A^{-1}\mathbf{l}) = (SA^{-1})\mathbf{l} = B_{MEG}\mathbf{l}, \tag{A.4}$$

where S is a generic secondary magnetic field integration matrix. B_{MEG} is the so-called MEG transfer matrix and allows computing $\mathbf{B}_h^s$ with a matrix-vector multiplication, instead of solving the EEG forward problem and applying S. To compute $B_{MEG} = SA^{-1}$, we can multiply its definition by A from the right and then transpose it. Using the symmetry of A, we arrive at the following matrix equation,

$$AB_{MEG}^t = S^t, \tag{A.5}$$

which can be solved for each row of S (column of S^t). In the case of the subtraction approach, we have

$$\mathbf{B}_{corr,h}^s = S\mathbf{u} = S(A^{-1}\mathbf{l}) = (SA^{-1})\mathbf{l} = B_{MEG}\mathbf{l}, \tag{A.6}$$

and the same procedure to compute B_{MEG} and $\mathbf{B}_{corr,h}^s$ can be applied. After $\mathbf{B}_{corr,h}^s$ is computed, analogously to the subtraction approach for the EEG forward problem, $\mathbf{B}_{\infty,h}^s$ is added in order to obtain the complete contribution to the secondary B-field.

A.5. Implementation Aspects on Solving the MEG Forward Problem in duneuro

The CG- and DG-FEM for solving the MEG forward problem are implemented in *duneuro*[1], which is a software toolbox for modeling in neuroscience [63]. More in

---

[1] `www.duneuro.org`

general, *duneuro* in a flexible open-source C++ software library which computes EEG and MEG forward problem solutions, and allows for brain stimulation simulations. *duneuro* is a module of the Distributed and Unified Numerics Environment (DUNE) [2] [14, 13, 12], which is a modular toolbox for solving partial differential equations with grid-based methods. In particular, we used the DUNE-ALUGrid module [5] for the representation of hexahedral meshes and the DUNE-PDELab module [15] for the discretization of the partial differential equations.

duneuro has a Python and Matlab interfaces so that users in neuroscience do not necessarily have to be confronted with C++ programming. Moreover, both interfaces allow for possible integrations with already existing toolbox used in brain research, e.g., Fieldtrip or Brainstorm (via the Matlab interface), or MNE-Python (via the Python interface).

In this thesis all the simulations have been conducted through the Python interface (Python3 and the jupyter notebook), while examples of Matlab scripts integrated in FieldTrip used in a live demo and hands sessions have been gathered in tutorials[3].

With regard to solving the MEG forward problem in a general framework, i.e., independently from CG- or DG-FEM, the idea is to first write the flux in (1.3) in terms of the basis of a suitable vector-valued function space (cfr. Section 3.5) given the numerical electric potential (i.e., the solution of the EEG forward problem) in the computational domain. Second step is to integrate the cross product between the projected flux and the relative distance to the center of the coil (cfr. (2.19) and (3.22), for the CG- and DG-FEM, respectively). The integration step can be optimized by pre-computing the S matrix in (A.4). Furthermore, when the secondary B-field has to be computed for several dipoles, the transfer matrix approach introduced in Section A.4 is preferred. In the following the main parts of a python code for the resolution of the MEG forward problem via the transfer matrix approach (Section A.4) is presented and commented.

The code is divided into 5 main steps. First, the *MEEG driver* is built, which is a python object that creates the volume conductor and through which all functions can be called.

```
config = {
```

---

[2] http://www.dune-project.org

[3] `http://www.fieldtriptoolbox.org/workshop/ohbm2018`

```
    'type' : 'fitted',
    'solver_type' : 'cg',
    'element_type' : 'hexahedron',
    'meg': {
                'intorderadd' : '3',
                'type' : 'physical'
                },
    'volume_conductor' : {
        'grid.filename' : 'path2grid.msh',
        'tensors.filename' : 'path2tensor.dat'
        }
}
driver = dp.MEEGDriver3d(config)
```

In particular, in `solver_type` we can specify the FE method to employ (CG- or DG-FEM available for the MEG forward problem), in `element_type` the type of the element of the mesh is specified, in `intordadd` the integration order for the quadrature rule is controlled, and in `type` the implementation of the flux can be chosen between `'physical'` for the CG case (see (2.18)) and `'numerical'` in the DG case (see (3.19)). Second, the S matrix in (A.4) is assembled as follows

```
driver.setCoilsAndProjections(coilPos, coilOri)
```

where the coil positions and projections are loaded from files and converted into lists of `FieldVector3D`.
Third, the transfer matrix is computed as follows

```
tm = driver.computeMEGTransferMatrix(configTM)
```

where the config dictionary should contain the *reduction* parameter, which is the minimum defect reduction to achieve when solving the linear system:

```
configTM = {
    'solver' : {
        'reduction' : 1e-7
    }
}
```

Fourth, the transfer matrix is applied, giving the secondary B-field in output:

```
meg = driver.applyMEGTransfer(tm, dipoles, configTM)
```

In particular, the function `applyMEGTransfer` has in input `tm`, i.e., the transfer matrix computed above; `dipoles`, that is:

```
dipoles = [dp.Dipole3d(p,m) for p,m in zip(dipPos, dipMom)]
```

where `dipPos` and `dipMom` are python lists of dipole positions and moments, respectively. In the last input of `applyMEGTransfer` the approach to discretize the source term can be specified. So far, for the MEG resolution of the forward problem, the subtraction and the partial integration approaches are available and tested for both CG- and DG-FEM, while Venant's approach is implemented and tested only for CG-FEM, and a first implementation of localized subtraction approach is included for DG-FEM but not yet extensively tested.
Moreover, in the particular case of the boundary subtraction approach (see 2.7), in order to add the contribution given by $\mathbf{B}^s_\infty$, in the configuration dictionary the key `‘‘post_process_meg’` has to be set to `True`.
Finally, the primary component of the B-field can be analytically computed and the full B-field can be assembled. Note that the output of `applyMEGTransfer` has to be multiply by $-\frac{\mu_0}{4\pi}$.

A.6. Software Tools

Many softwares were adopted to realize this thesis:

Dune implementation of the different finite element methods (*duneuro* and *duneuro-py*)
GIMP image editing
FieldTrip - Matlab pre-processing of EEG and MEG data, elaboration of realistic head models
FreeSurfer segmentation of MRI images
FSL co-registration and manipulation of MRI and DTI images

iso2mesh creation of the volumetric meshes
Latex typesetting the thesis
MeshLab manipulation of meshes
numpy numerical elaboration of results
pandas computation of statistics on results
ParaView visualization of meshes and results
seaborn visualization of results
Seg3D manipulation of volumetric masks

Bibliography

[1] Z. A. Acar and S. Makeig. Neuroelectromagnetic forward head modeling toolbox. *Journal of neuroscience methods*, 190(2):258–270, 2010.

[2] Z. Agirre-Arrizubieta, G. Huiskamp, C. Ferrier, A. Van Huffelen, and F. Leijten. Interictal magnetoencephalography and the irritative zone in the electrocorticogram. *Brain*, 132(11):3060–3071, 2009.

[3] S. P. Ahlfors et al. Sensitivity of meg and eeg to source orientation. *Brain topography*, 23(3):227–232, 2010.

[4] G. Alarcón and Z. Agirre-Arrizubieta. Magnetoencephalography in epilepsy: Is it time for emeg? *Clinical Neurophysiology*, 122(7):1282–1283, 2011.

[5] M. Alkämper, A. Dedner, R. Klöfkorn, and M. Nolte. The DUNE-ALUGrid Module. *Archive of Numerical Software*, 4(1):1–28, 2016.

[6] Y. Attal, B. Maess, A. Friederici, and O. David. Head models and dynamic causal modeling of subcortical activity using magnetoencephalographic/-electroencephalographic data. *Reviews in the Neurosciences*, 23(1):85–95, 2012.

[7] K. A. Awada, D. R. Jackson, J. T. Williams, D. R. Wilton, S. B. Baumann, and A. C. Papanicolaou. Computational aspects of finite element modeling in EEG source localization. *IEEE Transactions on Biomedical Engineering*, 44(8):736–752, 1997.

[8] Ü. Aydin, S. Rampp, A. Wollbrink, H. Kugel, J.-H. Cho, T. Knösche, C. Grova, J. Wellmer, and C. Wolters. Zoomed MRI Guided by Combined EEG/MEG Source Analysis: A Multimodal Approach for Optimizing Presurgical Epilepsy Work-up and its Application in a Multi-focal Epilepsy Patient Case Study. *Brain Topography*, pages 1–17, 2017.

[9] Ü. Aydin, J. Vorwerk, M. Dümpelmann, P. Küpper, H. Kugel, M. Heers, J. Wellmer, C. Kellinghaus, J. Haueisen, S. Rampp, et al. Combined EEG/MEG can outperform single modality EEG or MEG source reconstruction in presurgical epilepsy diagnosis. *PloS one*, 10(3):e0118753, 2015.

[10] Ü. Aydin, J. Vorwerk, P. Küpper, M. Heers, H. Kugel, A. Galka, L. Hamid, J. Wellmer, C. Kellinghaus, S. Rampp, et al. Combining eeg and meg for the reconstruction of epileptic activity using a calibrated realistic volume conductor model. *PLoS One*, 9(3):e93154, 2014.

[11] A. Barr de Saint-Venant. Memoire sur la torsion des prismes. *CR Acad. Sci*, 37, 1853.

[12] P. Bastian and M. Blatt. Iterative Solver Template Library. 2007.

[13] P. Bastian, M. Blatt, A. Dedner, C. Engwer, R. Klöfkorn, R. Kornhuber, M. Ohlberger, and O. Sander. A generic grid interface for parallel and adaptive scientific computing. part II: Implementation and tests in DUNE. *Computing*, 82(2-3):121–138, 2008.

[14] P. Bastian, M. Blatt, A. Dedner, C. Engwer, R. Klöfkorn, M. Ohlberger, and O. Sander. A generic grid interface for parallel and adaptive scientific computing. part I: abstract framework. *Computing*, 82(2):103–119, 2008.

[15] P. Bastian, F. Heimann, and S. Marnach. Generic implementation of finite element methods in the distributed and unified numerics environment (DUNE). *Kybernetika*, 46(2):294–315, 2010.

[16] S. B. Baumann, D. R. Wozny, S. K. Kelly, and F. M. Meno. The electrical

conductivity of human cerebrospinal fluid at body temperature. *IEEE Transactions on Biomedical Engineering*, 44(3):220–223, 1997.

[17] O. Bertrand, M. Thevenet, and F. Perrin. 3D finite element method in brain electrical activity studies. *Biomagnetic Localization and 3D Modelling*, pages 154–171, 1991.

[18] R. Brette and A. Destexhe. *Handbook of neural activity measurement*. Cambridge University Press, 2012.

[19] H. Buchner, M. Fuchs, H.-A. Wischmann, O. Dössel, I. Ludwig, A. Knepper, and P. Berg. Source analysis of median nerve and finger stimulated somatosensory evoked potentials: multichannel simultaneous recording of electric and magnetic fields combined with 3d-mr tomography. *Brain topography*, 6(4):299–310, 1994.

[20] H. Buchner, G. Knoll, M. Fuchs, A. Rienäcker, R. Beckmann, M. Wagner, J. Silny, and J. Pesch. Inverse localization of electric dipole current sources in finite element models of the human head. *Electroencephalography and clinical Neurophysiology*, 102(4):267–278, 1997.

[21] P. G. Ciarlet. The finite element method for elliptic problems. *Classics in applied mathematics*, 40:1–511, 2002.

[22] CIBC, 2016. Seg3D: Volumetric Image Segmentation and Visualization. Scientific Computing and Imaging Institute (SCI), Download from: http://www.seg3d.org.

[23] D. Cohen. Magnetoencephalography: detection of the brain's electrical activity with a superconducting magnetometer. *Science*, 175(4022):664–666, 1972.

[24] M. J. Cook and Z. J. Koles. A high-resolution anisotropic finite-volume head model for EEG source analysis. In *Engineering in Medicine and Biology*

Society, 2006. EMBS'06. 28th Annual International Conference of the IEEE, pages 4536–4539. IEEE, 2006.

[25] M. Dannhauer, B. Lanfer, C. H. Wolters, and T. R. Knösche. Modeling of the human skull in EEG source analysis. *Human brain mapping*, 32(9):1383–1399, 2011.

[26] A. Datta, X. Zhou, Y. Su, L. C. Parra, and M. Bikson. Validation of finite element model of transcranial electrical stimulation using scalp potentials: implications for clinical dose. *Journal of neural engineering*, 10(3):036018, 2013.

[27] J. De Munck. The potential distribution in a layered anisotropic spheroidal volume conductor. *Journal of applied Physics*, 64(2):464–470, 1988.

[28] J. C. De Munck, B. W. Van Dijk, and H. Spekreijse. Mathematical dipoles are adequate to describe realistic generators of human brain activity. *IEEE Transactions on Biomedical Engineering*, 35(11):960–966, 1988.

[29] D. A. Di Pietro, A. Ern, and J.-L. Guermond. Discontinuous galerkin methods for anisotropic semidefinite diffusion with advection. *SIAM Journal on Numerical Analysis*, 46(2):805–831, 2008.

[30] F. Drechsler, C. H. Wolters, T. Dierkes, H. Si, and L. Grasedyck. A full subtraction approach for finite element method based source analysis using constrained Delaunay tetrahedralisation. *NeuroImage*, 46(4):1055–1065, 2009.

[31] C. Engwer, J. Vorwerk, J. Ludewig, and C. H. Wolters. A Discontinuous Galerkin Method to Solve the EEG Forward Problem Using the Subtraction Approach. *SIAM Journal on Scientific Computing*, 39(1):B138–B164, 2017.

[32] Q. Fang and D. A. Boas. Tetrahedral mesh generation from volumetric binary and grayscale images. In *Biomedical Imaging: From Nano to Macro,*

2009. ISBI'09. IEEE International Symposium on, pages 1142–1145. Ieee, 2009.

[33] M. Fortin and F. Brezzi. *Mixed and hybrid finite element methods.* New York: Springer-Verlag, 1991.

[34] M. Fuchs, M. Wagner, H.-A. Wischmann, T. Köhler, A. Theißen, R. Drenckhahn, and H. Buchner. Improving source reconstructions by combining bioelectric and biomagnetic data. *Electroencephalography and clinical neurophysiology*, 107(2):93–111, 1998.

[35] N. G. Gençer and C. E. Acar. Sensitivity of eeg and meg measurements to tissue conductivity. *Physics in Medicine & Biology*, 49(5):701, 2004.

[36] D. Geselowitz. On the magnetic field generated outside an inhomogeneous volume conductor by internal current sources. *IEEE Transactions on Magnetics*, 6(2):346–347, 1970.

[37] S. Giani and P. Houston. Anisotropic hp-adaptive discontinuous galerkin finite element methods for compressible fluid flows. *International Journal of Numerical Analysis and Modeling*, 2011.

[38] D. M. Goldenholz et al. Mapping the signal-to-noise-ratios of cortical sources in magnetoencephalography and electroencephalography. *Human brain mapping*, 30(4):1077–1086, 2009.

[39] C. Golgi. Sulla struttura della sostanza grigia del cervello. *Gazz. Med. Ital. Lomb.*, 33:244–246, 1873.

[40] A. Gramfort, T. Papadopoulo, E. Olivi, and M. Clerc. Forward field computation with openmeeg. *Computational intelligence and neuroscience*, 2011, 2011.

[41] M. Hämäläinen, R. Hari, R. J. Ilmoniemi, J. Knuutila, and O. V. Lounasmaa. Magnetoencephalography—theory, instrumentation, and applications to

noninvasive studies of the working human brain. *Reviews of modern Physics*, 65(2):413, 1993.

[42] R. Hari and A. Puce. *MEG-EEG Primer.* Oxford University Press, 2017.

[43] J. Haueisen, M. Funke, D. Güllmar, and R. Eichardt. Tangential and radial epileptic spike activity: different sensitivity in eeg and meg. *Journal of Clinical Neurophysiology*, 29(4):327–332, 2012.

[44] J. Haueisen, C. Ramon, P. Czapski, and M. Eiselt. On the influence of volume currents and extended sources on neuromagnetic fields: a simulation study. *Annals of biomedical engineering*, 23(6):728–739, 1995.

[45] A. Hillebrand and G. Barnes. A quantitative assessment of the sensitivity of whole-head meg to activity in the adult human cortex. *Neuroimage*, 16(3):638–650, 2002.

[46] M.-X. Huang, T. Song, D. J. Hagler Jr, I. Podgorny, V. Jousmaki, L. Cui, K. Gaa, D. L. Harrington, A. M. Dale, R. R. Lee, et al. A novel integrated meg and eeg analysis method for dipolar sources. *Neuroimage*, 37(3):731–748, 2007.

[47] A. Hunold, M. Funke, R. Eichardt, M. Stenroos, and J. Haueisen. Eeg and meg: sensitivity to epileptic spike activity as function of source orientation and depth. *Physiological measurement*, 37(7):1146, 2016.

[48] R. Ilmoniemi. Radial anisotropy added to a spherically symmetric conductor does not affect the external magnetic field due to internal sources. *EPL (Europhysics Letters)*, 30(5):313, 1995.

[49] P. Krishnaswamy, G. Obregon-Henao, J. Ahveninen, S. Khan, B. Babadi, J. E. Iglesias, M. S. Hämäläinen, and P. L. Purdon. Sparsity enables estimation of both subcortical and cortical activity from meg and eeg. *Proceedings of the National Academy of Sciences*, page 201705414, 2017.

[50] B. Lanfer, I. Paul-Jordanov, M. Scherg, and C. H. Wolters. Influence of interior cerebrospinal fluid compartments on eeg source analysis. *Biomedical Engineering/Biomedizinische Technik*, 57(SI-1 Track-F):236–236, 2012.

[51] S. Lau, L. Flemming, and J. Haueisen. Magnetoencephalography signals are influenced by skull defects. *Clinical Neurophysiology*, 125(8):1653–1662, 2014.

[52] S. Lau, D. Güllmar, L. Flemming, D. B. Grayden, M. J. Cook, C. H. Wolters, and J. Haueisen. Skull defects in finite element head models for source reconstruction from magnetoencephalography signals. *Frontiers in neuroscience*, 10, 2016.

[53] S. Lew, C. Wolters, T. Dierkes, C. Röer, and R. MacLeod. Accuracy and run-time comparison for different potential approaches and iterative solvers in finite element method based eeg source analysis. *Applied numerical mathematics: transactions of IMACS*, 59(8):1970, 2009.

[54] G. Marin, C. Guerin, S. Baillet, L. Garnero, and G. Meunier. Influence of skull anisotropy for the forward and inverse problem in EEG: simulation studies using FEM on realistic head models. *Human brain mapping*, 6(4):250–269, 1998.

[55] T. Medani, D. Lautru, D. Schwartz, Z. Ren, and G. Sou. Fem method for the eeg forward problem and improvement based on modification of the saint venant's method. *Progress In Electromagnetics Research*, 153:11–22, 2015.

[56] J. W. Meijs, O. W. Weier, M. J. Peters, and A. Van Oosterom. On the numerical accuracy of the boundary element method (EEG application). *IEEE transactions on biomedical engineering*, 36(10):1038–1049, 1989.

[57] P. C. Miranda, M. Lomarev, and M. Hallett. Modeling the current distribution during transcranial direct current stimulation. *Clinical neurophysiology*, 117(7):1623–1629, 2006.

[58] V. Montes-Restrepo, P. van Mierlo, G. Strobbe, S. Staelens, S. Vandenberghe, and H. Hallez. Influence of skull modeling approaches on EEG source localization. *Brain topography*, 27(1):95–111, 2014.

[59] J. C. Mosher, R. M. Leahy, and P. S. Lewis. EEG and MEG: forward solutions for inverse methods. *IEEE Transactions on Biomedical Engineering*, 46(3):245–259, 1999.

[60] S. Murakami and Y. Okada. Contributions of principal neocortical neurons to magnetoencephalography and electroencephalography signals. *The Journal of physiology*, 575(3):925–936, 2006.

[61] J.-C. Nédélec. Mixed finite elements in r^3. *Numerische Mathematik*, 35(3):315–341, 1980.

[62] J. Nitsche. Über ein variationsprinzip zur lösung von dirichlet-problemen bei verwendung von teilräumen, die keinen randbedingungen unterworfen sind. In *Abhandlungen aus dem mathematischen Seminar der Universität Hamburg*, volume 36, pages 9–15. Springer, 1971.

[63] A. Nüßing. *Fitted and Unfitted Finite Element Methods for Solving the EEG Forward Problem.* PhD thesis, PhD thesis in Mathematics, Westfälische Wilhelms-Universität Münster, 2018.

[64] A. Nüßing, M. C. Piastra, S. Schrader, T. Miinalainen, H. Brinck, C. H. Wolters, and C. Engwer. duneuro - a software toolbox for forward modeling in neuroscience. *http://arxiv.org/abs/1901.02874*.

[65] A. Nüßing, C. H. Wolters, H. Brinck, and C. Engwer. The unfitted discontinuous Galerkin method for solving the EEG forward problem. *IEEE Transactions on Biomedical Engineering*, 63(12):2564–2575, 2016.

[66] Y. Okada. Empirical bases for constraints in current-imaging algorithms. *Brain topography*, 5(4):373–377, 1993.

[67] H. Okamoto, H. Stracke, C. H. Wolters, F. Schmael, and C. Pantev. Attention improves population-level frequency tuning in human auditory cortex. *Journal of Neuroscience*, 27(39):10383–10390, 2007.

[68] R. Oostenveld, P. Fries, E. Maris, and J.-M. Schoffelen. Fieldtrip: open source software for advanced analysis of meg, eeg, and invasive electrophysiological data. *Computational intelligence and neuroscience*, 2011:1, 2011.

[69] L. Parkkonen et al. Sources of auditory brainstem responses revisited: contribution by magnetoencephalography. *Human brain mapping*, 30(6):1772–1782, 2009.

[70] W. D. Penny, K. J. Friston, J. T. Ashburner, S. J. Kiebel, and T. E. Nichols. *Statistical parametric mapping: the analysis of functional brain images.* Elsevier, 2011.

[71] M. C. Piastra, A. Nüßing, J. Vorwerk, H. Bornfleth, R. Oostenveld, C. Engwer, and C. H. Wolters. The discontinuous galerkin finite element method for solving the meg and the combined meg/eeg forward problem. *Frontiers in Neuroscience*, 12:30, 2018.

[72] S. Pursiainen, J. Vorwerk, and C. H. Wolters. Electroencephalography (EEG) forward modeling via H (div) finite element sources with focal interpolation. *Physics in medicine and biology*, 61(24):8502, 2016.

[73] D. Purves, G. J. Augustine, D. Fitzpatrick, W. C. Hall, A.-S. LaMantia, R. D. Mooney, M. L. Platt, and L. E. White, editors. *Neuroscience.* Springer, 6th edition, 2018.

[74] A. Quarteroni and S. Quarteroni. *Numerical models for differential problems*, volume 2. Springer, 2009.

[75] C. Ramon, P. Schimpf, J. Haueisen, M. Holmes, and A. Ishimaru. Role

of soft bone, CSF and gray matter in EEG simulations. *Brain topography*, 16(4):245–248, 2004.

[76] J. K. Rice, C. Rorden, J. S. Little, and L. C. Parra. Subject position affects eeg magnitudes. *NeuroImage*, 64:476–484, 2013.

[77] L. Ruthotto, H. Kugel, J. Olesch, B. Fischer, J. Modersitzki, M. Burger, and C. Wolters. Diffeomorphic susceptibility artifact correction of diffusion-weighted magnetic resonance images. *Physics in Medicine & Biology*, 57(18):5715, 2012.

[78] J. Sarvas. Basic mathematical and electromagnetic concepts of the biomagnetic inverse problem. *Physics in medicine and biology*, 32(1):11, 1987.

[79] P. H. Schimpf, C. Ramon, and J. Haueisen. Dipole models for the EEG and MEG. *Biomedical Engineering, IEEE Transactions on*, 49(5):409–418, 2002.

[80] M. Stenroos and J. Sarvas. Bioelectromagnetic forward problem: isolated source approach revis (it) ed. *Physics in medicine and biology*, 57(11):3517, 2012.

[81] R. T. Thibault, M. Lifshitz, and A. Raz. Body position alters human resting-state: Insights from multi-postural magnetoencephalography. *Brain imaging and behavior*, 10(3):772–780, 2016.

[82] S. Van den Broek, H. Zhou, and M. Peters. Computation of neuromagnetic fields using finite-element method and Biot-Savart law. *Medical and Biological Engineering and Computing*, 34(1):21–26, 1996.

[83] S. P. van den Broek, F. Reinders, M. Donderwinkel, and M. Peters. Volume conduction effects in EEG and MEG. *Electroencephalography and clinical neurophysiology*, 106(6):522–534, 1998.

[84] F. Vatta, F. Meneghini, F. Esposito, S. Mininel, and F. Di Salle. Solving the

forward problem in EEG source analysis by spherical and fdm head modeling: a comparative analysis-biomed 2009. *Biomedical sciences instrumentation*, 45:382–388, 2009.

[85] J. Vorwerk. Comparison of Numerical Approaches to the EEG Forward Problem. Diploma thesis in Mathematics, Westfälische Wilhelms-Universität Münster, 2011.

[86] J. Vorwerk. *New finite element methods to solve the EEG/MEG forward problem*. PhD thesis, PhD thesis in Mathematics, Westfälische Wilhelms-Universität Münster, 2016.

[87] J. Vorwerk, J.-H. Cho, S. Rampp, H. Hamer, T. R. Knösche, and C. H. Wolters. A guideline for head volume conductor modeling in EEG and MEG. *NeuroImage*, 100:590–607, 2014.

[88] J. Vorwerk, C. Engwer, S. Pursiainen, and C. H. Wolters. A mixed finite element method to solve the eeg forward problem. *IEEE transactions on medical imaging*, 36(4):930–941, 2017.

[89] S. Wagner, F. Lucka, J. Vorwerk, C. S. Herrmann, G. Nolte, M. Burger, and C. H. Wolters. Using reciprocity for relating the simulation of transcranial current stimulation to the EEG forward problem. *Neuroimage*, 140:163–173, 2016.

[90] S. Wagner, S. Rampersad, Ü. Aydin, J. Vorwerk, T. Oostendorp, T. Neuling, C. Herrmann, D. Stegeman, and C. Wolters. Investigation of tDCS volume conduction effects in a highly realistic head model. *Journal of neural engineering*, 11(1):016002, 2014.

[91] D. Weinstein, L. Zhukov, and C. Johnson. Lead-field bases for electroencephalography source imaging. *Annals of biomedical engineering*, 28(9):1059–1065, 2000.

[92] K. Wendel, N. G. Narra, M. Hannula, P. Kauppinen, and J. Malmivuo.

The influence of CSF on EEG sensitivity distributions of multilayered head models. *IEEE Transactions on Biomedical Engineering*, 55(4):1454–1456, 2008.

[93] R. Wennberg, T. Valiante, and D. Cheyne. Eeg and meg in mesial temporal lobe epilepsy: where do the spikes really come from? *Clinical neurophysiology*, 122(7):1295–1313, 2011.

[94] M. Windhoff, A. Opitz, and A. Thielscher. Electric field calculations in brain stimulation based on finite elements: an optimized processing pipeline for the generation and usage of accurate individual head models. *Human brain mapping*, 34(4):923–935, 2013.

[95] C. H. Wolters et al. Efficient computation of lead field bases and influence matrix for the fem-based eeg and meg inverse problem. *Inverse problems*, 20(4):1099, 2004.

[96] C. H. Wolters, H. Köstler, C. Möller, J. Härdtlein, L. Grasedyck, and W. Hackbusch. Numerical mathematics of the subtraction method for the modeling of a current dipole in eeg source reconstruction using finite element head models. *SIAM Journal on Scientific Computing*, 30(1):24–45, 2007.

[97] Y. Yan, P. Nunez, and R. Hart. Finite-element model of the human head: scalp potentials due to dipole sources. *Medical and Biological Engineering and Computing*, 29(5):475–481, 1991.

[98] B. Yvert, A. Crouzeix-Cheylus, and J. Pernier. Fast realistic modeling in bioelectromagnetism using lead-field interpolation. *Human brain mapping*, 14(1):48–63, 2001.

[99] J. Zimmerman, P. Thiene, and J. Harding. Design and operation of stable rf-biased superconducting point-contact quantum devices, and a note on the properties of perfectly clean metal contacts. *Journal of Applied Physics*, 41(4):1572–1580, 1970.